Molecular Dynamics Simulation Studies on the Structure, Dynamics, and Interfacial Properties of Room Temperature Ionic Liquids

A Thesis
Submitted For the Degree of
DOCTOR OF PHILOSOPHY
in the Faculty of Science

by

Soumya Saswati Sarangi

CHEMISTRY AND PHYSICS OF MATERIALS UNIT
JAWAHARLAL NEHRU CENTRE FOR ADVANCED SCIENTIFIC RESEARCH
Bangalore – 560 064, India

APRIL 2011

To My Parents

DECLARATION

I hereby declare that the matter embodied in the thesis entitled " **Molecular Dynamics Simulation Studies on the Structure, Dynamics, and Interfacial Properties of Room Temperature Ionic Liquids**" is the result of investigations carried out by me at the Chemistry and Physics of Materials Unit, Jawaharlal Nehru Centre for Advanced Scientific Research, Bangalore, India under the supervision of Prof. S. Balasubramanian and that it has not been submitted elsewhere for the award of any degree or diploma.

In keeping with the general practice in reporting scientific observations, due acknowledgement has been made whenever the work described is based on the findings of other investigators. Any omission that might have occurred by oversight or error of judgement is regretted.

Soumya Saswati Sarangi

CERTIFICATE

I hereby certify that the matter embodied in this thesis entitled “ **Molecular Dynamics Simulation Studies on the Structure, Dynamics, and Interfacial Properties of Room Temperature Ionic Liquids**” has been carried out by Ms. Soumya Saswati Sarangi at the Chemistry and Physics of Materials Unit, Jawaharlal Nehru Centre for Advanced Scientific Research, Bangalore, India under my supervision and that it has not been submitted elsewhere for the award of any degree or diploma.

Prof. S. Balasubramanian
(Research Supervisor)

Acknowledgements

It is my pleasure to thank my research supervisor, Prof. S. Balasubramanian for giving me the opportunity to explore the properties of room temperature ionic liquids using computational methods. I highly acknowledge his unmatched patience, sincerity, guidance, and of professionalism. I am extremely thankful to him for teaching me molecular dynamics simulations. I sincerely appreciate the suggestions and advice he provided on many occasion during my work. I also liked the academic freedom that I received in his group. I am greatly thankful to him for the excellent computing resources he has provided for the group. The research training that I received from him will definitely help me in the coming years.

I thank my collaborators, Prof. Dr. Florian Müller-Plathe and Dr. Wei Zhao from Technical University, Darmstadt, Germany. I express my sincere thanks to Dr. Meheboob Alam, Prof. Umesh Waghmare, Prof. Chandrabhas Narayana, Prof. Swapan Pati, Dr. Prabal Maiti for the various courses they offered. I also thank Dr. Vidhyadhiraja for the fruitful discussions I had with him.

I would like to thank all my past and present lab mates; Dr. M. Krishnan, Dr. M. Saharay, Dr. Bhargava, Srinivas G. Raju, Sandeep Reddy, Bharat, Rajdeep, Sheeba, Kanchan, Dr. Ganga, for their joyous company and help at many stages of my tenure.

I thank the Jawaharlal Nehru Centre for providing excellent research facilities,

stimulating research ambience, and for financial support. I acknowledge JNCASR, CCMS for the computational facilities. I thank DST for a research fellowship. I thank all the staff members of JNCASR for their constant help.

I thank all my friends for all the moments I shared with them. I am grateful to all my teachers through out my carreer.

Finally, I am thankful to my family, who have been a source of constant support and strength for years. I thank my parents, brother, grand mother, and my husband for their patience and encouragement.

I thank all those who have helped me directly or indirectly.

Preface

The thesis entitled "Molecular Dynamics Simulation Studies on the Structure, Dynamics, and Interfacial Properties of Room Temperature Ionic Liquids" presents the results of investigations on room temperature ionic liquids. Classical molecular dynamics simulations were employed to characterize their microscopic structure, dynamics and interfacial properties.

Chapter 1 presents a general introduction to room temperature ionic liquids (RTILs). The methods of synthesis, some important physico-chemical properties, and few applications of the RTILs are discussed. Results of various experimental and theoretical studies on these liquids are reviewed. The chapter also contains a brief introduction to the classical molecular dynamics (MD) method employed in this thesis.

Chapter 2 presents a study on the complex dynamics exhibited by the IL, 1-*n*-butyl,3-methylimidazolium hexafluorophosphate ([bmim][PF_6]) in the temperature range, 250K-450K. The activation energy for the self diffusion of the anion was found to be marginally higher than that for the cation. The calculated electrical conductivity was found to agree well with experimental data. Structural relaxation has been studied through the decay of coherent and incoherent intermediate scattering functions over a range of temperatures and wave vectors relevant to the system. The relaxation data has been used to identify and characterize two processes – β and α. The dynamical heterogeneity of the ions determined through the non-Gaussian parameter indicated the motion of cation to be more heterogeneous than that of the anion. The faster ones among the cations were found to be coordinated to faster anions, while slower cations were surrounded predominantly by slower anions. Thus the dynamical heterogeneity in this ionic liquid was shown to have structural signatures.

In Chapter 3, the far-infrared region of the vibrational spectrum of four RTILs has been examined using two computational methods: normal mode analysis (NMA) and the power spectra obtained from velocity auto correlation functions. A distinct band has been observed around 30 to 70 cm^{-1} in all the liquids. The peak position shifted to higher frequencies with an increase in the strength of the cation-anion interaction. These bands were shown to arise primarily from inter-ionic interactions, but cannot be solely ascribed to localized motions of the hydrogen bond between the cation and the anion. They could be nearly reproduced by local interactions. These findings were confirmed from density functional theory (DFT) based gas phase calculations on ion pairs as well as through periodic calculations of crystalline [bmim][PF_6].

Chapter 4 discusses the influence of the symmetry of the imidazolium cation on the structure and properties of the ionic liquid-vapour interface. The anion chosen was bis(trifluoromethylsulfonyl)imide (NTf_2). At the interface, both cations and anions were present, and the alkyl chains of the former preferred to orient out into the vapour phase. A large fraction of cations were oriented with their ring normal parallel to the surface and alkyl chains perpendicular to it. These orientational preferences were reduced in ionic liquids with symmetric cations. The electrostatic potential difference between the liquid and the vapour phases was positive and decreased with increasing length of the alkyl group. The calculated surface tension of the liquids too decreased with increasing alkyl chain length and its value for a liquid with a symmetric cation was marginally higher than that for one with an asymmetric, isomeric cation.

Chapter 5 presents studies on free standing nanoscopic clusters of [bmim][PF_6] with diameters in the range of 2-8 nm. The butyl tail groups of the [bmim]$^+$ ion protrude outwards from the surface of the cluster while the ring centres lie beneath. The number densities of cation ring centres showed a non-uniform distribution near the surface in comparison to that of anions. An electrostatic potential drop of -0.17 V has been calculated across the cluster-vapour interface for the largest cluster studied. The effective interaction potential between the clusters was found to exhibit a short-ranged, strong attractive well. A linear dependence of this well depth on the cluster size was observed, consistent with the predictions of the interpenetration model for inter-micellar interactions.

Contents

4 Molecular Dynamics Simulations of Ionic Liquid-Vapour Interfaces:

List of Figures

List of Tables

Chapter 1

Introduction

The adoption of environmentally benign processes and procedures in chemistry is gaining increasing importance recently. Such an approach comes under the general term “Green Chemistry”. Apart from aiming for the use of fewer reactants to generate desired products, recyclability of unreacted components, increase of product yield, avoiding processes which consume large energies, green chemistry also advocates the use of environmentally acceptable solvents as chemical reaction media. Solvents in this category are called “Green Solvents”. They are expected to be non-toxic, non-flammable, to possess low vapour pressure and recyclable, and thus could be an attractive alternative to volatile organic compounds (VOCs) [1]. VOCs are being abundantly used in chemical processes for mass and heat transfer. They are also being used in separations and purification processes. They are an integral and primary component in cleaning agents, adhesives, and coatings. Therefore, the widespread use of such organic solvents contribute significantly to the generated waste in the chemical processes.

Research in this area has grown enormously over the last 10 years [2,3]. Green solvents must first of all be able to dissolve the solutes and in addition, be non-volatile, less toxic, easily recyclable, inert, nonflammable, biodegradable, and should not contaminate the product. These properties are termed as the environmental, health, and safety (EHS) properties to categorize the solvents as "environmentally poor" or "environmentally benign" solvents [4, 5]. They should also possess a high degree of solubility for both polar and non-polar solutes. Examples of such solvents include: water, supercritical fluids, room-temperature ionic liquids (RTILs), etc. [5].

Ionic liquids (ILs) can be categorized into three classes. They are: inorganic, protic, and aprotic ILs [6,7]. Inorganic ILs are salts composed of inorganic ions and have a high melting point. Protic and aprotic ILs are made up of mostly organic cations and organic/inorganic anions. ILs where a proton is transferred from an inorganic acid to a Bronsted base are called "protic".

This thesis is focussed on aprotic RTILs.

1.1 Room Temperature Ionic Liquids

Although there exists no concrete definition for RTILs, they could in general be defined as liquids composed entirely of ions at room temperature. Conventionally, following Paul Walden [8], the term room temperature ionic liquids is allowed to be used for salts which melt below 100^{o}C. Unlike inorganic molten salts which melt at much higher temperatures, RTILs possess low melting points [4, 9, 10]. The constituent ions in the former are mostly non-molecular; hence the electrostatic interaction between unlike ions is rather strong which increases the stability of the corresponding crystalline phases and thus the melting point. Common examples of inorganic ionic crystals are NaCl, ZnCl, $MgCl_2$, $AlCl_3$ etc. The strong electrostatic interactions among the ions increase the Madelung energy in the case of ionic crystals, which is the cause of their high melting temperatures. For example, the melting point of NaCl is 801 ^{o}C [11]. On the other hand, RTILs are generally composed of large, organic, and mostly asymmetric cations having poor coordination with organic/inorganic, reasonably large anions. The bulky and asymmetric nature of the ions hinder the packing among the ions leading to weak covalent bonds between them. There also exists a possibility of weak hydrogen bonding interactions between the cations and anions, which further fluidizes the ionic liquids. An exposition of the similarities and differences between inorganic molten salts and RTILs was provided by Kirchner and coworkers recently [12, 13].

In addition to the molecular structure of the constituent ions, the type and strength of the interactions between them play a crucial role in deciding many of the physico-chemical properties of RTILs [4, 14–17]. Apart from the electrostatic interaction between the ions, dispersion between the alkyl groups and directional ion-ion hydrogen bonding exist in RTILs. Depending on the applications they are meant to be used for, RTILs can be synthesized by a suitable choice of cation and anion. Some of the commonly used cations are imidazolium, pyrazolium, triazolium, thiazolium, oxazolium, pyridinium, pyridazinium, pyrimidinium, pyrazinium, pyrrolidinium etc. Anions can be broadly divided into two groups, fluorous and non-fluorous. The common inorganic fluorous anions are tetrafluroborate and hexafluorophosphate, and the organic, non-fluorous anions include sulfonate, imide and methide. Figure 1.1 shows the structure of some cations and Figure 1.2 shows structures of some of the anions.

The properties of ionic liquids change readily by changing the type of an ion. For example, 1-*n*-butyl-3-methylimidazolium ([bmim]) tetrafluoroborate ([BF_4]) is fully miscible with water [4], whereas its hexafluorophosphate ([PF_6]) analogue dissolves up to only 2 wt % in water [18]. The dependence of physico-chemical properties of ILs on the nature of cations and anions is given in detail later.

Thus, in principle, millions of binary RTILs and many more ternary RTILs can possibly be made in comparison to around 1,000 available molecular solvents till date [15]. Hence, RTILs are sometimes referred to as “designer solvents” or “ tailor-made solvents”.

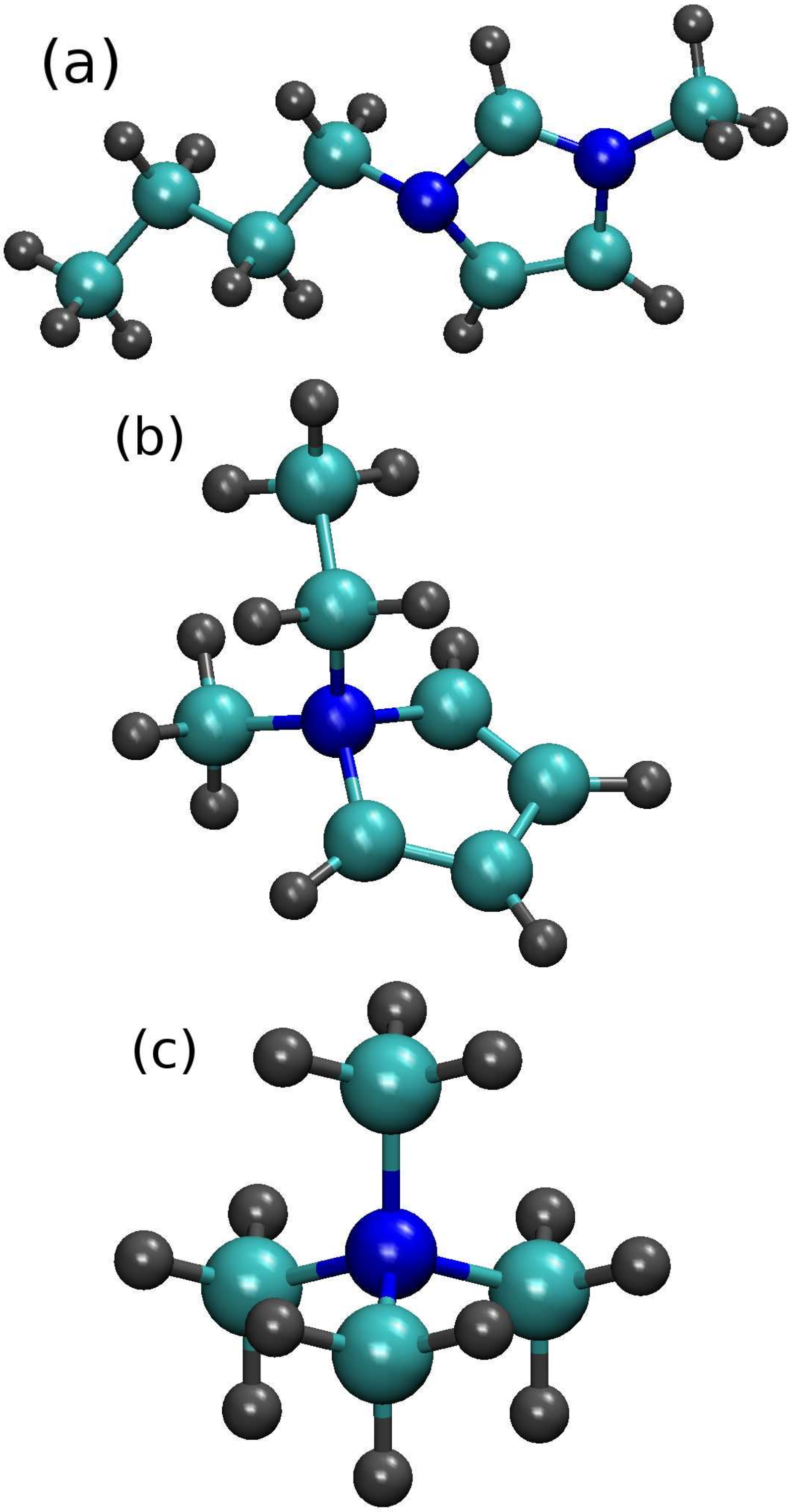

Figure 1.1: (a)1-butyl-3-methylimidazolium (b)N-ethyl-methylpyrrolidinium (c) Tetramethylammonium. Colours : Nitrogen–blue, Carbon–cyan, Hydrogen–gray

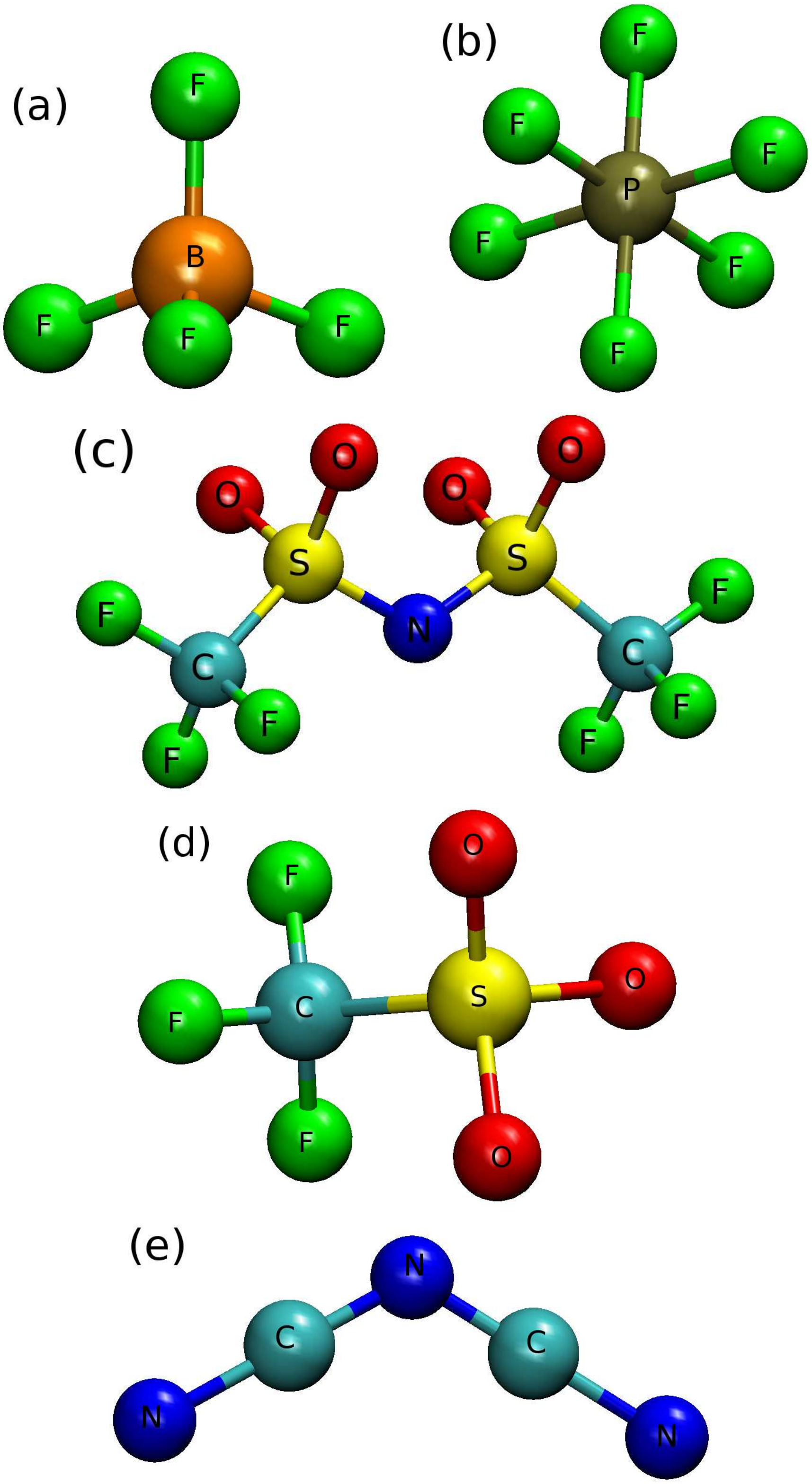

Figure 1.2: (a)Tetrafluoroborate$[BF_4]^-$ (b)Hexaflourophosphate$[PF_6]^-$ (c)Bis(trifluoromethanesulfonyl)imide$[NTf_2]^-$ (d)Trifluoromethanesulfonate$[CF_3SO_3]^-$ (e) Dicyanamide $[N(CN)_2]^-$.

ILs have an abundance of charge carrying entities, which allows them to be used as solvents without the need for a supporting electrolyte [9, 16, 19]. Further, their wide electrochemical window enables them to be used as electrolytes. They are non-flammable, non-corrosive, thermally and hydrolytically stable. In general, they possess a wide liquid range. They have a negligible vapour pressure, hence can be considered as non-volatile. Many RTILs are much more viscous than traditional solvents. The viscosity of [bmim][PF_6] is around 250 cP [20–22]. RTILs are also proven to be good solvents or catalysts for many organic reactions [14, 23, 24].

1.1.1 Synthesis

The first RTIL, ethylammonium nitrate ([$EtNH_3$][NO_3]) was synthesized in 1914 [8]. It has a melting point around 12 ^{o}C. [$EtNH_3$][NO_3] was synthesized from concentrated nitric acid (HNO_3) and ethylamine. The synthesis of ionic liquids consists of two chief steps: first is to prepare the desired cation and the second step is to perform the anion exchange reaction to get the desired IL. Welton published a quality review on the use of RTILs for synthesis and catalysis [14].

Cations are synthesized by either the process of "protonation" with an acid or by the "quaternization" of an amine, phosphine, or sulfide, using a haloalkane or dialkylsulfates (alkylating agent). Along with the first synthesized IL ([$EtNH_3$][NO_3]), many ILs having 1-alkylimidazolium as the cation with anions such as chloride, nitrate, and tetrafluoroborate have been synthesized by using the protonation method [25]. The most commonly used imidazolium ILs can also be prepared by the quaternization method [26], by heating 1-alkylimidazoles with haloalkanes at an appropriate temperature. In this procedure, the reaction temperature and the time required for completion greatly depends upon the length of the alkyl chain. In practice, some basic protocols have been employed in these reactions to make the reaction environment free of contaminants like, water and oxygen. Although haloalkanes are the primary alkylating reagents for quaternization reactions, nevertheless other reagents like methyl or ethyl triflate, methyl trifluoroacetate, methyl or octyl tosylate could be used to carry out the reaction. The advantage of using these alkylating reagents over the haloalkanes is that at the end of the chemical reactions, there would not be any unwanted by-products such as halides as found in case of the use of the latter.

The next process, i.e. the anion exchange could be approached through either of two methods. The“metathesis method” or the “acid-base neutralization method”. The first air and water stable ILs based on 1,3-dialkylmethylimidazolium cations were prepared through metathesis reaction between [EMIM]I and a number of silver salts (Ag[NO_3], Ag[NO_2], Ag_2[SO_4]) in methanol or aqueous methanol solution [27]. The first water-insoluble IL [EMIM][PF_6] had been synthesized from the metathesis reaction between [EMIM]Cl and HPF_6 [28]. In acid-base method, RTILs are formed from the reaction of halide salts with Lewis acids ($AlCl_3$). Figure 1.3 depicts a common route for the synthesis of ILs involving the cationization of the heteroatomic compound followed by anion metathesis reaction.

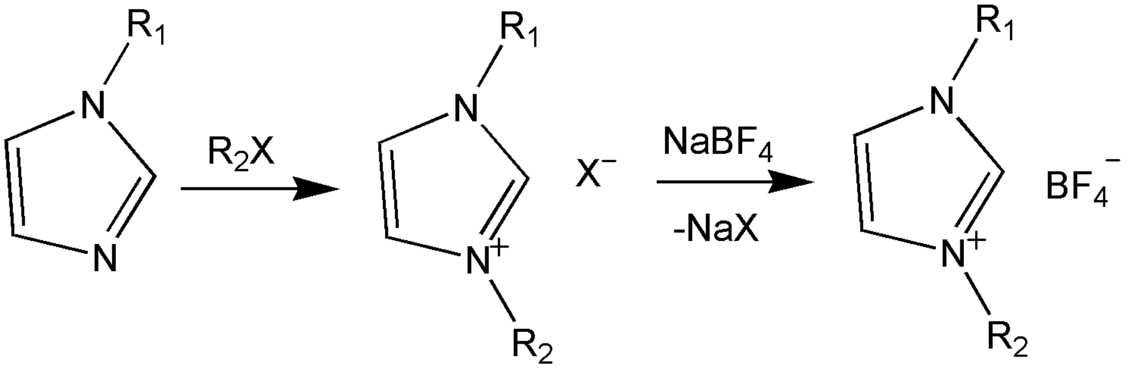

Figure 1.3: Synthesis of ionic liquids.

A third simple/direct way for synthesis of ionic liquid is the ”direct combination of a halide salt with a metal halide” [14].

1.1.2 Physical and Chemical Properties

Dielectric Constant

The dielectric constant of a substance is the ratio of its permittivity to that of free space. The solvation properties of RTILs depend greatly on the polarity of the liquid. Knowledge of polarity is of immense importance for designing task-specific ILs. The most common polarity scale relies on the static dielectric constant (ϵ_0), which reflects the polarization caused by the molecular dipole moment. Although the measurement of dielectric constant for a sample which is also conducting is not straightforward, many research groups have come up with methods to measure the dielectric constant of ILs experimentally as well as using simulations [29–34]. The dielectric constant of RTILs is found to fall in the range of 8-14, which is a moderate number and easy to handle, as substances with high dielectric constants break down more easily when subjected to intense electric fields. Table 1.1 compares the dielectric constants of RTILs against other common substances.

Materials	Dielectric constant(ϵ_0)
Vacuum	1.0
Air (dry)	1.0006
Polystyrene	2.6
Paper	3.6
Water	80
Ionic liquids	8-14

Table 1.1: Static dielectric constant of few substances.

Solvent Properties

The values of dielectric constant of RTILs from Table 1.1 reveal that RTILs are moderately polar. The polarity of RTILs influence their miscibility and solvating power with organic compounds. Due to the large difference in their polarities, non-polar solvents such as hexane and toluene are immiscible with RTILs. It has been found that carbon dioxide is soluble in many RTILs, whereas other gases such as hydrogen, carbon monoxide, and oxygen are not readily soluble. It has recently been shown that addition of carbon dioxide could enhance the solubility of other gases (oxygen and methane) in some RTILs [35]. Table 1.2 shows the miscibility of 1-*n*-butyl-3-methylimidazolium hexafluorophosphate [PF_6] with some of the volatile organic cosolvents.

Hydrophobicity/Hydrophilicity

Hydrophobicity or hydrophilicity of ILs is desired depending upon its applications. The nature of both cation and anion influence this property. For example, while both [bmim][Cl] and [bmim][BF_4] are soluble in water, [bmim][PF_6] and [bmim][NTf_2] are not [36]. As expected, the longer the alkyl chain on the cation is, the more hydrophobic the IL becomes; [bmim][BF_4] is soluble in water, while [omim][BF_4] is immiscible [37]. Until 2004, there was only one proven method available for quantifying these characteristics and it was being done by comparing the IL-water partitioning in a biphasic alcohol-water system. In 2004, Lee and workers came up with the technique of self-assembled monolayers (SAMs) to quantify the effects of anions on hydrophobicity and hydrophilicity [38].

Hygroscopicity is yet another important property of ILs in this context. It influences, among other quantities, their viscosity. It has been shown that ILs become less viscous with increasing water content [39, 40]. Hydrolysis may also occur in the presence of water in ILs.

Solvent	Miscibility
Water	Largely immiscible
CH_3OH	Miscible
CH_3CN	Miscible
Acetone	Miscible
CH_2Cl_2	Miscible
Toluene	Immiscible
Hexane	Immiscible

Table 1.2: Miscibility of [bmim][PF_6] with other cosolvents.

Volatility

Aprotic ILs are largely non-volatile [15], while protic ILs could be volatile as the acidic proton of the cation would combine with the basic anion to form neutral species which could evaporate. Molecular dynamics simulations of Maginn and co-workers on [bmim][PF_6] IL [41, 42], yield estimates of its vapour pressure to be as low as 10^{-11} Pa at 300 K, which in typical experimental environments (10^{-3} Pa and ambient temperature) is difficult to obtain and hence it was believed that ILs are non-volatile. Maginn *et al* [41, 42] have calculated the enthalpy and entropy of vapourization, from which the vapour pressure value is estimated. They also obtained very high cohesive energy density for the IL ($\sim$ 761 Jcm^{-3}), which comes mainly from the electrostatic interaction between the ions and hence results in the low vapour pressure. Recently, there were some notable experimental studies where the researchers were able to distill ILs at moderately high temperatures and low pressures without decomposing them. Thus, the ILs could be vapourized [43, 44], There are few excellent reviews addressing this important property of ILs [45, 46].

Melting Point and Liquid Density

The most important property of RTILs is the melting point temperature. ILs melt without decomposing or vapourizing. Due to the large molecular volumes over which the charge is distributed, inter-ion interaction is relatively weak which leads to a lower stability of their crystalline phase. Melting points can primarily be measured through differential scanning calorimetry (DSC) experiments.

The melting point of the ILs reduce with increase in the size of the cations and anions [10, 37, 47]. Other ways to lower the melting point could be introduction of ion flexibility, inefficiencies of packing, and non-charge bearing hydrocarbon groups. Symmetry of the ions has a major contribution in determining the melting point as well. Increasing symmetry in the ions increase melting points by enabling efficient packing in the crystal cell. It has also been observed that increase in the degree of chain branching increases the melting point. The thermal stability of ILs are usually high compared to other organic solvents.

Reported densities of RTILs vary between 1.1 gm/cc and 1.8 gm/cc. It has been observed that for a given anion, density of the ionic liquid decreases with increase in the alkyl chain lengths of the imidazolium based cation [20, 48, 49].

Viscosity

The internal friction of the fluid gives rise to the viscosity and it is the resistance of the fluid to flow. Fluids are divided into two groups based on their viscosity behaviour–Newtonian and non-Newtonian. The viscosity of Newtonian fluids is independent of the applied strain, whereas that for non-Newtonian liquids varies with the strain rate and can either thicken or thin with the applied strain. Within experimentally accessible strain rates, RTILs have been found to be Newtonian [4]. RTILs are also more viscous than most common molecular solvents. Viscosity is an important property as it controls the rate of a chemical reaction due to its strong effect on the rate of mass transport and also it has a strong impact on the diffusion mechanism of the system. The viscosity of RTILs could be in the range of 10 cP-500 cP. Viscosity of RTILs depend strongly on temperature and it decreases with increasing temperature [21, 50]. It has been observed that the presence of even a very small amount of impurity drastically alters the viscosity [39, 51]. Addition of 20 mol % of cosolvents such as water, acetone, ethanol, ethyl acetate, toluene etc. have shown to reduce the viscosity of [bmim][BF_4] by 50 % [39].

The size of ions plays an important role in determining the viscosity in ILs. For a fixed anion, the larger the alkyl group on the imidazolium cation, the larger is the viscosity. Whereas for a fixed cation, the trend does not depend entirely on the size of the anion, it also depends on the ability of the anion to form weak hydrogen bonds with the cation.

Conductivity

Electrical conductivity of a solvent is of great importance when it is used for electrochemical applications. It depends upon the available charge carriers and their mobility. Although RTILs are composed purely of ions, not all of them contribute to the measured total electrical conductivity. The smaller than expected ionic conductivity in ILs are due to the reduction in available charge carriers, which can be a consequence of ion pairing or aggregation or correlated ion motion. It has been observed that even a very small amount of impurity alters the conductivity significantly [52–54]. Seddon *et al* had reported that the presence of chloride ion decreased the conductivity while the presence of water increased it [39]. Generally the conductivity of ILs ranges from 10-30 mScm^{-1}, but recently ILs made up with $[(HF)_{2.3}F]^-$ anion have been shown to have high values, around 100 mScm^{-1} [55].

Table 1.3 lists the measured viscosity, conductivity, density for a group of imidazolium cation based RTILs [48, 56–62] at a pressure of 1 atmosphere.

Liquid Range

The liquid range of a solvent is the temperature span between the melting and boiling points of the solvent. In other words, it defines the range of temperatures within which the system remains in its liquid state. RTILs hold a relatively large liquid range as opposed to common molecular organic solvents; for example, water has a liquid range of 100 ^{o}C and dichloromethane has a liquid range of 145 ^{o}C, whereas for ILs the range can be as large as 400 ^{o}C [37] or more. The lower limit of the liquid range for RTILs extends due to the relative weak interaction between the ions and hence the lower temperature limit for solidification decreases. For molecular solvents, the upper limit of the liquid phase (boiling point) is vapourization, whereas for RTILs it is rather the thermal decomposition of ions as they are almost nonvolatile.

RTILs	Viscosity (Pa s)	Electrical conductivity (S/m)	Density (kg/m^3)
[emim] [DCA]	0.0145(298.1 K) [60]	2.928(298.1 K) [60]	1100.8(298.1 K) [60]
[emim] [BF$_4$]	0.036(298.1 K) [60]	1.57(298.1 K) [60]	1288.8(298.1 K) [60]
[emim] [PF$_6$]	0.0171(353.1 K) [56]	–	1421.8 (353.1 K) [59]
[emim] [NTf$_2$]	0.032(298.1 K) [60]	0.921(298.1 K) [60]	1519.3(298.1 K) [60]
[bmim] [DCA]	–	1.052(298.1 K) [62]	1058.0(297.1 K) [58]
[bmim] [BF$_4$]	0.0914(303.1 K) [56]	0.352(298.1 K) [61]	1202.08(298.1 K) [61]
[bmim] [PF$_6$]	0.249(298.1 K) [57]	0.146(298.1 K) [62]	1368(298.1 K) [57]
[bmim] [NTf$_2$]	0.04(303.1 K) [48]	0.4708(303.1 K) [48]	1439.7(303.1 K) [48]
[hmim] [NTf$_2$]	0.054(303.1 K) [48]	0.27(303.1 K) [48]	1360.8(303.1 K) [48]
[omim] [NTf$_2$]	0.071(303.1 K) [48]	0.165(303.1 K) [48]	1316.9(303.1 K) [48]

Table 1.3: Viscosity, electrical conductivity and density of a few RTILs. Value in parentheses is temperature.

Electrochemical Window

In electrochemistry, the potential range between which the substance does not get oxidized or reduced is defined as its electrochemical window. For their use in electrochemical applications, the stability of RTILs against high voltage differences is very important. It has been been found experimentally that RTILs do possess a comparatively large electrochemical window over the organic solvents. RTILs decompose when a voltage difference larger than 4-6 V is applied, which is the typical range of electrochemical window for RTILs [47, 63, 64]. The cathodic and anionic limits are determined by the reduction and oxidation of cations and anions respectively, which establishes the electrochemical potential range. Bonhote and coworkers [47] have studied a group of RTILs on platinum electrode and infer that the electrochemical window depends very much on the particular combinations of the ionic substituents along with the identity of the cations and anions. It has recently been shown that the electrochemical window also depends on the working electrode [65, 66].

1.1.3 Applications

Other than being unique solvents, RTILs are vastly used as electrolytes in lithium batteries, as lubricants, in sensors, in dye-sensitized solar cells, capacitors, synthesis of nanoparticles, multi-walled nanotubes etc. A brief descriptions on some of its applications is given below.

Solvents

RTILs are the main candidates for the replacement of volatile organic compounds to be used as solvents [3, 9, 14]. They are good solvents for both organic and inorganic solutes, and even for a few enzymes [67]. Solubility of gases like carbon dioxide, methane, ethane, argon, oxygen, hydrogen, nitrogen, carbon monoxide in RTILs, [bmim][PF_6] and [bmim][BF_4] have been studied by Maginn *et al* [68, 69]. Dissolution of carbon dioxide in RTILs have been studied [68–70]. Maginn and co-workers have examined the effect of the nature of anions on the gas solubility in RTILs and found that it contributes significantly. For example, they found bis(trifluoromethylsulfonyl)imide anion based RTILs had the largest affinity for carbon dioxide, irrespective of the nature of cations used [71]. RTILs are shown to be very good solvents for a few Diels-Alder reactions [72, 73] over molecular solvents. ILs are used as solvents in alkylation of sodium β-napthoxide, hydrogenation reactions, hydroformylation, dimerization of butadiene, Heck reactions, Friedel-Crafts acylation etc. [14].

Synthesis

Synthesis of many compounds in RTILs are being reported. There exist two volumes of a book dealing with a range of synthetic procedures to be adopted in

RTILs [4]. Their high heat capacity and ability to perform novel separations, enables the platform to conduct some reactions that are difficult to perform in water or even supercritical fluids. For example, the widely used Grignard reagents in synthesis processes are moisture sensitive. However, it has been shown that Grignard reactions can be carried out in phosphonium based ILs [23, 24]. RTILs are very effective in stabilizing metal nanoparticles [74, 75]. RTILs are also being routinely used in polymer synthesis and for biocatalysis processes.

Electrolytes

Due to their unique physico-chemical properties such as non-flammability, low vapour pressure, high conductivity, high stability, RTILs are one of the most promising electrolyte media in electrochemical devices. RTILs composed of imidazolium or pyrrolidinium cations with bis(trifluoromethanesulfonyl)imide (TFSI), bis(fluorosufonyl)imide anions are being greatly used as electrolytes without any solvent in rechargeable lithium ion batteries [76–83]. IL-based gel type membranes have currently emerged as good separators to be used in advanced lithium batteries for safety and reliability purposes over the liquid electrolytes [84–86].

Lubricants

Room temperature ionic liquids are shown to act as good lubricants for a variety of material-material contacts. 1-hexyl-3-methylimidazolium tetrafluoroborate ([HMIM][BF_4]) and 1-hexyl-3-ethylimidazolium tetrafluoroborate ([HEIM][BF_4]) were shown to be potent synthetic lubricants for steel/steel, steel/aluminum, steel/copper, steel/SiO_2, etc. These ILs showed excellent friction reduction, antiwear performance and high load-carrying capacity [87]. IL lubricants are used in three different ways: as base oils, additives and thin films [88]. It has been shown that due to the presence of the active element, Phosphorus, phosphonium based ILs shows better friction reduction and anti-wear ability than imidazolium based ILs [89, 90]. Depending upon the alkyl chain length of the cation, nature of the anion and the molecular polarity, this property can be tuned [91–94].

1.2 Studies on Structure, Dynamics, and Interfaces of RTILs

The structural and dynamical behaviour of RTILs are interesting due to the unique physical properties and the complex interactions between the constituent cations and anions. Since last decade, experimental and theoretical research on this topic has advanced our understanding on the microscopic details of the structure and dynamics.

Hamaguchi *et al* have carried out Raman spectroscopy and X-ray scattering experiments to obtain the crystal/liquid structure of a set of ILs [95–97]. Neutron scattering experiments too have been used to elucidate the intermolecular structure of many ILs [98–100]. The intermediate range order in ionic liquids is likely to be related to charge ordering. A chief observation from these studies is the existence of inter-ionic hydrogen bonding among the cation and anion [101–106].

The transport coefficients of ionic liquids and their dependence on pressure, temperature, density, and other quantities have been measured especially with NMR techniques [107–112]. It has been observed that inspite of having larger ionic radii and complex shapes, cations diffuse faster than anions in most of the ILs. Needless to state, this observation will not hold good if the mass of the cation is much larger than that of the anion. The response of viscosity to temperature and pressure has been measured by Kanakubo *et al* for a number of ILs, and it could be fitted to the Vogel-Fulcher-Tammann (VFT) equation [21,113–115]. The correlation between the molecular structure and physico-chemical properties is a well studied topic. Studies have been carried out to elucidate the effect of variation in the alkyl chain lengths of the cation and the nature of anions, on the volumetric, vibrational and transport properties [48,57,116,117]. The orientational dynamics of the ions were characterized by using NMR and optical Kerr effect experiments [118, 119]. Relaxation processes and the time scales associated with them in the ILs could be captured from neutron scattering, and dielectric relaxation experiments [99,120–122]. The presence of multiple relaxation mechanisms and the associated time scales have been determined through a Kohlrausch-Williams-Watts (KWW) fit to the relaxation data.

A large number of simulation studies on RTILs have been conducted to characterize their structural, dynamical, thermophysical, and transport properties. The first simulation in this regard was probably the one carried out by Lynden-Bell *et al* [123]. The microscopic details of the structure and interactions of ILs have been explored by using *ab-initio* molecular dynamics simulations and the presence of the strong hydrogen bonding interaction between the acidic hydrogen atom (hydrogen attached to the carbon on the imidazolium ring between the two nitrogen atoms) and the anion has been shown [124–134]. MD simulations turned out to be of great importance while determining the dynamical properties for the ILs. Transport properties such as diffusion coefficients for cations and anions, viscosity, thermal and electrical conductivity could be calculated using simulations for a variety of ILs and were found to match with experimental data [135–139]. Among all the transport properties, viscosity has gained special attention as it is a collective quantity and hence is challenging to calculate for viscous fluids. A number of studies have been devoted to measure the viscosity of RTILs and to monitor its response to various external influences [140–143].

The collective dynamics and correlated diffusion of the ions have been inferred from the difference between the actual transport coefficient values and the ones calculated using the Nernst-Einstein relation [144,145]. It has been observed that the correlations are very short-lived [146]. The cooperativity among the ions in RTILs has been studied by using density functional theory (DFT) based quantum chemical calculations [147] and a strong cooperativity is found in these cases. Heterogeneity in ion dynamics has been probed by calculating the non-Gaussian parameter in the structural relaxation [137,144,148–150]. The power spectrum for the individual ions and for the whole system have been calculated from the Fourier transform of the respective velocity auto-correlation functions in order to characterize the specific motions of the ions at particular frequencies [126,138,151,152]. The current status of ILs and the possibilities of studying them through using molecular simulations have been reviewed thoroughly by Maginn [153].

Numerous experimental and simulation studies have been carried out to characterize the structure (populations, orientation of ions, surface tension, electrostatic potential) and dynamics of RTILs at air, liquid, as well as solid interfaces. Sum frequency generation (SFG) vibrational spectroscopy, direct recoil spectroscopy (DRS), and X-ray reflectivity are some of the well known techniques used for this purpose. SFG studies on imidazolium cation based ILs at the air/IL, liquid/IL, solid/IL, interfaces have been conducted primarily to determine the orientation of cations and anions at the interfaces [154–165]. The conclusions from these studies are that both the ionic species are present at the interfacial region with the imidazolium ring lying flat along the surface plane and the butyl chain projecting out of the surface. X-ray reflectivity [166–170], neutron reflectrometry, DRS [171, 172] experiments have been carried out to obtain the properties at the IL interfaces. The air/IL interface studies have recently been summarized by Baldelli [173]. Surface-enhanced Raman scattering (SERS) has also been carried out at silver electrode/IL ([bmim][PF_6]) interface and the electrostatic potential has been determined at the interface [174]. Figure 1.4 shows a schematic depicting the general arrangement of ions at the ionic liquid-vapour interface.

A large number of simulations have been carried out in order to complement and support the experimental results. Simulation studies on vacuum/IL interface [175–180], liquid/IL interface [181–184], solid (rutile,gold,saffire,graphite)/IL interface [185–189] have revealed that the interface is occupied with both the cations and anions. Alkyl chains of the cations protrude out and constitute the outermost layer of the interface. Charge ordering is observed at the interfaces. The imidazolium cations are found to lie at the interface with their ring normals perpendicular and alkyl chains parallel to the surface normal. Thus, there is a segregation of polar (imidazolium ring and anion) and non-polar (alkyl groups) regions at the interface. It is also seen that the surface tension decreases with an increase in the alkyl chain length of the cation. The dynamics of the ions at these interfaces have also been determined through simulations [190, 191].

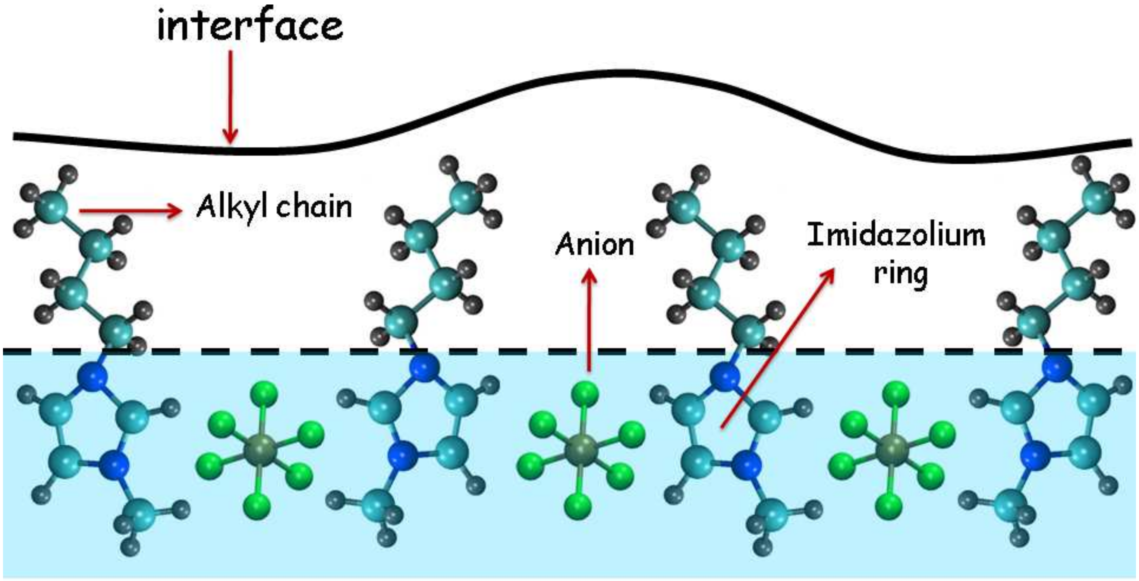

Figure 1.4: Schematic showing the arrangement of ions at the IL-vapour interface for [bmim][PF_6] liquid.

1.3 Methodology

Computer Simulations

Over the last several decades, computer simulations have played a major role in our understanding of the microscopic behaviour of substances in general and liquids in particular [192]. Simulations serve as a bridge between theory and experiment: a proposed theory could be tested by performing simulations using the same model, as it could be tested by conducting experiments. Another advantage of simulations is that they can be carried out at extreme conditions (like very high temperature and pressure) where experiment may not be possible. So, simulations are also termed as ”computer experiments”. Two main methods of simulations are – Molecular Dynamics (MD) and Monte Carlo (MC). MD method is deterministic while MC is based on stochastic events. The MD method has been employed to carry out the simulations in this thesis and a brief description is given below. The advantage of MD over MC is that, it is possible to obtain the dynamical properties of the system using MD simulations.

1.3.1 Molecular Dynamics Simulations

MD simulation technique is a numerical way to solve the classical Newton's equations of motion. Once the potential of interaction is available, for a simple atomic system, these can be formulated as,

$$\mathbf{F_i} = -\frac{\partial}{\partial \mathbf{r_i}} U \tag{1.1}$$

$$m_i \ddot{\mathbf{r}}_i = \mathbf{F_i} \tag{1.2}$$

where $\mathbf{F}_i$ is the force acting on the ith particle, $\mathbf{r}_i$ is the position and m$_i$ is the mass of ith particle. For a system consisting of N number of particles, the potential energy (U) will be a function of the coordinates, i.e., U($\mathbf{r}^N$), where; $\mathbf{r}^N$ = ($\mathbf{r}_1$, $\mathbf{r}_2$, $\mathbf{r}_3$,.....$\mathbf{r}_N$). The kinetic energy then would be given by, K($\mathbf{p}^N$) = $\sum_{i=1}^{N} \mathbf{p}_i^2/2m_i$, and

$\mathbf{p}^N = (\mathbf{p}_1,\ \mathbf{p}_2,\ \mathbf{p}_3, ...\mathbf{p}_N)$. The Hamiltonian $H(\mathbf{r}^N,\ \mathbf{p}^N)$ is represented as,

$$H(\mathbf{r^N}, \mathbf{p^N}) = U(\mathbf{r^N}) + \sum_{i=1}^{N} \mathbf{p_i}^2/2m_i \tag{1.3}$$

The Hamilton's equations for this system is given as,

$$\dot{\mathbf{r_i}} = \frac{\partial H}{\partial \mathbf{p_i}} = \frac{\mathbf{p_i}}{m_i} \tag{1.4}$$

$$\dot{\mathbf{p_i}} = -\frac{\partial H}{\partial \mathbf{r_i}} = \mathbf{F}_i \tag{1.5}$$

Thus, given the initial positions and momenta of the particles, these coupled equations of motion need to be integrated numerically to determine $\mathbf{r}_i$ and $\mathbf{p}_i$ as a function of time. To start a MD simulation, the initial positions of the system of interest is either taken from crystal databases (if one is reported) or can be generated by placing the atoms randomly in a lattice, after ensuring that there is no overlap between the positions of any two particles. The initial velocities are chosen at random from the Maxwell-Boltzmann distribution depending upon the desired temperature. The temperature of the system can be calculated by,

$$T(t) = \frac{1}{k_B} \sum_{i=1}^{N} \frac{m_i \mathbf{v_i}^2(t)}{N_f} \tag{1.6}$$

where, k_B is the Boltzmann constant, $\mathbf{v}_i$ is the velocity of particle "i", and N_f is the number of degrees of freedom. To retain the temperature at a constant value (T), the velocities are rescaled with a factor $(T/T(t))^{1/2}$ (or, one can use extended system MD methods; see later).

To get rid off the surface effects on the system, the simulation cell is replicated periodically infinite times in all dimensions (periodic boundary conditions) [192]. During the course of simulation, if a particle moves out of the cell, its periodic image from the neighbouring cell enters into it and the number density in the central simulation cell is conserved. In that case, the force calculation becomes of the order of N^2 for a system of N particles, after implementing the minimum image convention [193]. Minimum image convention takes care that every particle interacts with the closest atoms or the images from the periodic array. Thus, the force calculation turns out to be the most expensive part in a simulation, in terms of the computation time. Hence, an approximatation on the interaction could be made to make the force evaluation faster, by defining a cut-off distance (r_c). The interactions among the particles that are present within the cut-off distance are taken into account for the force calculation. If a pair distance r is greater than r_c, its contribution to the total energy is zero. r_c should be less than half the box length in case of a cubic box, to be consistent with the minimum image convention.

The integration time step of a MD simulation must be chosen judiciously. The necessary criterion is that it should be much smaller than the fastest process occuring in the system. But in order to generate longer trajectories of the dynamics, it should be large enough, for the sake of efficiency. While choosing larger time steps, accuracy of numerical integration should not be lost. To handle systems involving interactions of multiple time scales efficiently, multiple timestep algorithms have been developed [194]. The idea behind these algorithms is to treat the short-range forces very frequently with time, which requires a small integration time step and the relatively slow varying long-range forces can be handled with a larger time step and less frequent force evaluations.

Several algorithms have been developed to solve the equations of motion over time, *e.g.*, position Verlet [195, 196] algorithm, leap frog algorithm [197], velocity Verlet [198] algorithm, Gear predictor-corrector algorithm etc. Verlet algorithms are the simplest and efficient for most of the MD simulations. Other important criteria which makes it a reliabale one are its time reversal, area preserving and energy conservation qualities. The velocity Verlet method has been used in all the simulations in this thesis.

Velocity Verlet Algorithm

$$\mathbf{p_i}(t+\frac{1}{2}\delta t) = \mathbf{p_i}(t) + \frac{1}{2}\delta t\mathbf{F_i}(t) \tag{1.7}$$

$$\mathbf{r_i}(t+\delta t) = \mathbf{r_i}(t) + \delta t\mathbf{p_i}(t+\frac{1}{2}\delta t)/m_i \tag{1.8}$$

$$\mathbf{p_i}(t+\delta t) = \mathbf{p_i}(t+\frac{1}{2}\delta t) + \frac{1}{2}\delta t\mathbf{F_i}(t+\delta t) \tag{1.9}$$

1.3.2 Constant Temperature MD Simulations

The Hamilton's (or Newton's) equation of motion generate a trajectory in microcanonical or the constant NVE ensemble. However, laboratory experiments are carried out at constant temperature and constant pressure.

In the canonical ensemble (constant NVT), the temperature of a system is maintained at a constant value by coupling the system to bath which is at a temperature T. Particle exchange between the bath and system is not allowed, but energy transfer is allowed. Many methods have been proposed to carry out constant-temperature simulations, such as the constraint method [199, 200], stochastic method [201, 202], and extended-system methods [203–206]. The extended system is a more stable and efficient approach. A brief note on the extended system Nosé-Hoover chain method is given below.

Martyna *et al* [207–209] came up with the Nosé-Hoover chain method for the generation of a MD trajectory in the canonical ensemble. In this formalism, the bath is described by a set of coupled thermostats. The thermostat variables are η_1, η_2,..., η_M and their conjugate momenta are p_{η_1}, p_{η_2},..., p_{η_M}. The equations of motion are given by,

$$
\begin{aligned}
\dot{\mathbf{r}}_i &= \frac{\mathbf{p}_i}{m_i} \\
\dot{\mathbf{p}}_i &= -\frac{\partial U}{\partial \mathbf{r}_i} - \frac{p_{\eta_1}}{Q_1}\mathbf{p}_i \\
\dot{\eta}_i &= \frac{p_{\eta_i}}{Q_i} \\
\dot{p}_{\eta_1} &= \sum_{i=1}^{N} \frac{\mathbf{p}_i}{m_i} \cdot \mathbf{p}_i - N_f k_B T - \frac{p_{\eta_2}}{Q_2} p_{\eta_1} \\
\dot{p}_{\eta_i} &= \frac{p^2_{\eta_{i-1}}}{Q_{i-1}} - k_B T - \frac{p_{\eta_{i+1}}}{Q_{i+1}} p_{\eta_i} \qquad i = 2, ..., M-1 \\
\dot{p}_{\eta_M} &= \frac{p^2_{\eta_{M-1}}}{Q_{M-1}} - k_B T
\end{aligned}
\tag{1.10}
$$

where $-\frac{\partial U(\mathbf{r}_i)}{\partial \mathbf{r}_i}$ represents the force on particle i due to all the other particles in the system and N_f is the number of degrees of freedom. These equations known as the Nosé-Hoover chain (NHC) or Martyna-Tuckerman-Klein (MTK) equations. The conserved Hamiltonian then is given by:

$$
H' = \sum_{i=1}^{N} \frac{\mathbf{p}_i^2}{2m_i} + U(\mathbf{r}) + \sum_{i=1}^{M} \frac{p^2_{\eta_i}}{2Q_i} + N_f k_B T \eta_1 + \sum_{i=2}^{M} k_B T \eta_i \tag{1.11}
$$

1.3.3 Force Field

Force field refers to the functional form and set of parameters that describes the potential energy of a system of atoms (or molecules) to carry out classical MD/MC simulations. The functional form and parameter set could be derived either based on experimental data or from high-level quantum mechanical calculations or a mix of both. The total potential energy of a system of molecules has contributions from the bonded interactions (atoms linked by covalent bonds) as well as from nonbonded long-range interactions (electrostatic and van der Waals) between the atoms. Hence, in the force field parametrization, the total potential energy is written as,

E_{total}=E_{bonded}+$E_{nonbonded}$

where,

E_{bonded}=E_{bond}+E_{angle}+$E_{torsion}$

$E_{nonbonded}$=$E_{electrostatics}$+$E_{vanderWaals}$

The functional forms for bond and angle energies are usually modelled as harmonic oscillators. Torsional interactions could be represented in a variety of ways such as cosine series, power series etc. Improper torsions are also required to enforce planarity of ring molecules. Further, atoms could interact via electrostatic forces. van der Waals interactions can be represented by Lennard-Jones (12-6) terms. Some popular classical force fields are AMBER [210], CHARMM [211], GROMACS, GROMOS, OPLS [212] etc.

Potential parameters for RTILs

A large number of force field parameters have been developed in recent years to mimic the structural and dynamical behaviour of RTILs computationally. A well used force field is that of Lopes and co-workers [213–218]. Other force fields include that of Wang and co-workers [219–221], Stassen and co-workers [222, 223], and many others for specific liquids [22, 41, 123, 139, 224–229]. While the interaction terms among the various force fields are nearly the same, the parameters vary. The force field development methods and the associated limitations are reviewed by Hunt [230].

Given below is an expression for the potential energy of a system of atoms, which includes bonded and non-bonded interactions and is in the form of the CHARMM force field.

$$\begin{aligned} U\left(\{\mathbf{r}\}\right) &= \frac{1}{2}\sum_{ij}^{bonds} K_r^{ij}\left(\mathbf{r}_{ij}-\mathbf{r}_{ij}^0\right)^2 + \frac{1}{2}\sum_{ijk}^{angles} K_\theta^{ijk}\left(\theta_{ijk}-\theta_{ijk}^0\right)^2 \\ &+ \sum_{ijkl}^{dihedrals}\sum_{n=0}^{6} a_n^{ijkl} cos^n \phi_{ijkl} + \frac{1}{4\pi\epsilon_0}\sum_{i}^{N}\sum_{j>i}^{N}\frac{q_i q_j}{r_{ij}} \\ &+ \sum_{i}^{N}\sum_{j>i}^{N} 4\epsilon_{ij}\left[\left(\frac{\sigma_{ij}}{r_{ij}}\right)^{12} - \left(\frac{\sigma_{ij}}{r_{ij}}\right)^{6}\right] \end{aligned} \tag{1.12}$$

where i, j, k, and l denote atom indices, q_i and q_j are the partial charges of i^{th} and j^{th} atom respectively, ϵ_0 is the permittivity of free space, K_r^{ij} and K_θ^{ijk} are the stretching and bending force constants respectively, ϕ_{ijkl} is the dihedral angle, and r_{ij} is the interatomic distance between atoms i and j. The non-bonded interaction comes into picture only for those atoms separated by more than three bonds. However, in some force fields such as AMBER and OPLS, non-bonded interactions may be calculated for atoms separated by more than two bonds, with a scale factor.

1.3.4 Long Range Interactions

A long-range potential is defined as one in which the interaction decays no faster than r^{-d}, where d is the dimensionality of the system. Coulombic interaction comes under this catagory, as it falls as r^{-1}. In this potential, significant contributions to the total potential energy exist even for distances greater than the cutoff distance ($<$ box-length/2). The Coulomb sum is also conditionally convergent. One way to solve these problems is to increase the number of particles (N) sufficiently large, so that screening by neighbours could decrease the range of interaction. But as MD simulation is a $O(N^2)$ problem, the resulting computational cost would be very expensive. Hence, methods to exactly treat the long range nature of the electrostatic interactions have been developed. These include: Ewald summation technique, particle mesh Ewald(PME), particle-particle particle-mesh (PPPM). A brief note on the Ewald sum method is given below.

Ewald Summation Method

The Ewald sum is a lattice sum method, which includes the interaction of a particle with all other particles in the system and their periodic images. Suppose a periodic system consists of N point charges q_1, q_2,.....,q_N, located at positions $\mathbf{r}_1$**,** $\mathbf{r}_2$**,...,**$\mathbf{r}_N$ respectively. The total electrostatic potential energy of the system would be,

$$U_{coul}(\mathbf{r}) = \frac{1}{2}\frac{1}{4\pi\epsilon_0}\sum_{n}\sum_{i=1}^{N}\sum_{j=1}^{N}\frac{q_iq_j}{r_{nij}} \tag{1.13}$$

where $r_{nij} = |\mathbf{r_i} - (\mathbf{r_j} + n_1\mathbf{a_1} + n_2\mathbf{a_2} + n_3\mathbf{a_3})|$, and the sum over n is summation over all periodic boxes. The basic aim behind this method is to split the Coulombic sum given by Eq. 1.13 into short and long-range parts. In this method, each point charge is surrounded by an artificial charge distribution of equal magnitude and opposite sign with a radial spreading of the charge (normally this distribution is taken to be a Gaussian). In this manner, the added charge distribution screens the ionic interactions making them short-ranged. The total screened potential is calculated over all the atoms in the central box and all its images in real space. The pseudo charge distribution is cancelled by summing it up in the reciprocal space. Thus, the total Coulombic energy can be expresses as,

$$\begin{aligned} U_{coul}(\mathbf{r}) = \frac{1}{4\pi\epsilon_0}\sum_{i=1}^{N}\sum_{j>i}^{N}\frac{q_iq_j}{r_{ij}}erfc(\zeta r_{ij}) + \frac{1}{2V\epsilon_0}\sum_{k\neq 0}\frac{\exp(\frac{k^2}{4\zeta^2})}{k^2}|\sum_{j=1}^{N}q_je^{-i\mathbf{k}.\mathbf{r_j}}|^2 \\ -\frac{\alpha}{4\pi^{3/2}\epsilon_0}\sum_{j=1}^{N}q_j^2 - \frac{1}{4\pi\epsilon_0}\sum_{i=1}^{N}\sum_{j>i}^{bonded}\frac{q_iq_j}{r_{ij}}erf(\zeta r_{ij}) \end{aligned} \tag{1.14}$$

where erfc(x) is the complimentary error function, which is defined as,

$$erfc(x) = 1 - \sqrt{\frac{2}{\pi}}\int_0^x e^{-x^2}dx \tag{1.15}$$

and it goes to zero for large values of x. ζ is called the Ewald parameter. The third term in equation 1.14 is the self-energy term, which has to be subtracted from the total reciprocal energy. The last term in Eq. 1.14 takes care of the fact that atoms belonging to same molecule are allowed to interact via the non-bonded potential if separated by more than three bonds.

1.4 Analysis

MD simulations proceed by following the procedure described above. A trajectory of atomic positions and velocities is generated in the appropriate ensemble. The equilibration of the system is said to be achieved when the properties of the system no longer change with time. Then follows the MD runs to generate trajectories for analysis. In order to measure any observable quantity, first of all it should be expressed as a function of positions or velocities. Some of the real experimental observable thermodynamic properties, such as the temperature (T), pressure (P), heat capacity (C_v) etc. can be measured directly from MD simulations [231].

$$T = \frac{\langle 2K \rangle}{N_f} \tag{1.16}$$

$$P = \rho k_B T + \frac{1}{dV} \langle \sum_{i<j} F(r_{ij}).r_{ij} \rangle \tag{1.17}$$

$$\langle K^2 \rangle_{NVE} - \langle K \rangle^2_{NVE} = \frac{3k_B^2 T^2}{2N}(1 - \frac{3k_B}{2C_v}) \tag{1.18}$$

where, K is the kinetic energy, ρ is the density, d is the dimensionality of the system and $F(r_{ij})$ is the force between particles i and j at a distance r_{ij}.

A very important structural property called the “radial distribution function”, g(r) can be measured directly from the simulations. It gives the average number density of particles at a distance r from a given particle and is normalized by the density at the same distance r for an ideal gas. Hence, it plays a central role in liquid state physics. This can be compared with the experimentally obtained structure factors, as g(r) is the Fourier transform of the structure factor.

Apart from thermodynamic and structural properties, MD simulations allow one to obtain various dynamical quantities as well. The transport properties such as diffusion coefficient, viscosity, thermal, and electrical conductivity etc., can be obtained through various time correlation functions [232–234].

Time Correlation Functions (TCF)

The general expression for a TCF is,

$$C_{AB}(t) = \frac{\langle C_A(t).C_B(0)\rangle}{C_A(0).C_B(0)} \tag{1.19}$$

Where C_A(t), C_B(t) are the values of the variables C_A and C_B at time 't' and $C_A(0)$, $C_B(0)$ are values at time '0' respectively. For identical variables, the function is called as an auto correlation function (C_{AA}). TCF lies between 0 and 1, with values close to zero implying no correlation and values close to one indicating high degree of correlation. TCFs depict the dynamics in a fluid very well. The macroscopic transport coefficients are directly related to the time integrals of the TCFs through linear response theory. In general, transport coefficients are defined as the response of a system to a perturbation. For instance, diffusion coefficient relates the particle flux to the concentration gradient. For the dynamic variable A(t), the transport coefficient (γ) can either be expressed as the infinite time integral of an auto correlation function (this formulation is called the Green-Kubo formula) or it can be formulated in terms of the equivalent Einstein relation.

A general Green-Kubo relation is given by,

$$\gamma = \int_0^\infty \langle \dot{A}(t).\dot{A}(0)\rangle dt \tag{1.20}$$

whereas the corresponding Einstein relation is

$$2t\gamma = \langle (A(t) - A(0))^2 \rangle \tag{1.21}$$

where t is the time, depicting the long-time behaviour (asymptotic) value of the dynamic variable.

The Green-Kubo formula for diffusion coefficient (D) needs velocity as the dynamic variable and is given by

$$D = \frac{1}{3}\int_0^\infty \langle \mathbf{v_i}(t).\mathbf{v_i}(0) \rangle dt \tag{1.22}$$

where v$_i$(t) is the velocity of particle i. The corresponding Einstein relation is given by,

$$2tD = \frac{1}{3}\langle |\mathbf{r_i}(t) - \mathbf{r_i}(0)|^2 \rangle \tag{1.23}$$

where r$_i$(t) is the position of particle i. For a system consisting of N number of particles, the time averages are computed for each of the particles and then added up together, divided by N, to obtain statistical accuracy.

The power spectra (vibrational density of states, C(ω)) could be obtained by taking the Fourier transform of the normalized velocity autocorrelation function (C(t)). C(ω) is defined as,

$$C(\omega) = \int_{-\infty}^{\infty} C(t) e^{-i\omega t} dt \tag{1.24}$$

and C(t) is defined as,

$$C(t) = \frac{\langle \mathbf{v_i}(t) \cdot \mathbf{v_i}(0) \rangle}{\langle \mathbf{v_i}(0) \cdot \mathbf{v_i}(0) \rangle} \tag{1.25}$$

Viscosity is the ratio of shear stress induced by an applied strain. The correlation function associated with shear viscosity is the stress-stress time correlation function

(C_P(t)), which is defined as,

$$C_P(t) = \langle P_{\alpha\beta}(t) P_{\alpha\beta}(0) \rangle \tag{1.26}$$

where the subscripts denote any of the three Cartesian axes and the angular brackets imply averaging over initial times "0" and over the three distinct pairs of Cartesian components, xy, yz and zx. The shear viscosity at zero shear rate is calculated using the Green-Kubo relation,

$$\eta = \lim_{t_{max}\to\infty} \eta'(t_{max}) = \lim_{t_{max}\to\infty} \frac{V}{k_B T} \int_0^{t_{max}} C_P(t) dt \tag{1.27}$$

The equivalent Einstein formulation for shear viscosity is given by,

$$2t\eta = \frac{V}{k_B T} \langle (\zeta_{\alpha\beta}(t) - \zeta_{\alpha\beta}(0))^2 \rangle \tag{1.28}$$

In this case,

$$P_{\alpha\beta} = \frac{1}{V} \left(\sum_i v_{i\alpha} v_{i\beta} + \sum_i r_{i\alpha} f_{i\beta} \right) \tag{1.29}$$

is the off-diagonal ($\alpha \neq \beta$) element of the pressure tensor and

$$\zeta_{\alpha\beta} = \frac{1}{V} \sum_i r_{i\alpha} p_{i\beta} \tag{1.30}$$

The Green-Kubo relation for electrical conductivity (σ_e) is the integration of current-current correlation function and is given by,

$$\sigma_e = \frac{1}{V k_B T} \int_0^{\infty} \langle j_x^{el}(0) j_x^{el}(t) \rangle dt \tag{1.31}$$

where,

$$j_x^{el} = \sum_{i=1}^{N} q_i {v_i}^x \tag{1.32}$$

The Einstein relation is given by,

$$\sigma_e = \lim_{t\to\infty} \frac{e^2}{6tVK_BT} \langle \sum_{i=1}^{N}\sum_{j=1}^{N} q_i q_j * ([\mathbf{r_i}(t) - \mathbf{r_i}(0)].[\mathbf{r_j}(t) - \mathbf{r_j}(0)]) \rangle \tag{1.33}$$

The dynamic structure factor (S($\mathbf{k}$,ω)), which is measured in x-ray and neutron scattering experiments could be calculated from simulations by taking a temporal Fourier transform of a time correlation function called the intermediate scattering function (F($\mathbf{k}$,t)). F($\mathbf{k}$,t) is the density autocorrelation function, where the density ($\rho(\mathbf{k})$) is defined as,

$$\rho(\mathbf{k}) = \sum_{i=1}^{N} \exp(-i\mathbf{k}\cdot\mathbf{r_i}) \tag{1.34}$$

Intermediate scattering function (F($\mathbf{k}$,t)) is then given by,

$$F(\mathbf{k},t) = \frac{1}{N}\langle \rho(\mathbf{k},t)\rho(-\mathbf{k},0)\rangle \tag{1.35}$$

Dynamic structure factor (S($\mathbf{k}$,ω)) is then could be written as,

$$S(\mathbf{k},\omega) = \frac{1}{2\pi}\int_{-\infty}^{\infty} e^{-i\omega t} F(\mathbf{k},t)dt \tag{1.36}$$

1.5 Softwares and Hardwares used

All the classical molecular dynamics simulations studies mentioned in this thesis have been carried out by using LAMMPS program [235]. CPMD [236] program has been used for a few calculations. All the analysis of the MD trajectory have been carried with home developed codes, mostly using Fortran. Xmgr, Xmgrace, and Gnuplot software have been used for plots. Visualization softwares VMD, JMOL, Molden, have been used for visualization of the coordinates. The long analysis trajectories for the large systems studied in this thesis, required intense computational resources. The computations were carried out on our group's dedicated clusters as well as on the center's (JNCASR) clusters. The groups' clusters used are: a 10 node Xeon cluster (Nandini), a 32 processor Xeon cluster (Shabala), a 184 Harpertown processor cluster (Kamadhenu) and the center's 512 Woodcrest core cluster (Sampige).

1.6 Scope of the Thesis

The theme of this thesis is to examine the influence of inter-ionic interactions and structure of molecules on the complex dynamics and interfacial properties of RTILs using classical MD simulations. Chapter 2 describes a simulation study to explore the rich dynamics of an RTIL, [bmim][PF_6]. It demonstrates that the dynamical heterogeneity observed in the motion of ions in this system is correlated to the local structural heterogeneity present in the system. In Chapter 3, the far infra-red region of the vibrational spectra of some RTILs has been investigated by using classical MD simulations and DFT based calculations. Results are analyzed using velocity time correlation functions as well as through normal mode analysis. Chapter 4 deals with the study of ionic liquid-vapour interfaces where the effect of cation symmetry on the interfacial properties has been addressed. The last chapter, presents results of MD simulation studies on free-standing, large clusters of RTILs. Along with the characterization of the curved surface of the RTILs, effective interaction potentials between the clusters have been obtained as a function of the distance between their center of masses.

Bibliography

[1] M. Lancaster, *Green Chemistry : An introductory Text, Royal Society of Chemistry*, (Cambridge, UK, 2002).

[2] L.A. Blanchard, D. Hancu, E.J. Beckman, J.F. Brennecke, *Nature*, **399**, 28, (1999).

[3] R.A. Sheldon, *Green Chem.*, **7**, 267, (2005).

[4] P. Wasserscheid and T. Welton, Eds., *Ionic Liquids in Synthesis, Wiley-VCH Verlag*, (Weinheim, 2003).

[5] F.M. Kerton, *Alternatives Solvents for Green Chemistry, Royal Society of Chemistry*, (Cambridge, UK, 2009).

[6] C.A. Angell, W. Xu, M. Yoshizawa, J.-P. Belieres, *Ionic Liquids, Eds. H. Oye, A. Jagtoyen et al.,* pp.389-398.

[7] C.A. Angell, N. Byrne, J.-P. Belieres, *Acc. Chem. Res.*, **40**, 1228, (2007).

[8] P. Walden, *Bull. Acad. Imper. Sci.*, (St. Petersburg), 1800, (1914).

[9] M.J. Earle, K.R. Seddon, *Pure Appl. Chem.*, **72**, 1391, (2000).

[10] J.G. Huddleston, A.E. Visser, W.M. Reichert, H.D. Willauer, G.A. Broker, R.D. Rogers, *Green Chem.*, **3**, 156, (2001).

[11] D.R. Lide, *Handbook of chemistry and physics*, (CRC Press, Boca Raton, (2004)).

[12] S. Zahn, F. Uhlig, J. Thar, C. Spickermann, B. Kirchner, *Angew. Chem. Int. Ed.*, **47**, 3639, (2008).

[13] B. Kirchner, *Ionic Liquids (Topics in Current Chemistry), Springer*, (2009).

[14] T. Welton, *Chem. Rev.*, **99**, 2071, (1999).

[15] R.D. Rogers, K.R. Seddon, *Science*, **302**, 792, (2003).

[16] F. Endres, S. Zein El Abedin, *Phys. Chem. Chem. Phys.*, **8**, 2101, (2006).

[17] P. Wasserscheid, *Nature*, **439**, 797, (2006).

[18] A.G. Fadeev, M.M. Meagher, *Chem. Commun.*, 295, (2001).

[19] M.C. Buzzeo, R.G. Evans, R.G. Compton, *ChemPhysChem*, **5**, 1106, (2004).

[20] S.V. Dzyuba, R.A. Bartsch, ChemPhysChem **3**, 161 (2002).

[21] K. R. Harris, L. A. Woolf, M. Kanakubo, *J. Chem. Eng. Data*, **50**, 1777, (2005).

[22] N.M. Micaelo, A.M. Baptista, C.M. Soares, *J. Phys. Chem. B*, **110**, 14444, (2006).

[23] T. Ramnial, S.A. Taylor, M.L. Bender, B. Gorodetsky, P.T.K. Lee, D.A. Dickie, B.M. McCollum, C.C. Pye, C.J. Walsby, J.A.C. Clyburne, *J. Org. Chem.*, **73**, 801, (2008).

[24] T. Ramnial, D.D. Ino, J.A.C. Clyburne, *Chem. Commun.*, 325, (2005).

[25] C.K. Lee, H.W. Huang, I.J.B. Lin, *Chem. Commun.*, 1911, (2000).

[26] Z. Fei, D. Zhao, R. Scopelliti, P.J. Dyson, *Organometallics*, **23**, 1622, (2004).

[27] J.S. Wikes, M.J. Zaworotko, *Chem. Commun.*, 965, (1992).

[28] J. Fuller, R.T. Carlin, H.C. DeLong, D. Harworth, *Chem. Commun.*, 299, (1994).

[29] H. Weingärtner, *Z. Phys. Chem.*, **220**, 1395, (2006).

[30] H. Weingärtner, *J. Phys. Chem. B*, **111**, 4775, (2007).

[31] S. Schrödle, G. Annat, D.R. MacFarlane, M. Forsyth, R. Buchner, G. Hefter, *Chem. Commun.*, 1748, (2006).

[32] A. Stoppa, J. Hunger, R. Buchner, G. Hefter, A. Thoman, H. Helm, *J. Phys. Chem. B*, **112**, 4854, (2008).

[33] T. Singh, A. Kumar, *J. Phys. Chem. B*, **112**, 12968, (2008).

[34] C. Schröder, T. Rudas, O. Steinhauser, *J. Chem. Phys.*, **125**, 244506, (2006).

[35] D.G. Hert, J.L. Anderson, S. Aki, J.F. Brennecke, *Chem. Commun.*, 2603, (2005).

[36] C.F. Poole, *J. Chromatogr. A*, **1037**, 49, (2004).

[37] J.D. Holbrey, K.R. Seddon, *J. Chem. Soc., Dalton Trans.*, 2133, (1999).

[38] B.S. Lee, Y.S. Chi, J.K. Lee, I.S.Choi, C.E. Song, S.K. Namgoong, S. lee, *J. Am. Chem. Soc.*, **126**, 480, (2004).

[39] K.R. Seddon, A. Stark, M. Torres, *Pure Appl. Chem.*, **72**, 2275, (2000).

[40] M. Kanakubo, T. Umecky, T. Aizawa, Y. Kurata, *Chem. Lett.*, **34**, 324, (2005).

[41] T.I. Morrow, E.J. Maginn, *J. Phys. Chem. B*, **106**, 12807, (2002).

[42] J.K. Shah, J.F. Brennecke, E.J. Maginn, *Green Chem.*, **4**, 112, (2002).

[43] Y.U. Paulechka, D.H. Zaitsau, G.J. Kabo, A.A. Strechan, *Thermochim. Acta*, **439**, 158, (2005).

[44] M.J. Earle, J.M.S.S. Esperanca, M.A. Gilea, J.N.C. Lopes, L.P.N. Rebelo, J.W. Magee, K.R. Seddon, J.A. Widegren, *Nature*, **439**, 831, (2006).

[45] R. Ludwig, U. Kragl, *Angew. Chem. Int. Ed.*, **46**, 6582, (2007).

[46] J.M.S.S. Esperanca, J.N.C. Lopes, M. Tariq, L.M.N.B.F. Santos, J.W. Magee, L.P.N. Rebelo, *J. Chem. Eng. Data*, **55**, 3, (2010).

[47] P. Bonhote, A. Dias, N. Papageorgiou, K. Kalyanasundaram, and M. Grätzel, *Inorg. Chem.*, **35**, 1168, (1996).

[48] H. Tokuda, K. Hayamizu, K. Ishii, Md. A. B. H. Susan, M. Watanabe, *J. Phys. Chem. B*, **109**, 6103, (2005).

[49] C. Kolbeck, J. Lehmann, K. R. J. Lovelock, T. Cremer, N. Paape, P. Wasserscheid, A. P. Fröba, F. Maier, H.-P. Steinrück, *J. Phys. Chem. B*, DOI:10.1021/jp1068413, (2010).

[50] S.N. Baker, G.A. Baker, M.A. Kane, F.V. Bright, *J. Phys. Chem. B*, **105**, 9663, (2001).

[51] J.A. Widegren, A. Laesecke, J.W. Magee, *Chem. Commmun.*, 1610, (2005).

[52] J.A. Widegren, E.M. Saurer, K.N. Marsh, J.W. Magee, *J. Chem. Thermodynam.*, **37**, 569, (2005).

[53] R.L. Perry, K.M. Jones, W.D. Scott, Q. Liao, C.L. Hussey, *J. Chem. Eng. Data*, **40**, 615, (1995).

[54] Q. Liao, C.L. Hussey, *J. Chem. Eng. Data*, **41**, 1126, (1996).

[55] R. Hagiwara, K. Matsumoto, Y. Nakamori, T. Tsuda, Y. Ito, H. Matsumoto, K. Momota, *J. Electrochem. Soc.*, **140**, D195, (2003).

[56] K. R. Seddon, A. Stark, M. -J. Torres, *ACS Symp. Ser.*, **819**, 34, (2002).

[57] H. Tokuda, S. Tsuzuki, Md. A. B. H. Susan, K. Hayamizu, M. Watanabe, *J. Phys. Chem. B*, **110**, 19593, (2006).

[58] C. P. Fredlake, J. M. Crosthwaite, D. G. Hert, S. N. V. K. Aki, J. F. Brennecke, *J. Chem. Eng. Data*, **49**, 954, (2004).

[59] R. Taguchi, H. Machida, Y. Sato, R. L. Smith, Jr., *J. Chem. Eng. Data*, **54**, 22, (2009).

[60] C. Schreiner, S. Zugmann, R. Hartl, H. J. Gores, *J. Chem. Eng. Data*, **55**, 1784, (2010).

[61] A. Stoppa, O. Zech, W. Kunz, R. Buchner, *J. Chem. Eng. Data*, **55**, 1768, (2010).

[62] O. Zech, A. Stoppa, R. Buchner, W. Kunz, *J. Chem. Eng. Data*, **55**, 1774, (2010).

[63] B. D. Fitchett, T. N. Knepp, J. C. Conboy, *J. Electrochem. Soc.*, **151**, E219, (2004).

[64] M.C. Buzzeo, C. Hardacre, and R.G. Compton, *ChemPhysChem*, **7**, 176, (2006).

[65] C. Zhao, G. Burrell, A.A.J. Torriero, F. Separovic, N.F. Dunlop, D.R. MacFarlane, and A.M. Bond, *J. Phys. Chem. B*, **112**, 6923, (2008).

[66] E.I. Rogers, B. Sijukie, C. Hardacre, and R.G. Compton, *J. Chem. Eng. Data*, **54**, 2049, (2009).

[67] R.A. Sheldon, R. M. Lau, M.J. Sorgedrager, F. van Rantwijk, K.R. Seddon, *Green Chem.*, **4**, 147, (2002).

[68] J. L. Anthony, E. J. Maginn, J. F. Brennecke, *J. Phys. Chem. B*, **106**, 7315, (2002).

[69] J.L. Anthony, J.M. Crosthwaite, D.G. Hert, S.N.V.K. Aki, E.J. Maginn, J.F. Brennecke, *Phase Equilibria of Gases and Liquids with 1-N-Butyl-3-Methylimidazolium Tetrafluoroborate. In Ionic Liquids as Green SolVents: Progress and Prospects*, Eds. R.D. Rogers, K.R. Seddon, ACS Symposium Series 856; American Chemical Society: Washington, DC, 110, (2003).

[70] L.M. Galan Sanchez, G.W. Meindersma, A.B. de Haan, *Chem. Eng. Res.*, **85**, 31, (2007).

[71] J. L. Anthony, J. L. Anderson, E. J. Maginn, J. F. Brennecke, *J. Phys. Chem. B*, **106**, 6366, (2005).

[72] M.J. Earle, P.B. McCormac, and K.R. Seddon, *Green Chem.*, **1**, 23, (1999).

[73] T. Fisher, A. Sethi, T. Welton, and J. Woolf, *Tetrahedron Lett.*, **40**, 793, (1999).

[74] E. Redel, R. Thomann, C. Janiak, *Chem. Commun.*, 1789, (2008).

[75] J. Kramer, E. Redel, R. Thomann, C. Janiak, *Organomettalics*, **27**, 1976, (2008).

[76] T. Sugimoto, M. Kikuta, E. Ishiko, M. Kono, M. Ishikawa, *J. Power Sources*, **183**, 436, (2008).

[77] T. Sugimoto, Y. Atsumi, M. Kikuta, E. Ishiko, M. Kono, M. Ishikawa, *J. Power Sources*, **189**, 802, (2009).

[78] T. Sugimoto, Y. Atsumi, M. Kono, M. Kikuta, E. Ishiko, M. Yamagata, M. Ishikawa, *J. Power Sources*, **195**, 6153, (2010).

[79] A. Guerfi, S. Duchesne, Y. Kobayashi, A. Vijh, K. Zaghib, *J. Power Sources*, **175**, 866, (2008).

[80] H. Matsumoto, H. Sakaebe, K. Tatsumi, M. Kikuta, E. Ishiko, M. Kono, *J. Power Sources*, **160**, 1308, (2006).

[81] H. Sakaebe, H. Matsumoto, K. Tatsumi, *Electrochim. Acta*, **53**, 1048, (2007).

[82] A. Fernicola, F. Croce, B. Scrosati, T. Watanabe, H. Ohno, *J. Power Sources*, **41**, 348, (2007).

[83] S. Seki, Y. Kobayashi, H. Miyashiro, Y. Ohno, A. Usami, Y. Mita, N. Kihira, M. Watanabe, N. Terada, *J. Phys. Chem. B*, **110**, 10228, (2006).

[84] T.E. Sutto, *J. Electrochem. Soc.*, **154**, P101, (2007).

[85] R. Fortunato, L.C. Branco, C.A.M. Afonso, J. Benavente, J.G. Crespo, *J. Membrane Science*, **270**, 42, (2006).

[86] S. Sirisopanaporn, A. Fernicola, B. Scrosati, *J. Power Sources*, **186**, 490, (2009).

[87] C. Ye, W. Liu, Y. Chen, L. Yu, *Chem. Commun.*, 2244, (2001).

[88] F. Zhou, Y. Liang, W. Liu, *Chem. Soc. Rev.*, **38**, 2590, (2009).

[89] X. Q. Liu, F. Zhou, Y. M. Liang and W. M. Liu, Wear, **261**, 1174, (2006).

[90] L. J. Weng, X. Q. Liu, Y. M. Liang and Q. J. Xue, *Tribol. Lett.*, **26**, 11, (2007).

[91] H. Kamimura, T. Chiba, T. Kubo, H. Nanao, I. Minami, S. Mori, *Japanese J. Trib.*, **51**, 675, (2006).

[92] Q. Lu, H. Wang, C. Ye, W.M. Liu, Q. Xue, *Tribol. Inter.*, **37**, 547, (2004).

[93] I. Minami, M. Kita, T. Kubo, H. Nanao, S. Mori, *Tribol. Lett.*, **30**, 215, (2008).

[94] B. Harrison, R. Crerw, M. S. Koncady, D. M. Pai, M. W. Lopatka and P. B. Jones, Proceedings of IMECE 2005, 2005ASME International Mechanical Engineering Congress and Exposition, P405, Nov 511, Orlando, Florida, USA, (2005).

[95] S. Hayashi, R. Ozawa, H. Hamaguchi, *Chem. Lett.*, **32**, 498, (2003).

[96] H. Katayanagi , S. Hayashi , H. Hamaguchi , K. Nishikawa, *Chem. Phys. Lett.*, **392**, 460, (2004).

[97] K. Iwata, H. Okajima, S. Saha, H. Hamaguchi, *Acc. Chem. Res.*, **40**, 1174, (2007).

[98] M. Deetlefs, C. Hardacre, M. Nieuwenhuyzen, A. A. H. Padua, O. Sheppard, A. K. Soper, *J. Phys. Chem. B*, **110**, 12055, (2006).

[99] A. Triolo, A. Mandanici, O. Russina, V. Rodriguez-Mora, M. Cutroni, C. Hardacre, M. Nieuwenhuyzen, H. Bleif, L. Keller, M. A. Ramos, *J. Phys. Chem. B*, **110**, 21357, (2006).

[100] M. Kanakubo, T. Ikeda, T. Aizawa, H. Nanjo, Y. Kameda, Y. Amo, T. Usuki, *Analytical Sciences*, **24**, 1373, (2008).

[101] C. Hardacre, J. D. Holbrey, S. E. Jane McMath, D. T. Bowron, A. K. Soper, *J. Chem. Phys.*, **118**, 273, (2003).

[102] R. W. Berg, M. Deetlefs, K. R. Seddon, I. Shim, J. M. Thompson, *J. Phys. Chem. B*, **109**, 19018, (2005).

[103] R. C. Remsing, J. L. Wildin, A. L. Rapp, G. Moyna, *J. Phys. Chem. B*, **111**, 11619, (2007).

[104] K. Fumino, A. Wulf, R. Ludwig, *Angew. Chem. Int. Ed.*, **47**, 8731, (2008).

[105] A. Wulf, K. Fumino, R. Ludwig, *Angew. Chem. Int. Ed.*, **49**, 449, (2010).

[106] A. Wulf, K. Fumino, R. Ludwig, P. F. Taday, *ChemPhysChem*, **11**, 349, (2010).

[107] A. Noda, K. Hayamizu, M. Watanabe, *J. Phys. Chem. B*, **105**, 4603, (2001).

[108] T. Umecky, M. Kanakubo, Y. Ikushima, *Fluid Phase Equilibria*, **228**, 329, (2005).

[109] M. Kanakubo, K. R. Harris , N. Tsuchihashi, K. Ibuki, M. Uenoc, *Fluid Phase Equilibria*, **261**, 414, (2007).

[110] G. Annat, D. R. MacFarlane, M. Forsyth, *J. Phys. Chem. B*, **111**, 9018, (2007).

[111] M. Kanakubo, K. R. Harris, N. Tsuchihashi, K. Ibuki, M. Ueno, *J. Phys. Chem. B*, **111**, 2062, (2007).

[112] K. R. Harris, M. Kanakubo, N. Tsuchihashi, K. Ibuki, M. Ueno, *J. Phys. Chem. B*, **112**, 9830, (2008).

[113] K. R. Harris, M. Kanakubo, L. A. Woolf, *J. Chem. Eng. Data*, **51**, 1161, (2006).

[114] K. R. Harris, M. Kanakubo, L. A. Woolf, *J. Chem. Eng. Data*, **52**, 1080, (2007).

[115] K. R. Harris, M. Kanakubo, L. A. Woolf, *J. Chem. Eng. Data*, **52**, 2425, (2007).

[116] H. Tokuda, K. Hayamizu, K. Ishii, Md. A. B. H. Susan, M. Watanabe, *J. Phys. Chem. B*, **108**, 16593, (2004).

[117] T. Umecky, M. Kanakubo, Y. Ikushima, *J. Mol. Liq.*, **119**, 77, (2005).

[118] Hu Cang, Jie Li, and M. D. Fayer, *J. Chem. Phys.*, **119**, 13017, (2003).

[119] J. H. Antony, D. Mertens, A. Dölle, P. Wasserscheid, W. R. Carper, *ChemPhysChem*, **4**, 588, (2003).

[120] A. Triolo, V. Arrighi, F. Juranyi, S. Janssen, C.M. Gordon, *J. Chem. Phys.*, **119**, 8549, (2003).

[121] A. Triolo, O. Russina, C. Hardacre, M. Nieuwenhuyzen, M. A. Gonzalez, H. Grimm, *J. Phys. Chem. B*, **109**, 22061, (2005).

[122] Y. Inamuraa, O. Yamamuroa, S. Hayashib, H. Hamaguchi, *Physica B*, **385**, 732, (2006).

[123] C. G. Hanke, S. L. Price, R. M. Lynden-Bell, *Mol. Phy.*, **99**, 801, (2001).

[124] J. H. Antony, D. Mertens, T. Breitenstein, A. Dölle, P. Wasserscheid, W. R. Carper, *Pure Appl. Chem.*, **76**, 255, (2004).

[125] M. G. Del Popolo, R. M. Lynden-Bell, J. Kohanoff, *J. Phys. Chem. B*, **109**, 5895, (2005).

[126] B. L. Bhargava, S. Balasubramanian, *Chem. Phys. Lett.*, **417**, 486, (2006).

[127] M. G. Del Popolo, J. Kohanoff, R. M. Lynden-Bell, C. Pinilla, *Acc. Chem. Res.*, **40**, 1156, (2007).

[128] P. A. Hunt, B. Kirchner,T. Welton, *Chem. Eur. J.*, **12**, 6762, (2006).

[129] P.A. Hunt, I.R. Gould, B. Kirchner, *Aus. J. Chem.*, **60**, 9, (2007).

[130] P. A. Hunt, I. R. Gould, *J. Phys. Chem. A*, **110**, 2269, (2006).

[131] S. Zahn, G. Bruns, J. Thar and B. Kirchner, *Phys. Chem. Chem. Phys.*, **10**, 6921, (2008).

[132] J. Thar, M. Brehm, A.P. Seitsonen, B. Kirchner, *J. Phys. Chem. B*, **113**, 15129, (2009).

[133] S. Zahn, J. Thar, B. Kirchner, *J. Chem. Phys.*, **132**, 124506, (2010).

[134] V. Kempter, B. Kirchner, *J. Mol. Struct.*, **972**, 22, (2010).

[135] B. L. Bhargava, S. Balasubramanian, *J. Chem. Phys.*, **123**, 144505, (2005).

[136] O. Borodin, G. D. Smith, *J. Phys. Chem. B*, **110**, 11481, (2006).

[137] C. Cadena, E. J. Maginn, *J. Phys. Chem. B*, **110**, 18026, (2006).

[138] L. J. A. Siqueira, M. C. C. Ribeiro, *J. Phys. Chem. B*, **111**, 11776, (2007).

[139] Aneesh Chandran, Karthigeyan Prakash, Sanjib Senapati, *Chem. Phys.*, **374**, 46, (2010).

[140] M. S. Kelkar, E. J. Maginn, *J. Phys. Chem. B*, **111**, 4867, (2007).

[141] W. Zhao, F. Leroy, S. Balasubramanian, F. Müller-Plathe, *J. Phys. Chem. B*, **112**, 8129, (2008).

[142] O. Borodin, G. D. Smith, H. Kim, *J. Phys. Chem. B*, **113**, 4771, (2009).

[143] N. Van-Oanh, C. Houriez, B. Rousseau, *Phys. Chem. Chem. Phys.*, **12**, 930, (2010).

[144] M. G. Del Popolo, G. A. Voth, *J. Phys. Chem. B*, **108**, 1744, (2004).

[145] Y. Wang, G. A. Voth, *J. Phys. Chem. B*, **110**, 18601, (2006).

[146] W. Zhao, F. Leroy, B. Heggen, S. Zahn, B. Kirchner, S. Balasubramanian, F. Müller-Plathe, *J. Am. Chem. Soc.*, *131*, 15825, (2009).

[147] S. Komann, J. Thar, B. Kirchner, P. A. Hunt, Tom Welton, *J. Chem. Phys.*, **124**, 174506, (2006).

[148] C. J. Margulis, *Mol. Phys.*, **102**, 829, (2004).

[149] Z. Hu, C. J. Margulis, *PNAS*, **103**, 831, (2006).

[150] J. Habasaki, K. L. Ngai, *J. Chem. Phys.*, **129**, 194501, (2008).

[151] Z. Hu, X. Huang, H. V. R. Annapureddy, C. J. Margulis, *J. Phys. Chem. B*, **112**, 7837, (2008).

[152] T. Ishida, K. Nishikawa, H. Shirota, *J. Phys. Chem. B*, **113**, 9840, (2009).

[153] E. J. Maginn, *J. Phys.: Condens. Matter*, **21**, 373101, (2009).

[154] T, Iimori, T. Iwahashi, H. Ishii, K. Seki, Y. Ouchi, R. Ozawa, H. Hamaguchi, D. Kim, *Chem. Phys. Lett.*, **389**, 321, (2004).

[155] S. Baldelli, *J. Phys. Chem. B*, **109**, 13049, (2005).

[156] S. Rivera-Rubero, S. Baldelli, *J. Phys. Chem. B*, **110**, 4756, (2006).

[157] T, Iimori, T. Iwahashi, K. Kanai, K. Seki, J. Sung, D. Kim, H. Hamaguchi, Y. Ouchi, *J. Phys. Chem. B*, **111**, 4860, (2007).

[158] C. Aliaga, S. Baldelli, *J. Phys. Chem. B*, **111**, 9733, (2007).

[159] C. S. Santos, S. Baldelli, *J. Phys. Chem. B*, **111**, 4715, (2007).

[160] S. Baldelli, *Acc. Chem. Res.*, **41**, 421, (2007).

[161] T. Iwahashi, T. Miyamae, K. Kanai, K. Seki, D. Kim, Y. Ouchi, *J. Phys. Chem. B*, **112**, 11936, (2008).

[162] I. S. Martinez, S. Baldelli, *J. Phys. Chem. C*, **114**, 11564, (2010).

[163] B. D. Fitchett, J. C. Conboy, *J. Phys. Chem. B*, **108**, 20255, (2004).

[164] J. B. Rollins, B. D. Fitchett, J. C. Conboy, *J. Phys. Chem. B*, **111**, 4990, (2007).

[165] C. Aliaga, S. Baldelli, *J. Phys. Chem. C*, **112**, 3064, (2008).

[166] A. J. Carmichael , C. Hardacre, J. D. Holbrey, M. Nieuwenhuyzen, K. R. Seddon, *Mol. Phys.*, **99**, 795, (2001).

[167] E. Sloutskin, B. M. Ocko, L. Tamam, I. Kuzmenko, T. Gog, M. Deutsch, *J. Am. Chem. Soc.*, **127**, 7796, (2005).

[168] E. Sloutskin, R. M. Lynden-Bell, S. Balasubramanian, M. Deutsch, *J. Chem. Phys.*, **125**, 174715, (2006).

[169] M. Mezger, H. Schröder, H. Reichert, S. Schramm, J. S. Okasinski, S. Schröder, V. Honkimäki, M. Deutsch, B.M. Ocko, J. Ralston, M. Rohwerder, M. Stratmann, and H. Dosch, *Science*, **322**, 424, (2008).

[170] M. Mezger, S. Schramm, H. Schröder, H. Reichert, M. Deutsch, E.J. De Souza, J.S. Okasinski, B.M. Ocko, V. Honkimäki, and H. Dosch, *J. Chem. Phys.*, **131**, 094701, (2009).

[171] T. J. Gannon, G. Law, P. R. Watson, *Langmuir*, **15**, 8429, (1999).

[172] G. Law, P. R. Watson, A. J. Carmichael, K. R. Seddon, *Phys. Chem. Chem. Phys.*, **3**, 2879, (2001).

[173] C. S. Santos, S. Baldelli, *Chem. Soc. Rev.*, **39**, 2136, (2010).

[174] V. O. Santos, Jr., M. B. Alves, M. S. Carvalho, P. A. Z. Suarez, J C. Rubim, *J. Phys. Chem. B*, **110**, 20379, (2006).

[175] T. Yan, S. Li, W. Jiang, X. Gao, B. Xiang, G. A. Voth, *J. Phys. Chem. B*, **110**, 1800, (2006).

[176] B. L. Bhargava, S. Balasubramanian, *J. Am. Chem. Soc.*, **128**, 10073, (2006).

[177] R. M. Lynden-Bell, M. G. Del Popolo, T. G. A. Youngs, J. Kohanoff, C. G. Hanke, J. B. Harper, C. C. Pinilla, *Acc. Chem. Res.*, **40**, 1138, (2007).

[178] W. Jiang, T. Yan, Y. Wang, G. A. Voth,*J. Phys. Chem. B*, **112**, 3121, (2008).

[179] W. Jiang, Y. Wang, T. Yan, G. A. Voth,*J. Phys. Chem. C*, **112**, 1132, (2008).

[180] A. S. Pensado, P. Malfreyt, A. A. H. Padua, *J. Phys. Chem. B*, **113**, 14708, (2009).

[181] R. M. Lynden-Bell, J. Kohanoff, M. G. Del Popolo, *Faraday Discuss.*, **129**, 57, (2005).

[182] G. Chevrot, R. Schurhammer, G. Wipff, *Phys. Chem. Chem. Phys.*, **8**, 4166, (2006).

[183] N. Sieffert, G. Wipff, *J. Phys. Chem. B*, **110**, 13076, (2006).

[184] N. Sieffert, G. Wipff, *J. Phys. Chem. B*, **111**, 4951, (2007).

[185] L. Liu, S. Li, Z. Cao, Y. Peng, G. Li, T. Yan, X. Gao, *J. Phys. Chem. C*, **111**, 12161, (2007).

[186] S. Maolin, Z. Fuchun, W. Guozhong, F. Haiping, W. Chunlei, C. Shimou, Z. Yi, H. Jun, *J. Chem. Phys.*, **128**, 134504, (2008).

[187] S. A. Kislenko, I. S. Samoylov, R. H. Amirov, *Phys. Chem. Chem. Phys.*, **11**, 5584, (2009).

[188] S. A. Kislenko, R. H. Amirov, I. S. Samoylov, *Phys. Chem. Chem. Phys.*, **12**, 11245, (2010).

[189] S. Wang, S. Li, Z. Cao, T. Yan, *J. Phys. Chem. C*, **114**, 990, (2010).

[190] C. Pinilla, M. G. Del Popolo, R. M. Lynden-Bell, J. Kohanoff, *J. Phys. Chem. B*, **109**, 17922, (2005).

[191] B. Heggen, W. Zhao, F. Leroy, A. J. Dammers,Florian Muüller-Plathe, *J. Phys. Chem. B*, **114**, 6954, (2010).

[192] M. -P. Allen, D. J. Tildesley, *Computer Simulation of Liquids, Oxford University Press*, (Oxford, England, 1989).

[193] N. Metropolis, A. W. Rosenbluth, M. N. Rosenbluth, A. H. Teller, E. Teller, *J. Chem. Phys.*, **21**, 1087, (1953).

[194] M. E. Tuckerman, B. J. Berne, G. Martyna, *J. Chem. Phys.*, **97**, 1990, (1992).

[195] L. Verlet, *Phys. Rev.*, **159**, 98, (1967).

[196] L. Verlet, *Phys. REv.*, *165*, 201, (1968).

[197] R. W. Hockney, J. W. Eastwood, *Computer simulations using particles*, Adam Hilger, Bristol, (1988).

[198] W. C. Swope, H. C. Anderson, P. H. Berens, K. R. Wilson, *J. Chem. Phys.*, **76**, 637, (1982).

[199] D. J. Evans, W. G. Hoover, B. H. Failor, B. Moran, A. J. C. Ladd, *Phys. Rev. A*, **28**, 1016, (1983).

[200] W. G. Hoover, A. J. C. Ladd, B. Moran, *Phys. Rev. Lett.*, **48**, 1818, (1982).

[201] T. Schneider, E. Stoll, *Phys. Rev. B*, **17**, 1302, (1978).

[202] H. C. Andersen, *J. Chem. Phys.*, **72**, 2384, (1980).

[203] S. Nosé, *Mol. Phys.*, **52**, 255, (1984).

[204] S. Nosé, *J. Chem. Phys.*, **81**, 511, (1984).

[205] W. G. Hoover, *Phys. Rev. A*, **31**, 1695, (1985).

[206] S. Nosé, *Mol. Phys.*, **57**, 187, (1986).

[207] G. J. Martyna, M. L. Klein, M. E. Tuckerman, *J. Chem. Phys.*, **97**, 2635, (1992).

[208] G. J. Martyna, M. E. Tuckerman, D. J. Tobias, M. L. Klein, *Mol. Phys.*, **87**, 1117, (1996).

[209] C. J. Mundy, S. Balasubramanian, K. Bagchi, M. E. Tuckerman, G. J. Martyna, M. L. Klein, *Reviews in Comutational Chemistry*, **14**, 291, (1999).

[210] W.D. Cornell, p. Cieplak, C.I. Bayly, I.R. Gould, K.M. Merz, D.M. Ferguson, D.C. Spellmeyer, T. Fox, J.W. Caldwell, P.A. Kollman, *J. Am. Chem. Soc.*, bf 117, 5179, (1995).

[211] A.D. MacKerell, D. Bashford, M. Bellott, R.L. Dunbrack, J.D. Evanseck, M.J. Field, S. Fischer, J. Gao, H. Guo, S. Ha, D. Joseph-McCarthy, L. Kuchnir, K. Kuczera, F.T.K Lau, C. Mattos S. Michnick, T. Ngo, D.T. Nguyen, B. Prodhom, W.E. Reiher, B. Roux, M. Schlenkrich, J.C. Smith, R. Stote, J. Straub, M. Watanabe, J. Wiorkiewicz-Kuczera, D. Yin, H. Karplus, *J. Phys. Chem. B*, **102**, 3586i, (1998).

[212] W.L. Jorgensen, D.S Maxwell, J. TiradoRives, *J. Am. Chem. Soc.*, **118**, 11225, (1996).

[213] J.N.C. Lopes, J. Deschamps, A.A.H. Padua, *J. Phys. Chem. B*, **108**, 2038, (2004).

[214] J.N.C. Lopes, A.A.H. Padua, *J. Phys. Chem. B*, **108**, 16893, (2004).

[215] J.N.C. Lopes, A.A.H. Padua, *J. Phys. Chem. B*, **110**, 7485, (2006).

[216] J.N.C. Lopes, A.A.H. Padua, *J. Phys. Chem. B*, **110**, 19586, (2006).

[217] J.N.C. Lopes, A.A.H. Padua, K. Shimizu, *J. Phys. Chem. B*, **112**, 5039, (2008).

[218] K. Shimizu, D. Almantariotis, M.F. Costa Gomes, A.A.H. Padua, J.N.C. Lopes, *J. Phys. Chem. B*, **114**, 3592, (2010).

[219] Z. Liu, S. Huang, W. Wang, *J. Phys. Chem. B*, **108**, 12978, (2004).

[220] X. Wu, Z. Liu, S. Huang, W. Wang, *Phy. Chem. Chem. Phys.*, **7**, 2771, (2005).

[221] Z. Liu, X. Wu, W. Wang, *Phy. Chem. Chem. Phys.*, **8**, 1096, (2006).

[222] J. de Andrade, E.S. Böse, H. Stassen, *J. Phys. Chem. B*, **106**, 3546, (2002).

[223] J. de Andrade, E.S. Böse, H. Stassen, *J. Phys. Chem. B*, **106**, 13344, (2002).

[224] T.I. Morrow, E.J. Maginn, *J. Phys. Chem. B*, **107**, 9160, (2003).

[225] B.L. Bhargava, S. Balasubramanian, *J. Chem. Phys.*, **127**, 114510, (2007).

[226] M. Masia, *J. Chem. Phys.*, **128**, 184107, (2008).

[227] S.V. Sambasivarao, O. Acevedo, *J. Chem. Theory Comput*, **5**, 1038, (2009).

[228] O. Borodin, *J. Phys. Chem. B*, **113**, 11463, (2009).

[229] Z. Liu, T. Chen, A. Bell, B. Smit, *J. Phys. Chem. B*, **114**, 4572 (2010).

[230] P.A. Hunt, *Molec. Simulations*, **32**, 1 (2006).

[231] D. Frenkel, B. Smit, *Understanding Molecular Simulations*, (Academic Press, San Diego, 1996).

[232] D. A. McQuarrie, *Statistical Mechanics*, (University Science Books, Sausakito, 2003).

[233] B. J. Berne, R. Pecora, *Dynamic Light Scattering : With Applications to Chemistry, Biology, and Physics*, (John Wiley & Sons, Inc., New York, 1976).

[234] J. -P. Hansen, I. R. McDonald, *Theory of Simple Liquids*, (Academic Press, New York, 1986).

[235] S. J. Plimpton, *J. Comp. Phys*, **117**, 1, (1995).

[236] J. Hutter, J, P. Ballone, M. Bernasconi, P. Focher, E. Fois, S. Goedecker, D. Marx, M. Parrinello, M.E. Tuckerman, CPMD Version 3.11.1, Max Planck Institut fuer Festkoerperforschung, Stuttgart, and IBM Zurich Research Laboratory, 1990-. Version 3.13.2.

Chapter 2

Correlation between Dynamic Heterogeneity and Local Structure in a Room Temperature Ionic Liquid: A Molecular Dynamics Study of [bmim][PF_6]

2.1 Introduction

The presence of both organic and inorganic components in room temperature ionic liquids (RTIL) make them uniquely interesting, not only in terms of the variety they exhibit in microscopic structure, but also in their dynamics [1, 2]. Although their intermolecular structure is primarily determined by the strong electrostatic interactions (characteristic of molten salts), van der Waals forces between the alkyl groups of the cations too influence near neighbor, and possibly, the intermediate range structure in these liquids [3–5]. A subtler aspect of the ordering in these liquids is the hydrogen bonding between the acidic hydrogen of the imidazolium cation and sites of the anion [6–11]. While many of these aspects have been well explored using both experiments and computations, specific relationships between intermolecular structure and dynamics remain not as well studied.

A large number of experiments and simulations have been carried out to study the dynamics of ionic liquids (IL) over the last decade. Triolo and co-workers have employed various neutron scattering techniques (elastic, inelastic, and quasielastic) [12, 13], as well as neutron spin echo method [14] to investigate the relaxation processes in a set of ILs. Weingärtner and co-workers have used microwave dielectric relaxation spectroscopy to study the picosecond dynamics of RTILs based on pyrolidinium, pyridinium, tetraalkylammonium, and triethylsulfonium cations and bis(triflouromethyl sulfonyl) anions [15–17]. Using dielectric relaxation and ultrafast optical Kerr effect spectroscopy, Turton *et al* [18] observed multiple relaxations in an IL. They interpreted the α-relaxation to arise possibly from librations of the cations and a slower, sub-α relaxation to arise from relaxation of stacked cation rings [19]. Ludwig *et al* have carried out FTIR and NMR experiments as well as density functional theory (DFT) based calculations on [C_2mim][NTf_2] ionic liquid to study the dynamics of cation-anion hydrogen bond [7, 20]. Moreover, they have also studied the validity of Stokes-Einstein (SE) and Stokes-Einstein-Debye (SED) relations using molecular dynamics (MD) simulations [21] and found that both SE and SED relations do not hold good for [C_2mim][NTf_2]. *Ab initio* calculations have also been employed to study the relationship between ion pairs and the dynamics in a set of ILs ([bmim] cation and [Cl], [BF_4], [NTf_2] anions) [22, 23]. Many other works have explored both single particle and collective dynamics of ILs with MD simulations [24–27]. Ion pairs, despite being mobile, do not contribute to the total electrical conductivity of the system due to their charge neutrality. Using MD simulations, Zhao *et al* [28] had recently examined their nature, mobility and lifetime in liquid [bmim][PF_6]. Kim *et al* have shown that the origin of the commonly seen α-relaxation in the dynamics of ILs is the large angle jump of cations rather than rotational diffusion [29], although both ion translations and reorientations contribute to dielectric relaxation.

In the current work, many aspects of the complex dynamics exhibited by ILs have been explored. As a prototype, the IL [bmim][PF_6]has been studied, for which a reasonably good potential model [30] is available. The model has been shown to reproduce many structural [30, 31] and dynamical properties [28, 30, 32] rather well when compared to experimental data. In the present work, both single particle and collective dynamical quantities have been calculated. The dynamical heterogeneity exhibited by this ionic liquid has also been examined and an attempt has been made to study its structural underpinnings.

2.2 Details of Simulation

Equilibrium classical molecular dynamics simulations have been carried out on a system of 256 pairs (8,192 atoms) of [bmim][PF_6] ionic liquid at different temperatures (250 K, 280 K, 300 K, 340 K, 400 K, 450 K) to characterize its dynamics and structural relaxation processes, using the LAMMPS program [33]. The force field parameters for the simulations were obtained from the all-atom model developed by Bhargava*et al* [30]. The model is a fully flexible one with reduced charges on the ions (+0.8 e on the cation and -0.8 e on the anion); Polarization effects are not included in this model. A cutoff distance of 13 Å has been applied in calculating the non-bonded interactions. At each temperature, the system was equilibrated under NPT conditions (at a pressure of 1 atmosphere) for around 1-2 ns, until the equilibrium density was attained. Thereafter, NVT simulations were carried out for durations ranging from 5 to 30 ns depending on the temperature. Samples at lower temperatures were obtained by slow cooling of those at the immediate higher temperature.

The length of analysis trajectory is about 10 ns. Three dimensional periodic boundary conditions were employed and the equations of motion were integrated with a time step of 0.5 fs using the velocity Verlet algorithm. Coulombic interactions were treated using the particle-particle particle-mesh(PPPM) [34] method with an accuracy of 1×10^{-6}. Long range corrections to the potential energy and pressure were applied.

At each of these temperatures, five different simulations were carried out each starting from a configuration synthesized to be independent of others to ensure adequate sampling. The box lengths were 43.88 Å, 44.21 Å, 44.39 Å, 44.85 Å, 45.53 Å, and 46.12 Å at the temperatures 250 K, 280 K, 300 K, 340 K, 400 K and 450 K respectively. The coordinates of each atom were stored at every 0.5 ps for the structural relaxation analysis (mean square displacement (MSD), intermediate scattering function (ISF), electrical conductivity, heterogeneity) and the velocities were dumped at a time interval of 25 fs for studies on dynamics (velocity autocorrelations functions (VACF) and vibrational density of states (VDOS)). All these quantities were averaged over the above mentioned five independent trajectories.

The numbering scheme used for the atoms in the cation is given in Figure 2.1 to aid the discussion.

2.3 Results and Discussion

2.3.1 Diffusion

Figure 2.2 shows the time variation of MSDs for the centers of cations and anions as a function of temperature in logarithmic scale (log-log), as in earlier studies [35–37].

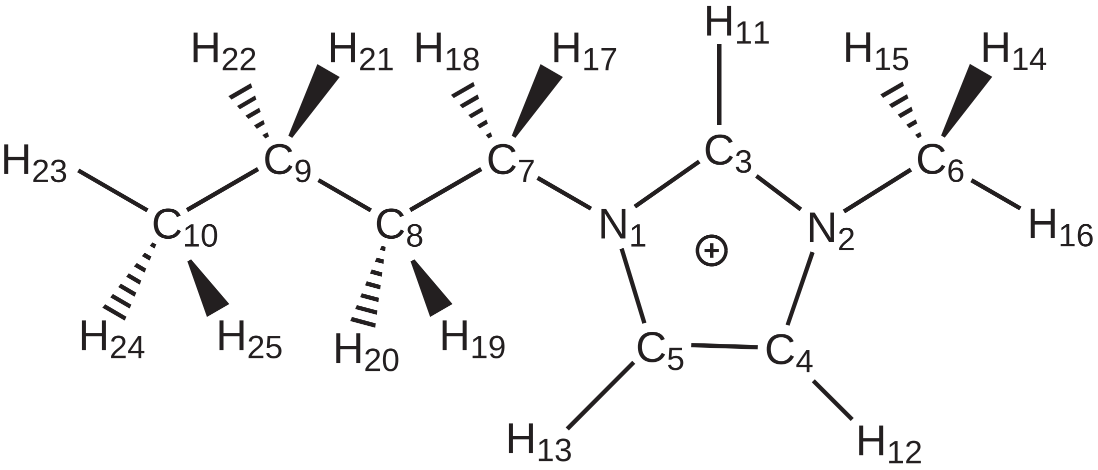

Figure 2.1: Numbering scheme followed in $[\text{bmim}]^+$

Thus, the time dependence of MSD can be written as,

$$\langle |r_i^{(c)}(t) - r_i^{(c)}(0)|^2 \rangle = \Delta r^2 \propto t^\delta \tag{2.1}$$

where the quantity within the angular brackets denotes the ensemble-averaged MSD of an individual ion and $r_i^{(c)}(t)$ is the location of the center of ion i at time t. In this study, the assumed center for cation was the geometric center of the imidazolium ring and that for the anion was its center of symmetry (phosphorus atom).

δ characterizes the behaviour of ionic motion and can be deduced from the following relation,

$$\delta = \lim_{t\to\infty} \frac{d(log(\Delta r^2))}{d(log(t))} \tag{2.2}$$

The MSDs of both the ions showed three regimes in the log-log plot. At short times, the ionic motion was ballistic with the $MSD \propto t^2$ (i.e., $\delta = 2$). At longer times, when the ions escaped from the local neighbour cage, the motion was diffusive with $MSD \propto t$ ($\delta = 1$). At intermediate times, a plateau was observed indicating the sub-diffusive regime, which was similar to that seen in supercooled

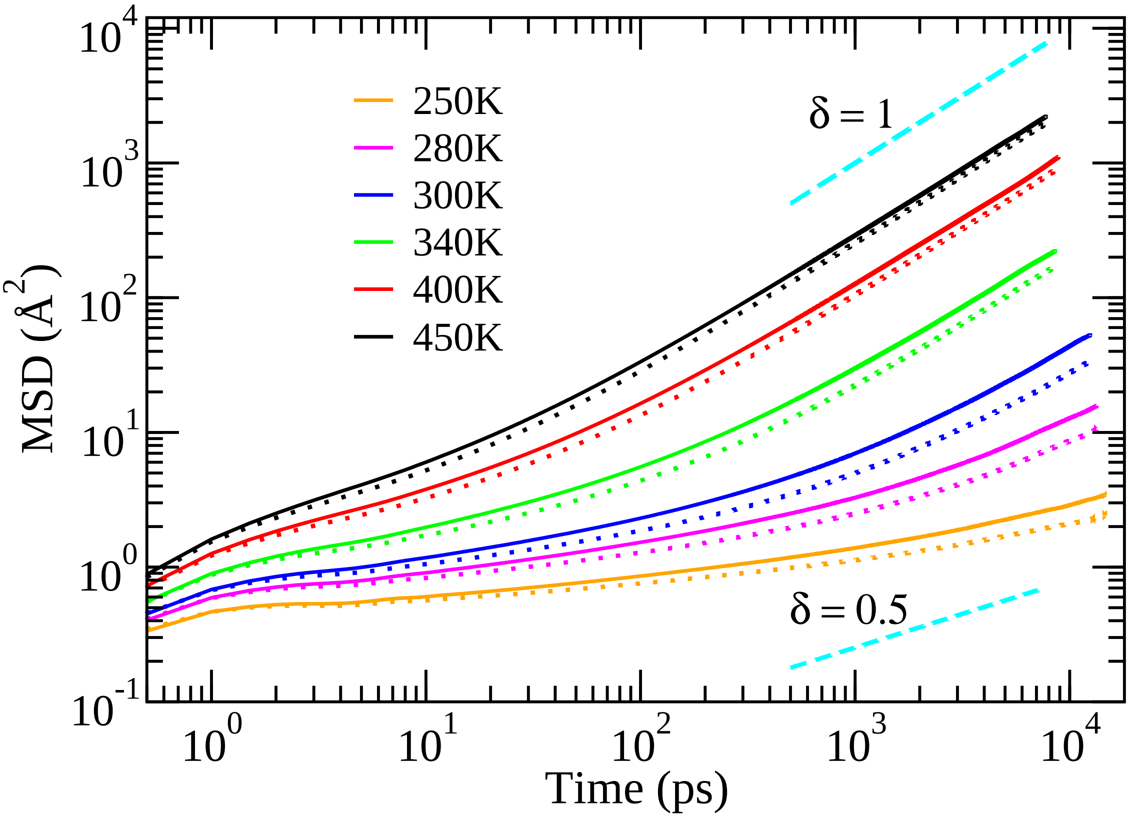

Figure 2.2: Mean squared displacement of ions at all the temperatures. Bold lines are for cations and the dotted ones are for anions. The dashed line is for reference.

liquids ($\delta < 1$) [36, 38]. The duration of this sub-diffusive regime varied with temperature as can be seen from Figure 2.2. The width of the plateau diminished as temperature increased. The δ values for cation and anion at all temperatures are listed in Table 2.1.

Temperature (K)	δ (cation)	δ (anion)
250	0.35	0.29
280	0.64	0.59
300	0.84	0.79
340	0.93	0.94
400	0.98	0.99
450	0.99	0.99

Table 2.1: δ (MSD exponent) values obtained from Eq.2.2

For temperatures $\geq$ 300 K, the system was diffusive in the time scales observed and structural relaxation can be studied (to be discussed later). Careful examination of the MSDs revealed that as temperature increased, the dynamics of cations and anions became more or less similar. This is presumed to be due to the decrease of dynamical heterogeneity in the system (see later) with increase in temperature.

The self diffusion coefficients of ions were calculated from the MSDs using the Einstein equation [39] as,

$$D_s = \frac{1}{6} \lim_{t \to \infty} \frac{d}{dt} \langle \sum_{i=1}^{N} |r_i^{(c)}(t) - r_i^{(c)}(0)|^2 \rangle \tag{2.3}$$

The calculated values for the cation and anion are compared against experimental values in Table 2.2. These values agree with earlier data. As has been noted by others, the [bmim] cation did diffuse faster than the anion despite its larger size and complex shape.

Temperature (K)	D_s^{cation} (10^{-12} m^2/s)	D_s^{anion} (10^{-12} m^2/s)
250	0.19	0.12
280	1.46	0.91
300	6.63 (6.8)	4.17 (4.0)
340	41.10	31.27
400	218.34 (209.2)	173.96 (178.6)
450	475.88 (447.3)	428.47 (401.3)

Table 2.2: Diffusion coefficients of ions. Experimental values [40] known at a few temperatures are provided in parentheses.

There exist many hypotheses explaining this difference in diffusion coefficients, such as ; (i) the anions being present in a deeper potential well than the cations [41] or (ii) the less hindered motion of cations along the direction of carbon-acidic hydrogen bond (i.e., C_3-H_{11} bond shown in Figure 2.1) [24,42]. In order to examine this aspect further, the activation energies for self-diffusion of the ions have been obtained from the dependence of D_s on temperature using an Arrhenius fit, shown in Figure 2.3. (Data for temperatures higher than 300 K were considered for the fit). The fit

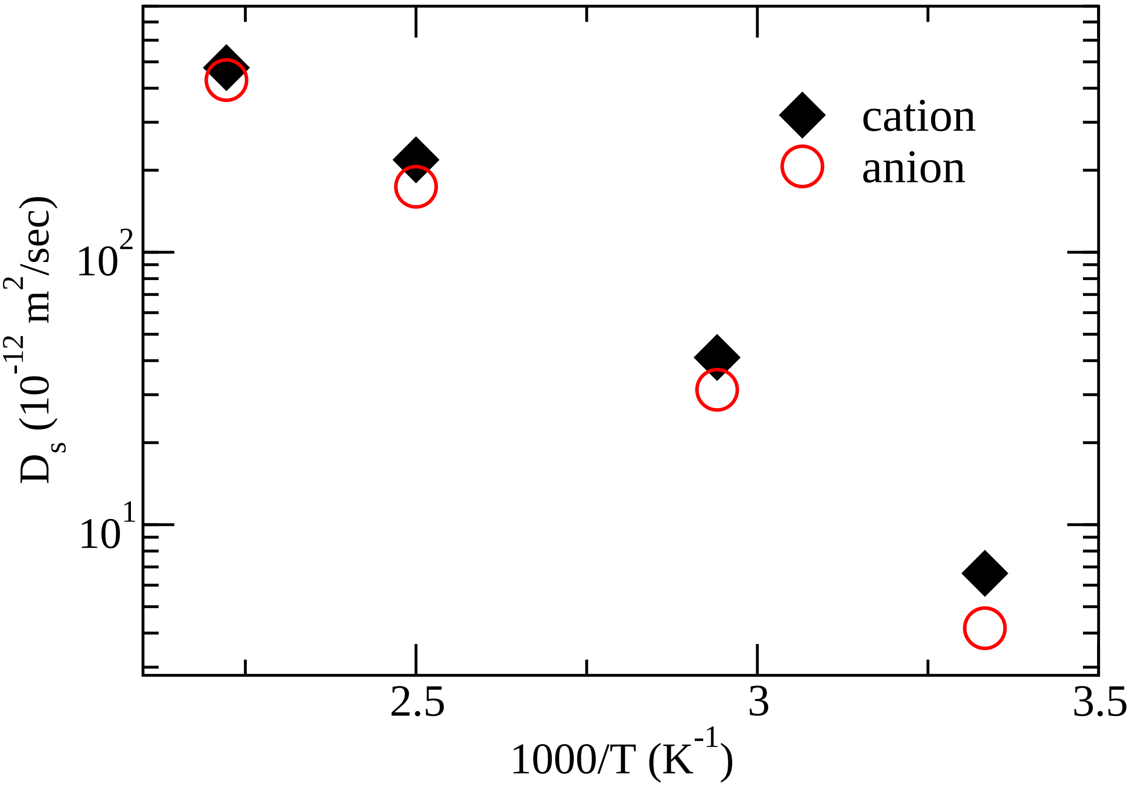

Figure 2.3: Self diffusion coefficients of ions against inverse of temperature.

is rather good, consistent with earlier work of Maginn *et al* for pyridinium based ILs [35] and of Hamaguchi *et al* for [bmim][Cl] [43].

The calculated activation energy of diffusion for the cation and anion are 32.1 kJ/mol and 34.5 kJ/mol respectively. Recently, Zhao *et al* have obtained very similar activation energies for diffusion of the cation (34.4 kJ/mol) and of the anion (36.1 kJ/mol) by assuming an Arrhenius fit [28]. The faster diffusion of cations is consistent with its lower activation energy.

2.3.2 Electrical Conductivity

The electrical conductivity has been calculated from both the Nernst-Einstein equation and from the slope of the collective MSD using an Einstein relation. The

Nernst-Einstein equation is given by [44],

$$\sigma_{\mathrm{NE}} = \frac{Ne^2}{VK_BT}(Z_-^2 D_- + Z_+^2 D_+) \tag{2.4}$$

where N denotes the number of ion pairs, e is the elementary electronic charge, V is the volume of the system, k_B is Boltzmann constant, T is temperature in Kelvin, and Z_- (Z_+) is the formal charge on the anion (cation). σ_{NE} is the upper limit for the actual conductivity as it does not include cross correlation terms. It assumes that the diffusion of individual species contributes entirely to the total electrical conductivity of the system. Recently, Zhao *et al* have studied this quantity and the effect of ion pairing in liquid [bmim][PF_6] [28].

To calculate the true electrical conductivity of the system, one should consider the collective counterpart of the MSD and the corresponding Einstein equation [45, 46],

$$\sigma = \lim_{t\to\infty} \frac{e^2}{6tVK_BT} \langle \sum_{i=1}^{N} \sum_{j=1}^{N} Z_i Z_j * ([r_i^{(c)}(t) - r_i^{(c)}(0)].[r_j^{(c)}(t) - r_j^{(c)}(0)]) \rangle \tag{2.5}$$

The ratio $\sigma/\sigma_{\mathrm{NE}}$ is the percentage of ions which contribute to ionic conductivity. Table 2.3 shows the calculated values of σ, σ_{NE} and $\sigma/\sigma_{\mathrm{NE}}$ at different temperatures and these agreed well with experimental data [47]. The calculated values are marginally lower than the experimental values, which is due to the fractional charges on the ions used in the adopted model (and thus in Equation 2.5). Although both σ and σ_{NE} increased with increase in temperature, the ratio $\sigma/\sigma_{\mathrm{NE}}$ seemed to be independent of it. This behaviour has been observed previously by Tokuda *et al* for a series of ILs and the $\sigma/\sigma_{\mathrm{NE}}$ ratio reported by them was also in the range of 0.6-0.7, similar to the current results [48]. These results imply that there is correlated motion of ions in ILs.

Temperature (K)	σ (S/m)	σ_{NE} (S/m)	$\sigma/\sigma_{\mathrm{NE}}$
300	0.08 (0.144)	0.13	0.64
340	0.50 (0.863 at 345 K)	0.72	0.69
400	2.10	3.17	0.66
450	3.80	6.25	0.61

Table 2.3: Electrical conductivity (σ) calculated using Eq.2.5 and the Nernst-Einstein estimate (σ_{NE}) from Eq.2.4. Experimental values at a few temperatures [47] are given within brackets.

2.3.3 Dynamical Heterogeneity

The dynamical heterogeneity in a system can be studied through the non-Gaussian parameter, defined as,

$$\alpha(t) = \frac{3\langle|\Delta r(t)|^4\rangle}{5\langle|\Delta r(t)|^2\rangle^2} - 1 \tag{2.6}$$

where Δr(t) is the displacement of the ion at time t with respect to its position at time 0. For dynamically homogeneous liquids, α is zero.

Supercooled liquids show a deviation from the normal Gaussian behaviour of the self part of the van Hove correlation function (G_s(r,t)), which is associated with dynamical heterogeneities [38, 49, 50]. Del Popolo and Voth demonstrated this kind of behaviour for the ionic liquid 1-*n*-ethyl-3-methylimidazolium nitrate ([emim][NO_3]) [37]. Margulis and co-workers examined the differential dynamics of cations in liquid [bmim][PF_6] [51, 52] and correlated the same to the existence of regions of IL possessing varied relaxation times. Although on macroscopic time scales the ionic liquid is homogeneous (i.e., there is no difference in the dynamical behaviour of any two regions, whatever be their length scale), in the time scale accessible to simulations (few nanoseconds), one could observe significant differences in the dynamics of different regions in the ionic liquid.

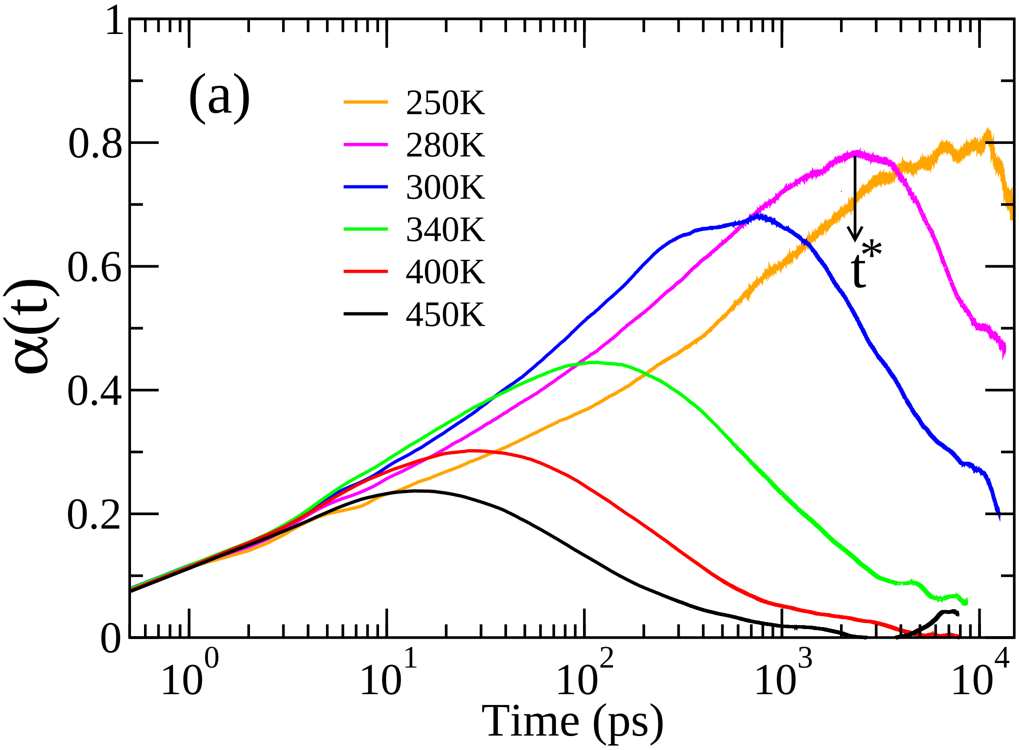

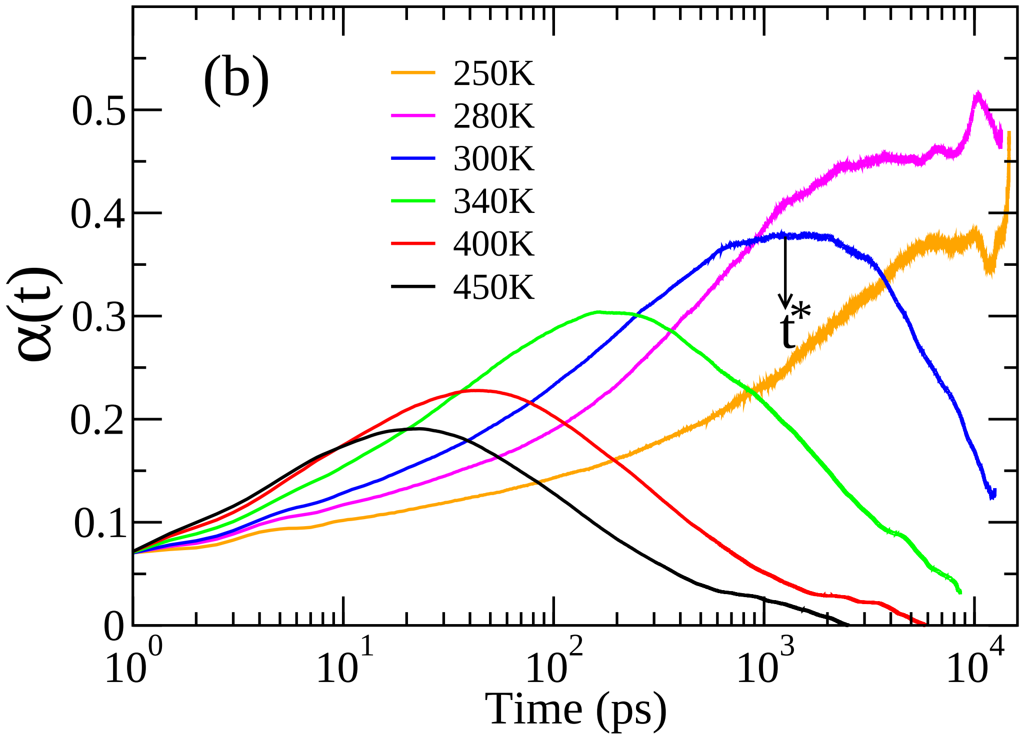

Figure 2.4: Variation of the non-Gaussian parameter (α(t)) with temperature. (a) Cation (b) Anion

Figures 2.4(a) and (b) show the variation of the non-Gaussian parameter with temperature for the cation and anion respectively. At all temperatures, the peak height for the cation is larger than that for the anion, specifically so at low temperatures. In addition, the profiles for the anion are somewhat flatter, indicating that the cations have a higher degree of heterogeneity in their dynamics than the anions.

$\alpha(t)$ was zero during the short time ballistic motion of ions and it reaches a maximum at a time marked with an arrow (t^*) in the intermediate sub-diffusive regime. It once again reaches a value of zero in the long time diffusive regime. The peak height and t^* decrease with increasing temperature for both the ions. At high temperatures, the cation and the anion have nearly the same heterogeneity profiles. Spatially resolved profiles of ion dynamics is provided later in this chapter.

2.3.4 Incoherent Intermediate Scattering Function

The temporal Fourier transform of the self-part of van Hove function [53] provides information on the nature of relaxation of density correlations at specific wave vectors (or, conversely length scales). The function is known as the incoherent (self) intermediate scattering function (F_s(K,t)) and is given by [54],

$$F_s(K,t) = \frac{1}{N}\langle\frac{\sin(K|\mathbf{r}_i^{(c)}(t+t_0) - \mathbf{r}_i^{(c)}(t_0)|)}{K|\mathbf{r}_i^{(c)}(t+t_0) - \mathbf{r}_i^{(c)}(t_0)|}\rangle \tag{2.7}$$

Here, N is the number of ion pairs, K is the reciprocal lattice vector, and $\mathbf{r}_i^{(c)}(t)$ is the position of the ion center at time t. This correlation function exhibits two dynamical regimes in supercooled liquids and in standard glass formers. Similar dynamics has also been reported to be present in ILs recently [12, 25, 55]. The correlation function bears a fast relaxation process at shorter time scale (β-relaxation), immediately followed by the plateau associated with caging. At longer time scales, the ions escape the cage formed by their neighbours (α-relaxation).

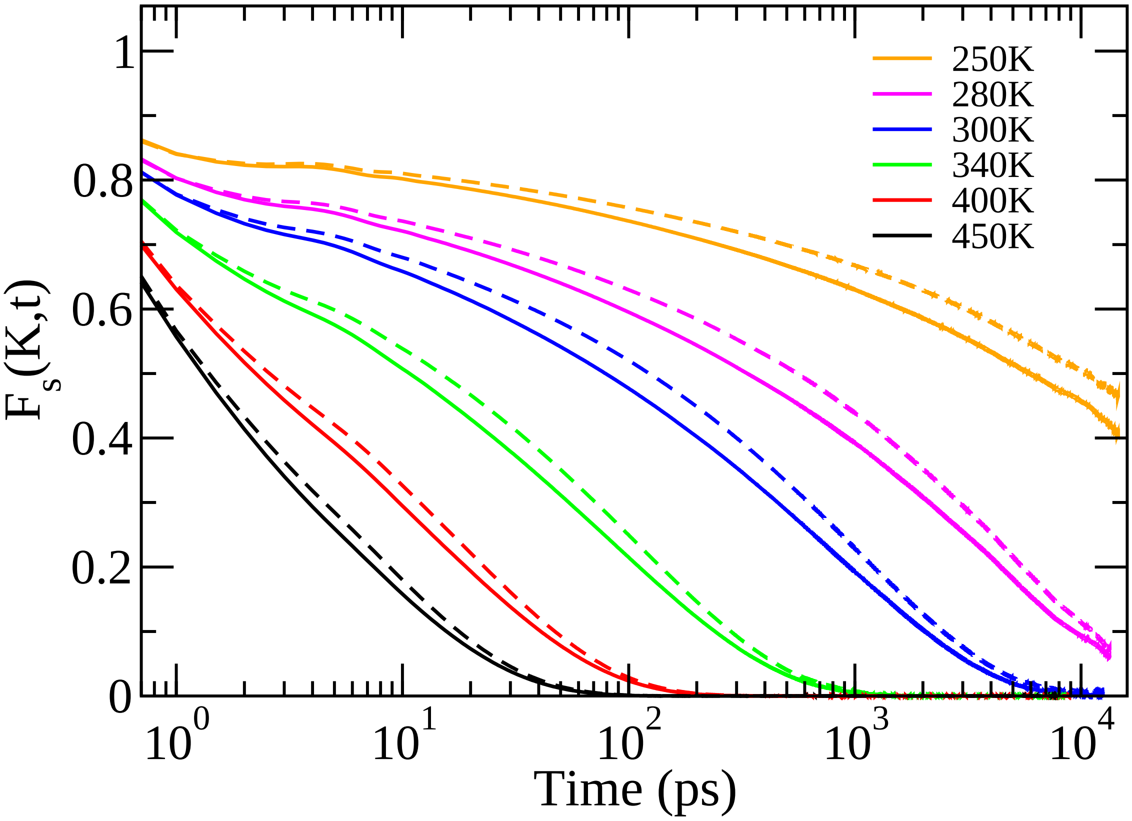

Figure 2.5: Relaxation of F_s(K,t) with time (log scale) for all temperatures at K=1.5 Å^{-1}. Solids and dotted lines are for cations and anions respectively.

Figure 2.5 shows the decay of F_s(K,t) curves with time for the cation and anion over the temperature range, at a wave vector of 1.5 Å^{-1}. As shown earlier, the structure factor of [bmim][PF_6] exhibits a sharp peak at this value of the wave vector [31, 56]. Through an analysis of partial structure factors, this feature was shown to be contributed by anion-anion, tail-tail and tail-cation correlations [31]. It can be inferred directly from Figure 2.5 that the structural relaxation of the cation occurs faster than that of the anion at all temperatures, consistent with diffusion data. F_s(K,t) have been fitted to a modified Kohlrausch-Williams-Watts (KWW) function to obtain the time scales associated with β (τ_β) and α relaxations (τ_α). Its form is [12],

$$F_s(K,t) = Aexp(-t/\tau_\beta) + (1-A)exp(-(t/\tau_\alpha)^\beta) \tag{2.8}$$

where A and (1-A) are the amplitudes of the β and α relaxations respectively. β is the stretching parameter of the α-relaxation. The model represented by Eq. 2.8 takes into account two processes. The β-relaxation process has a purely exponential form, whereas the α-relaxation has a stretched exponential form with the stretching parameter β. Values of $\beta < 1$ indicate a distribution of relaxation times as seen for both the ions in this IL. The actual relaxation time ($\langle\tau_\alpha\rangle$) for the slow relaxation part was obtained by taking the time integral of the stretched exponential term. It is defined as [12,45],

$$\langle\tau_\alpha\rangle = \frac{\tau_\alpha}{\beta}\,\Gamma\,(\frac{1}{\beta}) \tag{2.9}$$

In Figure 2.6, $\langle\tau_\alpha\rangle$ and τ_β as a function of temperature are plotted in semi-log scale. As expected, both the relaxation times decrease with increasing temperature indicating a faster structural relaxation at high temperatures. $\langle\tau_\alpha\rangle$, i.e. the relaxation time of the slower process decreases significantly with increase in temperature, whereas τ_β seems not to be much sensitive to temperature. A closer inspection revealed that τ_β of the anion was marginally lower compared to that of the cation, whereas $\langle\tau_\alpha\rangle$ for cations were lower than those for the anions. This observation suggests that at shorter time scales, when ions move in their respective local energy basins, the anion relaxes marginally faster than the cation. However at longer time scales, the cation relaxes faster than the anion, due possibly to its flexibility which results in a relatively smaller barrier.

The temperature dependence of these relaxation times were fitted to an Arrhenius expression yielding activation energies of 38.7 kJ/mol and 10.8 kJ/mol for the α and β relaxation regimes respectively. The value for the former is only slightly

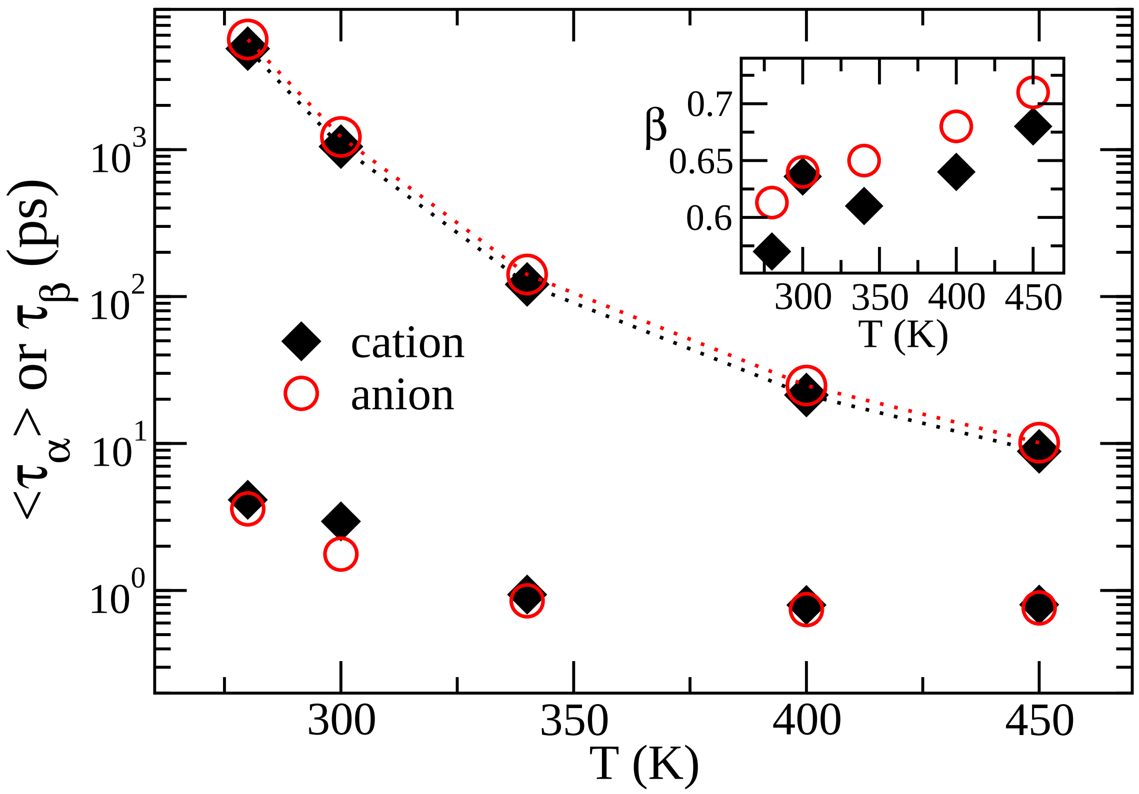

Figure 2.6: $\langle\tau_\alpha\rangle$ and τ_β obtained from F$_s$(K,t) for cations and anions as a function of temperature. At each temperature, the higher and lower values denote $\langle\tau_\alpha\rangle$ and τ_β respectively. Inset shows the variation of the KWW stretching parameter β of the α-relaxation process with temperature. Dotted lines are drawn to guide the eye.

larger than the barriers calculated for ion diffusion discussed earlier. The inset in Figure 2.6 shows the variation of the stretching parameter (β) for the α-relaxation process of cations and anions. For both the cationic and anionic relaxation processes, β increased with increase in temperature. Again, the values for anions were slightly larger than those for cations over the entire temperature range. The data indicated that the dynamics of cations involves a wider distribution of relaxation times than those for anions.

To complete the study of decay of the incoherent intermediate scattering function, the dependence of the relaxation processes on the wave vector (or, in turn the real space correlation length) has also been investigated. The relaxation at various wave vectors relevant to the system size (the minimum being 2π over the box length), at a temperature of 400 K is shown in Figure 2.7. The results match qualitatively those seen in Figure 2.5. The relaxation curves were fitted according to Equation 2.8. Figure 2.8 shows the wave vector dependence of $\langle\tau_\alpha\rangle$ and τ_β.

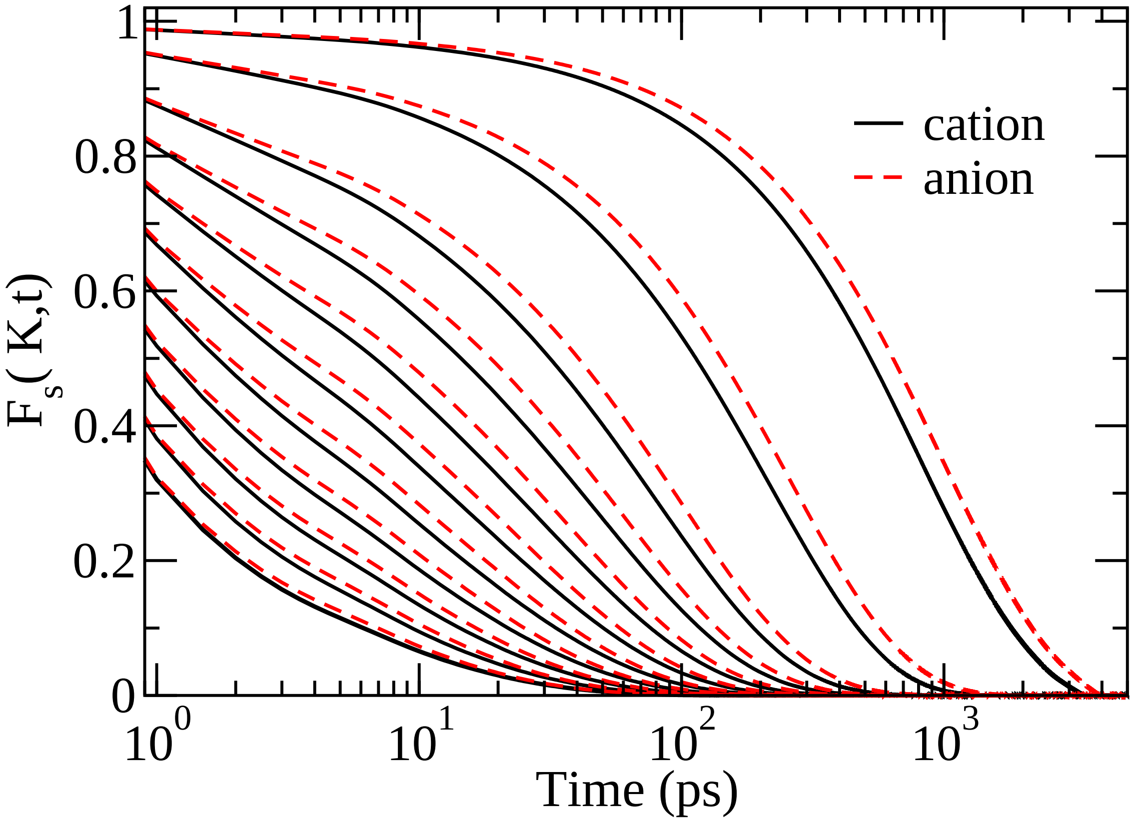

Figure 2.7: Relaxation of F_s(K,t) with time (log scale) at 400 K for the following wave vectors: K (in Å^{-1}) = 0.25, 0.5, 0.8, 1.0, 1.2, 1.4, 1.6, 1.8, 2.0, 2.2, and 2.4 in the order of top to bottom.

With increasing wave vectors, both the relaxation times decrease. τ_β exhibited a much weaker dependence on K than $\langle\tau_\alpha\rangle$. The inset of Figure 2.8 shows the dependence of the stretching parameter (β) on K. As expected, for small wave vectors, i.e., for large values of real space distance, the motion of ions became diffusive and the stretching parameter approaches unity.

Triolo *et al* had studied the incoherent structural relaxation dynamics in liquid [bmim][PF_6] through quasielastic neutron scattering (QENS) experiments [12]. Their technique mainly explored the relaxation of hydrogen atoms of the cation and

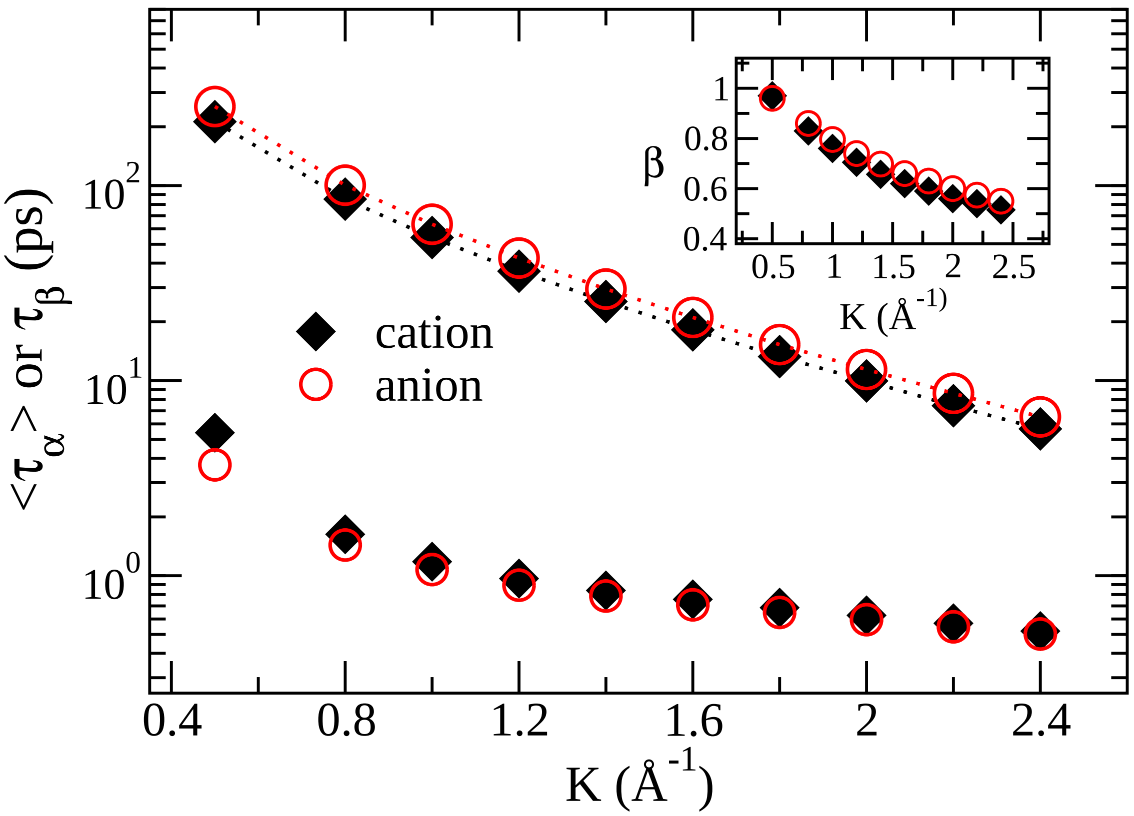

Figure 2.8: $\langle\tau_\alpha\rangle$ and τ_β obtained from F$_s$(K,t) for cations and anions as a function of wave vector, K. The upper curves in the graph represent $\langle\tau_\alpha\rangle$ and the lower ones represent τ_β. Inset shows the variation of the KWW stretching parameter β of the α-relaxation process with wave vector. Dotted lines are guide to the eye.

hence they inferred that the cation relaxation follows the same path as that of the hydrogen atoms. They had observed two kinds of relaxation behaviour for hydrogen atoms, similar to the findings for the cation and the anion in the current study. The simulation results were validated by comparing the calculated incoherent intermediate scattering function for hydrogen atoms to the experimental data of Triolo *et al* [12] at a wave vector of 2.0 Å^{-1} at two temperatures – 250 K and 300 K. Figure 2.9 shows the same. The agreement with experiments is indeed quite good, illustrating the goodness of the potential model used and the protocols employed in the simulations.

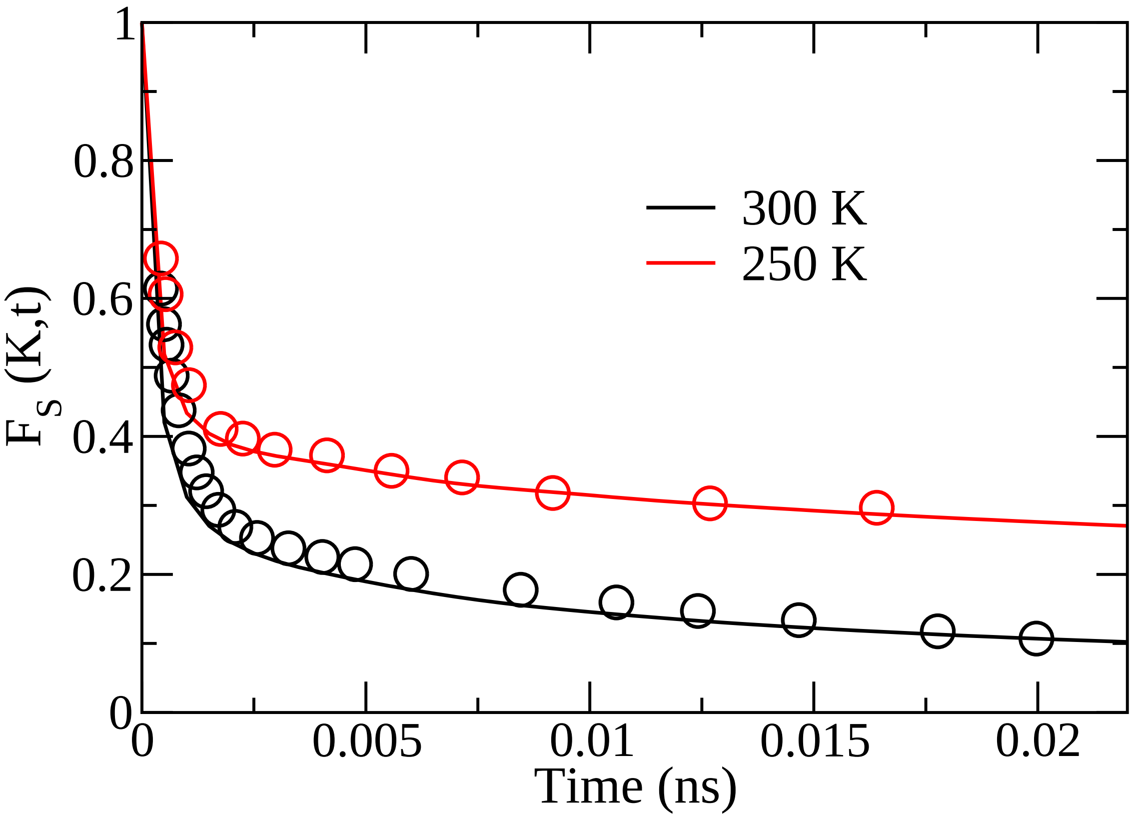

Figure 2.9: Comparison of the relaxation of the incoherent intermediate scattering function of hydrogen atoms obtained from simulations to experiment for a wave vector value of 2.0 Å^{-1} at 250 K and 300 K. Straight lines are simulation data and symbols are from experiment [12].

2.3.5 Coherent Intermediate Scattering Function

While F$_s$(K,t) describes the individual motion of ions, the coherent intermediate scattering function F(K,t) reflects the collective behaviour of the system.

$$F(K,t) = \langle \sum_{i=1}^{N} \sum_{j=1}^{N} \frac{\sin(|K||r_i^{(c)}(t+t_0) - r_j^{(c)}(t_0)|)}{|K||r_i^{(c)}(t+t_0) - r_j^{(c)}(t_0)|} \rangle \tag{2.10}$$

Figure 2.10 shows the relaxation of F(K,t) with wave vectors at 400 K.

The trend is similar to that seen in the case of F$_s$(K,t) (Figure 2.7), with two relaxation processes. The close similarity between these two functions suggests a strong coupling between the individual ionic motion and the collective modes of the liquid.

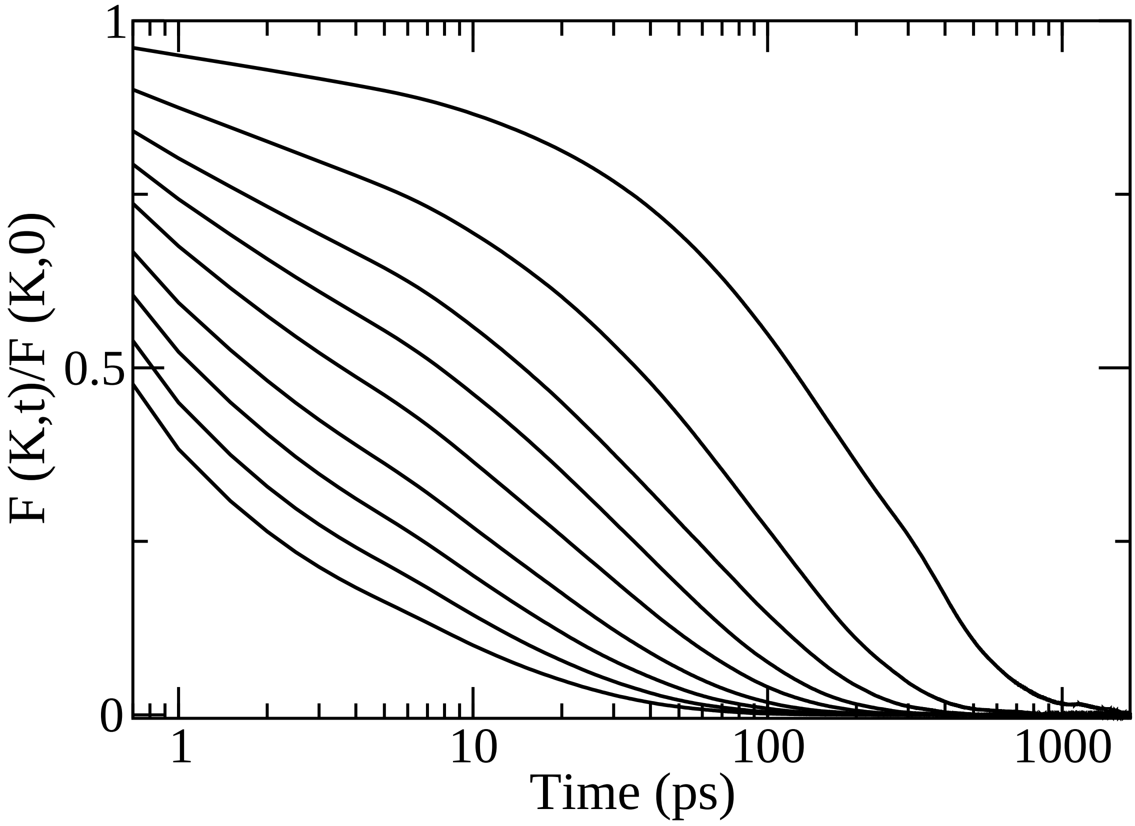

Figure 2.10: Normalized F(K,t) Vs time (log scale) at 400 K for the following wave vectors: K (in Å^{-1}) = 0.5, 0.8, 1.0, 1.2, 1.4, 1.6, 1.8, 2.0, 2.2, and 2.4 in the order of top to bottom.

2.3.6 Velocity Auto Correlation Functions and Vibrational Density of States

The single particle dynamics of the IL has also been studied through the velocity auto correlation functions (VACF) and its Fourier transform, the vibrational density of states (VDOS) of the centers of mass of cations and anions. Figure 2.11 shows the VDOS for cations and anions in the low frequency region at temperatures 300 K and 450 K.

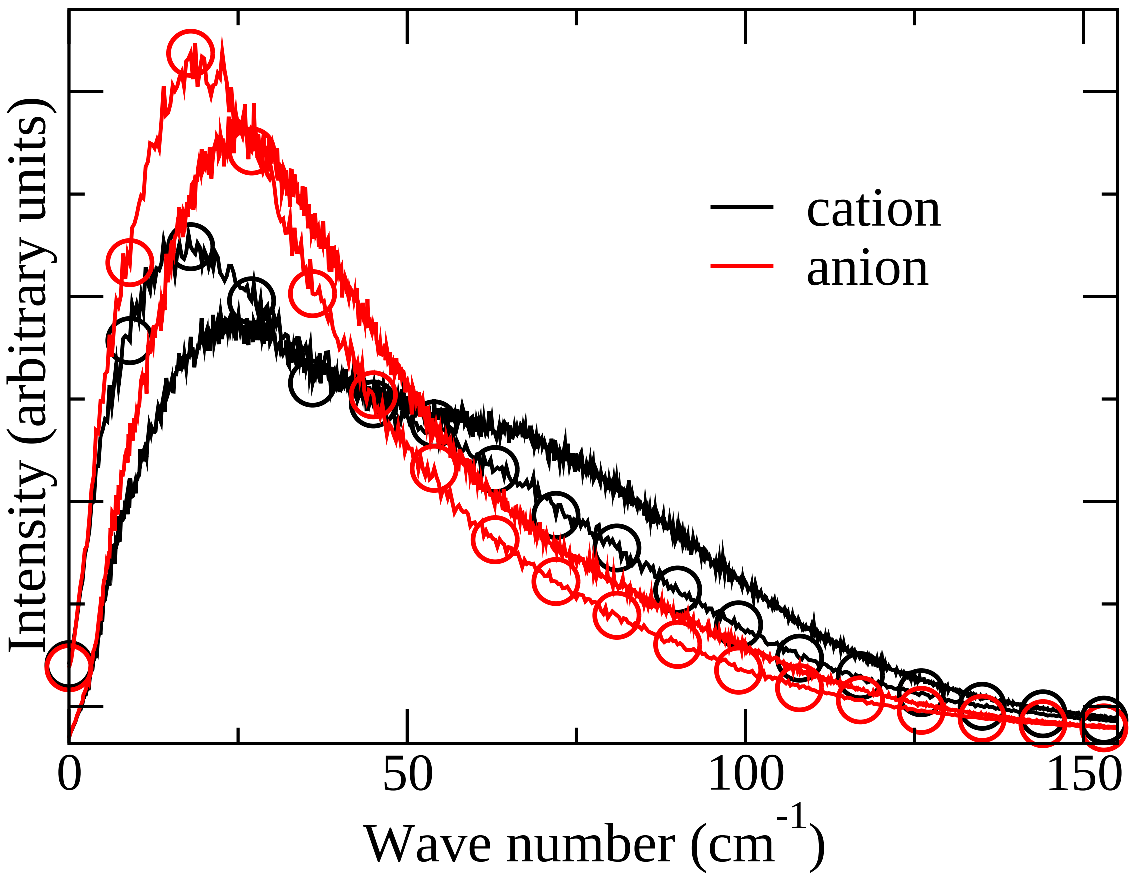

Figure 2.11: Vibrational density of states for the cation and the anion center of mass at 300 K and 450 K. The 300 K data are shown with solid lines and 450 K data are represented by solid lines with circles.

Ishida and co-workers have recently studied the effect of atom substitution in ILs containing anions of the kind [XF_6] using MD simulations. The VDOS spectra obtained from the current simulations are in excellent agreement with theirs [57]. Giraud *et al* could fit the experimental optical Kerr effect (OKE) spectra obtained for a set of ILs to three bands located around 30 cm^{-1}, 65 cm^{-1} and 100 cm^{-1} at 300 K [58]. Urahata and Ribeiro characterized the single particle dynamics of ILs with an united atom model, and obtained two broad bands for [bmim][PF_6] at around 20 cm^{-1} and 80 cm^{-1} [24]. This region of the spectrum results from intermolecular modes and is a good signature of near neighbour arrangement around a given ion type [59,60]. Ludwig *et al* have studied the intermolecular modes using a variety of approaches, including Terahertz spectroscopy, infra-red, and Raman experiments as well as through quantum chemical calculations of ion clusters [59, 60]. For $N(CN)_2^-$ anion based ionic liquid, they observed two modes, one at around 114 cm^{-1} and another around 55 cm^{-1}. The modes were attributed to the stretching and bending vibrations of the cation-anion hydrogen bonds ($^+$C-H...A$^-$) respectively. They also noticed a red shift in these mode frequencies in ionic liquids with weakly coordinating anions, i.e., the weaker the cation-anion interaction, the lower are these frequencies. The hydrogen bond between hexafluorophosphate, PF_6 and the imidazolium cation is rather weak, as reported by us through *ab initio* MD simulations earlier [61]. Hence, the peak positions of these intermolecular modes for [bmim][PF_6] must be considerably red shifted from the values reported for ILs with $N(CN)_2$. Results of the VDOS shown in Figure 2.11 confirm this view. At 300 K, the VDOS of the cation exhibits two clear peaks at 25 cm^{-1} and 75 cm^{-1}. The VDOS of the anion shows a solitary peak at around 30 cm^{-1}. The second peak in the spectra for cations (present at around 75 cm^{-1}) is pronounced at lower temperatures (300 K and below) and diminishes as temperature increased. With an increase in temperature, both the cation and anion mode frequencies soften, in agreement with Raman spectroscopic results of Ribeiro [62].

Figure 2.12 shows the VDOS for the center of mass of the imidazole ring, methyl group, terminal methyl group of the butyl chain and butyl chain at 300 K. It is noticed that the methyl groups predominantly contribute to the second peak (~ 70 cm^{-1}), which appears in the VDOS of the COM of the cation (Figure 2.11). There is a contribution from the imidazolium ring as well, but the butyl chain does not have any distinct modes in this region. The peaks in the anion VDOS are sharper. The peaks for both the ions show a marginal blue shift upon decreasing temperature indicating that the motion is more constrained at lower temperatures.

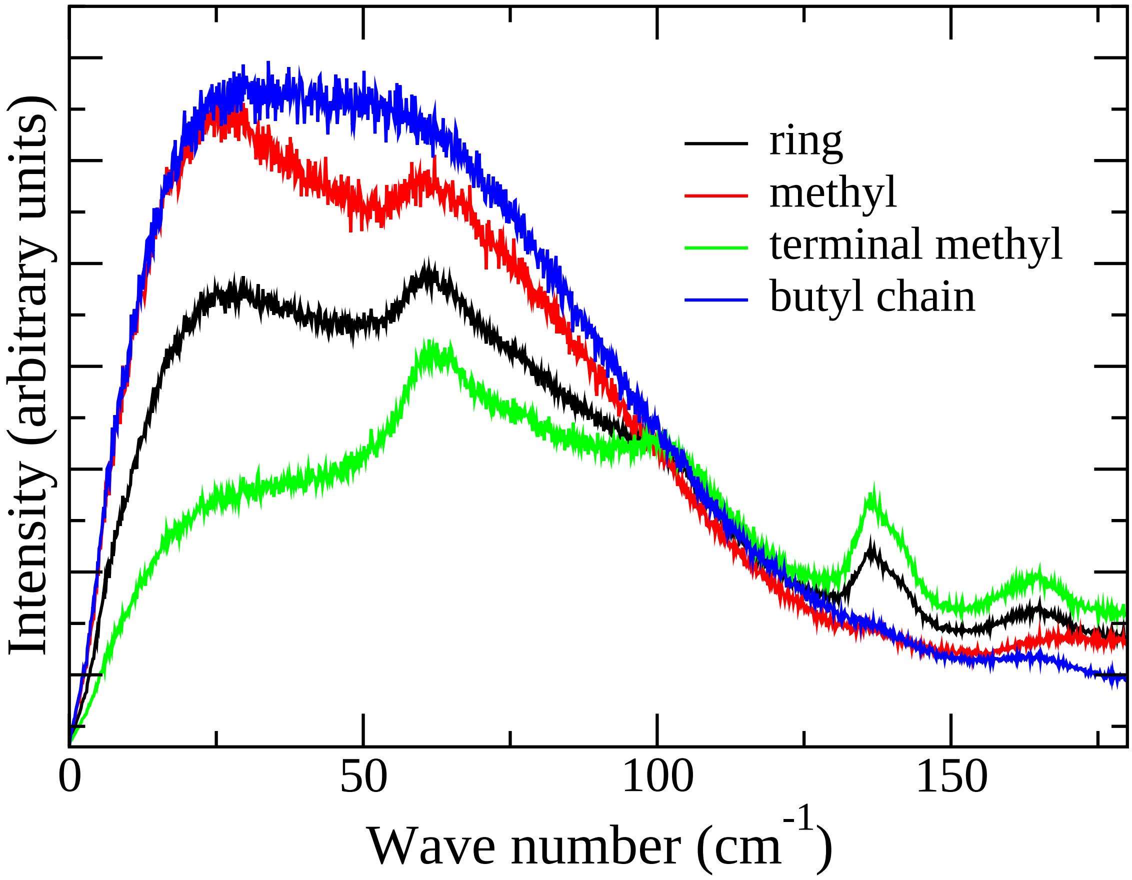

Figure 2.12: Vibrational density of states of the center of mass of the imidazolium ring, methyl group, terminal methyl group of the butyl chain and of the butyl chain of the cation at 300 K.

2.3.7 Structural Heterogeneity

Correlations between structural and dynamical heterogeneities have been reported in supercooled liquids. Chille *et al* have demonstrated structural heterogeneity in supercooled m-toluidine, specifically through the radial-angular pair distribution function g(R,θ) [63]. They observed preferential near neighbour positions and orientations for slow moving molecules, while none was found for the fast moving ones. A similar strategy has been adopted to study the structural origin of the observed dynamical heterogeneities in this ionic liquid. The function g(R,cos θ) is defined as,

$$g(R, \cos\theta) = \frac{\langle \sum_{i=1}^{N_i} \sum_{j=1}^{N_j} \delta(R - R_{ij})\delta(\cos\theta - \cos\theta_{ij}\rangle}{2\pi R^2 \Delta R \Delta \cos\theta N_i N_j V^{-1}} \tag{2.11}$$

where the angular brackets denote averaging over time, the sum on i is over the cations and that on j is over the anions. V is the volume of the simulation box. N_i and N_j are the number of cations and anions respectively. R_{ij} is the distance between the hydrogen atoms of the cation ring and the fluorine atoms of the anion. θ_{ij} is the angle between the following two vectors: (i) the one joining the hydrogen atoms to the carbon atom on the imidazolium ring to which they are covalently bonded and (ii) the vector joining the cation ring hydrogen atoms to any of the fluorine atoms of the anion.

Through this analysis, an attempt is made to find out if there is any preferential position and orientation between the ions which can be considered as a complex, however short-lived it may be [64]. g(R,$\cos\theta$) has been calculated at 300 K between all the cations and anions. It is seen that the most probable position for ion pair is linear (C-$\hat{\mathrm{H}}$-F $\approx 180^o$), as is expected for a hydrogen bond [11]. Mobile and immobile subensembles of cations and anions are defined in a similar way as was introduced by Margulis *et al* [51]. Based on the mean squared displacements of each of the ions at 300 K (in the time range around 5 ns), the fastest 20 ($\approx 8\%$ of the ions) and the slowest 20 of cations and anions were identified.

In a path breaking study, Margulis *et al* [51] had studied the pair distribution functions for the cations and the anions for mobile-mobile, immobile-immobile, mobile-immobile subensembles and found that the spatial correlation among the mobile ions (i.e., cation-cation or anion-anion) and that among the immobile ions are much higher than those between mobile-immobile cross correlations. In contrast to their approach, the “cation-anion” pair distributions for these subensembles were studied. Figure 2.13 shows g(R,cos(θ)) along the C_3-H_{11} direction.

It can be observed that the probability densities for the mobile cations-mobile anions and that for the immobile cations-immobile anions are distinctly higher than that for the mobile cations-immobile anions. $g(R,\cos\theta)$ with respect to the C_4-H_{12} and C_5-H_{13} bonds too agree with these conclusions. This analysis shows that *neighbouring counterions (or, in general, ion complexes) share mobility indices as well – mobile cations tend to associate with those anions which too are mobile.*

The relationship between structural and dynamical heterogeneities has been further probed in the following manner. The simulation box is divided into 27 equal sized cubic boxes each containing about 9 to 10 cations and nearly an equal number of anions. For this analysis, ions which were present in each of these small boxes at the start of the analysis trajectory were considered to "belong" to the same box for the full simulation time. The MSDs for each of the ions at 300 K over the duration of 5 ns were then calculated and this quantity was averaged over all ions (of a particular ion type, i.e., cation or anion) present in that box. As expected, the mean displacement of ions in some boxes was much higher than in some others, indicating that the dynamical behaviour is related to location. Note, however that such dynamical heterogeneities are dependent on the timescales of the probe, in this case that of the MD simulation (which, in the present case, is a few nanoseconds). In macroscopic timescales, ions present in all regions of the system will have equal average mobilities. Two small boxes (*aka* regions inside the simulation cell) over the time duration of 5 ns were identified: one in which the mean MSD of the ions was the highest, and another in which the value was the lowest. The ratio of diffusion coefficients of ions between the fast and the slow boxes was around three.

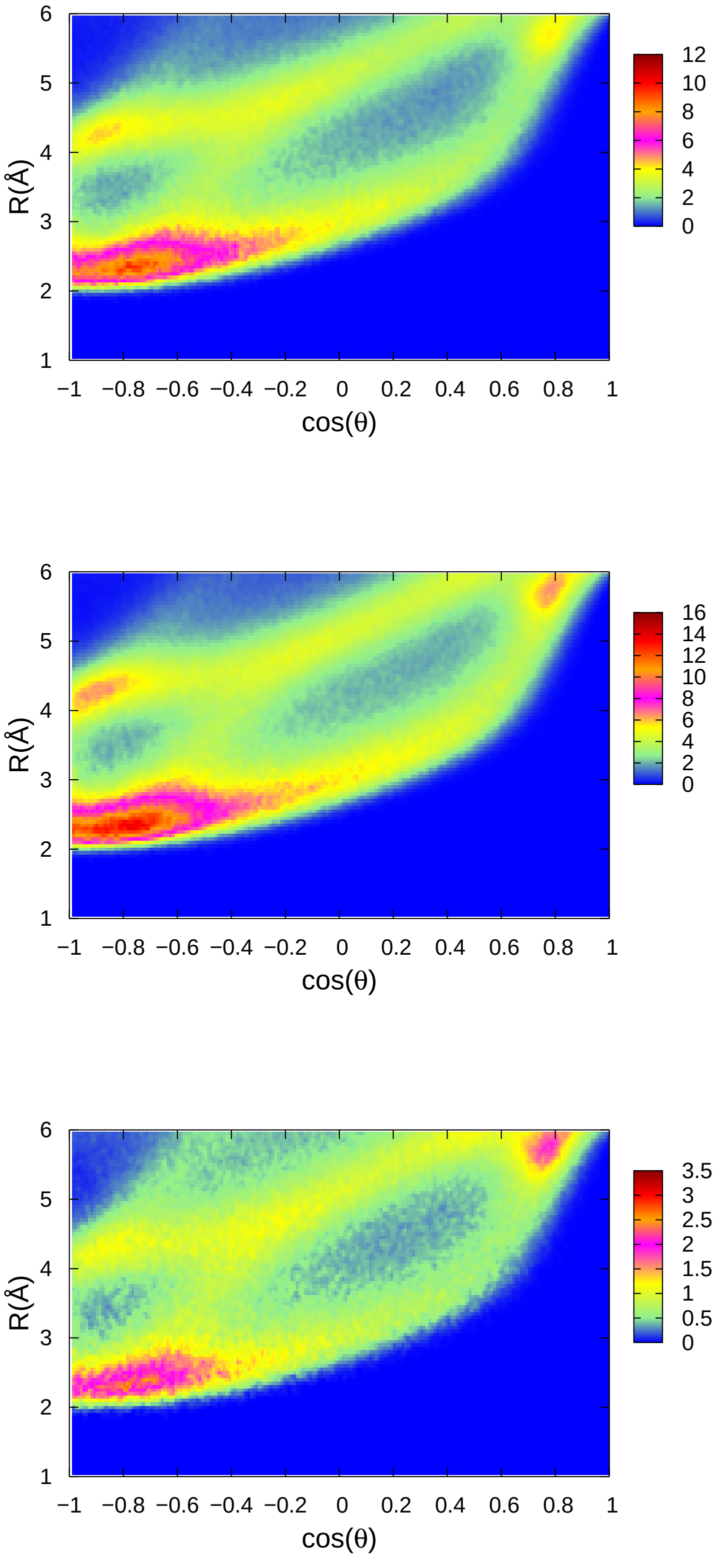

Figure 2.13: Radial-angular pair distribution function (g(R,cos(θ))) Top: mobile cations - mobile anions Middle: immobile cations - immobile anions Bottom: mobile cations - immobile anions. Note the difference in the maximum value of the bottom panel, compared to those in the top and middle panels.

The function g(R,cos θ) for cations located in these two regions has been calculated. Through this analysis, an attempted has been made to probe if differences in cation mobilities were related to differences in cation-anion near neighbour arrangements (if any). Again, the cation-anion g(R,cos θ) for cations present in the fastest and the slowest regions were calculated. In Figure 2.14, the difference in this quantity between these two regions (slow region's minus that for the fast region) is shown.

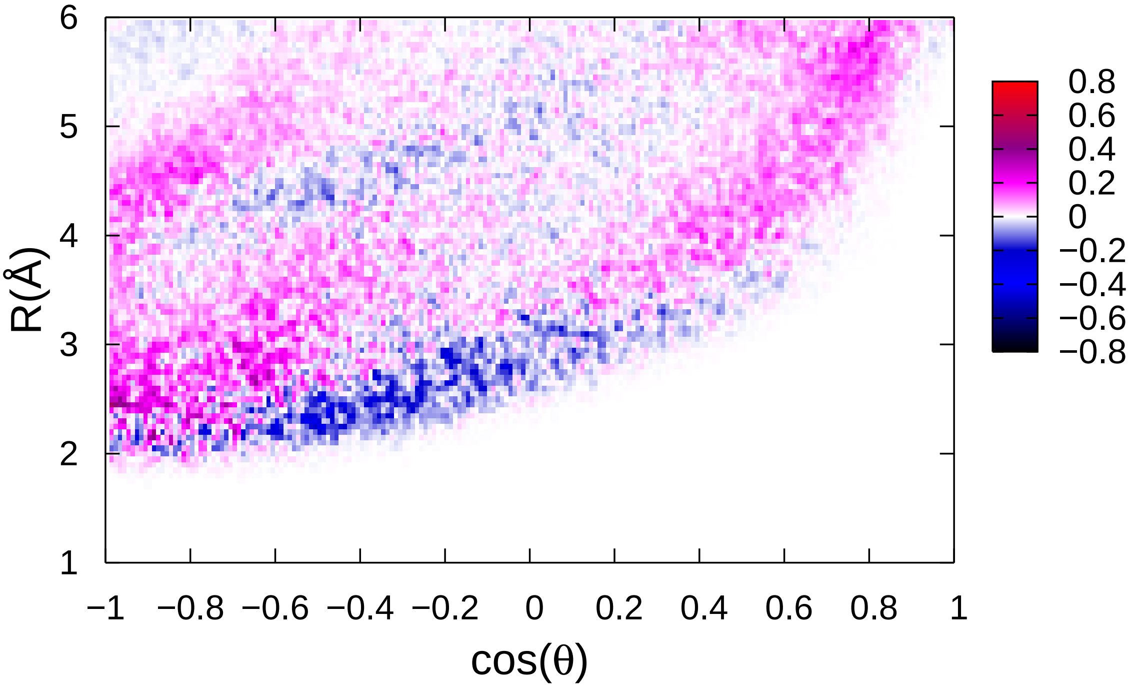

Figure 2.14: A difference plot of the cation-anion g(R,cos(θ)) defined as the function for slow cations present in a region of the simulation box minus that for fast cations present in another region.

There is a non-negligible difference in the probability density of anions located around fast cations than around slow cations. The values were significantly positive, denoting a larger coordination of anions around a slow cation than around a fast one. The first coordination number from the cation-anion pair correlation function too attests to this fact. Around 4% more anions surround a slow cation relative to the number around a fast cation. Although this difference may appear to be small, it is significant as the g(R,cos θ) function as well this difference has been averaged over the five independent trajectories and ensemble averaged. Thus, the observed dynamical heterogeneity is likely linked to subtle differences in the cation-anion near neighbour structure.

Zhao *et al* showed that neutral ion pairs are short lived and do not fully account for the observed difference between the total electrical conductivity and the Nernst-Einstein value [28]. Here, it is shown that a mobile ion is likely to be surrounded by mobile counterions. The spatial extent of such a preferential environment (preference determined by individual ion mobility) is as yet undetermined. Our attempts to answer this question through the calculation of the structure factor between fast ions (or, slow ones) did not yield any conclusive answer [65]. However, further efforts in this direction are required.

2.4 Conclusions

The rich dynamics exhibited by room temperature ionic liquids have been explored through a study of liquid [bmim][PF_6]. Using atomistic molecular dynamics simulations of this system modelled with a well established force field, results on diffusion, electrical conductivity, and the relaxation of the incoherent intermediate scattering function (F_s(K,t)) have been presented. In particular, the decay of F_s(K,t) for the hydrogen atoms present in the cation compared extremely well with the neutron scattering results of Triolo and coworkers [12]. The current results, cumulatively seen with the earlier MD studies on the structure and transport of [bmim][PF_6] [30, 32] provide further validation of the potential model employed.

It was observed, the cations exhibited a larger heterogeneity in their dynamics than the anions. The decay of F_s(K,t) could be captured using the modified Kohlrausch-Williams-Watts function and the presence of two relaxation regimes β (fast and exponential) and α (slow and stretched exponential) could be deduced. In line with experiment, it was found that the stretching exponent increased with temperature and attained a value of unity at high temperatures. It decreased with increasing wave vector. The vibrational density of states of the cations exhibited a bimodal behaviour at low temperatures, corresponding to intermolecular dynamics. Specific motions to which these features can be assigned could be studied by applying instantaneous normal mode analysis, which is planned to carry out in the future. The low frequency VDOS corresponding to the anions were relatively sharper and were red shifted with respect to that of the cation. By analyzing the contributions from different moieties constituting the cation, the 70 cm^{-1} peak specifically could be assign to the motion of methyl groups.

An interesting new result that has emerged in the current work is that mobile anions tend to coordinate mobile cations and less mobile anions coordinate less mobile cations. In contrast, the population density of immobile anions around mobile cations (or vice versa) was significantly lesser than that in the former categories. Thus the dynamical heterogeneity displayed by ions of one kind is mirrored by the counterion shell around the central ion. Evidence of a small, but non-negligible difference in the probability density of anions (irrespective of whether the anions are mobile or not) around a “fast” cation relative to that around a “slow” cation has also been observed. In particular, the anion density was slightly larger along the C_3-$H_1$1 vector when it coordinates a slow cation. The observed dynamical heterogeneity is thus interrelated to subtle distinctions in the cation-anion first coordination shell.

Bibliography

[1] H. Weingärtner, *Angew. Chem. Int. Ed.*, **47**, 654-670, (2008).

[2] R.M. Lynden-Bell, M.G. Del Popolo, T.G.A. Youngs, J. Kohanoff, C.G. Hanke, J.B. Harper, C.C. Pinilla, *Acc. Chem. Res.*, **40**, 1138-1145, (2007).

[3] J.N.A.C. Lopes, A.A.H. Padua, *J. Phys. Chem. B*, **110**, 3330-3335, (2006).

[4] Y. Wang, G.A. Voth, *J. Phys. Chem. B*, **110**, 18601-18608, (2006).

[5] B.L. Bhargava, S. Balasubramanian, M.L. Klein, *Chem. Commun.*, 3339-3351, (2008).

[6] A. Noda, K. Hayamizu, M. Watanabe, *J. Phys. Chem. B*, **105**, 4603-4610, (2001).

[7] T. Köddermann, C. Wertz, A. Heintz, R. Ludwig, *ChemPhysChem*, **7**, 1944-1949, (2006).

[8] S. Zahn, G. Bruns, J. Thar, B. Kirchner, *Phys. Chem. Chem. Phys.*, **10**, 6921-6924, (2010).

[9] J. Thar, M. Brehm, A.P. Seitsonen, B. Kirchner, *J. Phys. Chem. B*, **113**, 15129-15132, (2009).

[10] K. Fumino, A. Wulf, R. Ludwig, *Angew. Chem. Int. Ed.*, **47**, 8731-8734, (2008).

[11] A. Wulf, K. Fumino, R. Ludwig, *Angew. Chem. Int. Ed.*, **49**, 449-453, (2010).

[12] A. Triolo, V. Arrighi, F. Juranyi, S. Janssen, C.M. Gordon, *J. Chem. Phys.*, **119**, 8549-8557, (2003).

[13] A. Triolo, O. Russina, C. Hardacre, M. Nieuwenhuyzen, M.A. Gonzalez, H. Grimm, *J. Phys. Chem. B*, **109**, 22061-22066, (2005).

[14] O. Russina, M. Beiner, C. Pappas, M. Russina, V. Arrighi, T. Unruh, C.L. Mullan, C. Hardacre, A. Triolo, *J. Phys. Chem. B*, **113**, 8469-8474, (2009).

[15] C. Daguenet, P.J. Dyson, I. Krossing, A. Oleinikova, J. Slattery, C. Wakai, H. Weingärtner, *J. Phys. Chem. B*, **110**, 12682-12688, (2006).

[16] H. Weingärtner, P. Sasisanker, C. Daguenet, P.J. Dyson, I. Krossing, J.M. Slattery, T. Schubert, *J. Phys. Chem. B*, **111**, 4775-4780, (2007).

[17] C. Schröder, C. Wakai, H. Weingärtner, O. Steinhauser, *J. Chem. Phys.*, **126**, 084511, (2007).

[18] D.A. Turton, J. Hunger, A. Stoppa, G. Hefter, A. Thoman, M. Walther, R. Buchner, K. Wynne, *J. Am. Chem. Soc.*, **131**, 11140-11146, (2009).

[19] J. Andrade, E.S. Böes, H. Stassen, *J. Phys. Chem. B*, **112**, 8966-8974, (2008).

[20] A. Wulf, K. Fumino, D. Michalik, R. Ludwig, *ChemPhysChem*, **8**, 2265-2269, (2007).

[21] T. Köddermann, R. Ludwig, D. Paschek, *ChemPhysChem*, **9**, 1851-1858, (2008).

[22] P.A. Hunt, I.R. Gould, B. Kirchner, *Aus. J. Chem.*, **60**, 9-14, (2007).

[23] P.A. Hunt, B. Kirchner, T. Welton, *Chem.-Eur.J.*, **12**, 6762-6775, (2006).

[24] S.M. Urahata, M.C.C. Ribeiro, *J. Chem. Phys.*, **122**, 024511, (2005).

[25] W. Jiang, T. Yan, Y. Wang, G.A. Voth, *J. Phys. Chem. B*, **112**, 3121-3131, (2008).

[26] M.H. Kowsari, S. Alavi, M. Ashrafizaadeh, B. Najafi, *J. Chem. Phys.*, **129**, 224508, (2008).

[27] M.H. Kowsari, S. Alavi, M. Ashrafizaadeh, B. Najafi, *J. Chem. Phys.*, **130**, 014703, (2009).

[28] W. Zhao, F. Leroy, B. Heggen, S. Zahn, B. Kirchner, S. Balasubramanian, F. Müller-Plathe, *J. Am. Chem. Soc.*, **131**, 15825-15833, (2009).

[29] Y. Shim, H.J. Kim, *J. Phys. Chem. B*, **112**, 11028-11038, (2008).

[30] B.L. Bhargava, S. Balasubramanian, *J. Chem. Phys.*, **127**, 114510, (2007).

[31] B.L. Bhargava, M.L. Klein, S. Balasubramanian, *ChemPhysChem*, **9**, 67-70, (2008).

[32] W. Zhao, F. Leroy, S. Balasubramanian and F. Müller-Plathe, *J. Phys. Chem. B*, **112**, 8129-8133, (2008).

[33] S.J. Plimpton, *J. Comp. Phys.*, **117**, 1, (1995).

[34] R.W. Hockney, J.W. Eastwood, *Computer Simulation Using Particles*, Taylor and Francis, New York, (1988).

[35] C. Cadena, Q. Zhao, R.Q. Snurr, E.J. Maginn, *J. Phys. Chem. B*, **110**, 2821-2832, (2006).

[36] J. Qian, R. Hentschke, A. Heuer, *J. Chem. Phys.*, **110**, 4514-4522, (1999).

[37] M.G. Del Popolo, G.A. Voth, *J. Phys. Chem. B*, **108**, 1744-1752, (2004).

[38] Y. Gembremichael, T.B. Schroder, F.W. Starr, S.C. Glotzer, *Phys. Rev. E*, **64**, 051503-051515, (2001).

[39] D. Frenkel and B. Smit, *Understanding Molecular Simulations*, Academic Press, New York (1996).

[40] H. Tokuda, K. Hayamizu, K. Ishii, Md. A.B.H. Susan, M. Watanabe, *J. Phys. Chem. B*, **108**, 16593-16600, (2004).

[41] B.L. Bhargava, S. Balasubramanian, *J. Chem. Phys.*, **123**, 144505, (2005); B. L. Bhargava, S. Balasubramanian, *ibid*, **125**, 219901E, (2006).

[42] F. Dommert, J. Schmidt, B. Qiao, Y. Zhao, C. Krekeler, L. Delle Site, R. Berger, C. Holm, *J. Chem. Phys.*, **129**, 224501, (2008).

[43] Y. Inamura, O. Yamamuro, S. Hayashi, H. Hamaguchi, *Physica B*, **385-386**, 732-734, (2006).

[44] J.P. Hansen, I.R. McDonald, *Theory of simple liquids*, Academic, London (1990).

[45] F. Müller-Plathe, W.F. van Gunsteren, *J. Chem. Phys.*, **103**, 4745-4756, (1995).

[46] L.J.A. Siqueira, M.C.C. Ribeiro, *J. Chem. Phys.*, **125**, 214903, (2006).

[47] M. Kanakubo, K.R. Harris, N. Tsuchihashi, K. Ibuki, M. Ueno, *J. Phys. Chem. B*, **111**, 2062-2069, (2007).

[48] H. Tokuda, K. Ishii, Md. A.B.H. Susan, S. Tsuzuki, K. Hayamizu, M. Watanabe, *J. Phys. Chem. B*, **110**, 2833-2839, (2006).

[49] W. Kob, C. Donati, S.J. Plimpton, P.H. Poole, S.C. Glotzer, *Phys. Rev. Lett.*, **79**, 2827-2830, 1997.

[50] J. Qian. R. Hentschke, A. Heuer, *J. Chem. Phys.*, **111**, 10177-10182, (1999).

[51] Z. Hu, C.J. Margulis, *Proc. Natl. Acad. Sci.*, **103**, 831-836, (2006).

[52] Z. Hu, C.J. Margulis, *Acc. Chem. Res.*, **40**, 1097-1105, (2007).

[53] L. van Hove, *Phys. Rev.*, **95**, 249-262, (1954).

[54] K.W. Herwig, Z. Wu, P.Dai, H. Taub, *J. Chem. Phys.*, **107**, 5186-5196, (1997).

[55] J. Habasaki, K.L. Ngai, *J. Chem. Phys.* , **129**, 194501, (2008).

[56] A. Triolo, A. Mandanici, O. Russina, V. Rodriguez-Mora, M. Cutroni, C. Hardacre, M. Nieuwenhuyzen, H. Bleif, L. Keller, M.A. Ramos, *J. Phys. Chem. B*, **110**, 21357-21364, (2006).

[57] T. Ishida, K. Nishikawa, H. Shirota, *J. Phys. Chem. B*, **113**, 9840-9851, (2009).

[58] G. Giraud, C.M. Gordon, I.R. Dunkin, K. Wynne, *J. Chem. Phys.*, **119**, 464-477, (2003).

[59] T. Köddermann, K. Fumino, R. Ludwig, J.N.C. Lopes, A.A.H. Padua, *ChemPhysChem*, **10**, 1181-1186, (2009).

[60] A. Wulf, K. Fumino, R. Ludwig, and P.F. Taday, *ChemPhysChem*, **11**, 349-353, (2010).

[61] B.L. Bhargava, S. Balasubramanian, *J. Phys. Chem. B*, **111**, 4477-4487, (2007).

[62] M.C.C. Ribeiro, *J. Phys. Chem. B*, **111**, 5008-5015, (2007).

[63] R. Chelli, G. Cardini, P. Procacci, R. Righini, S. Califano, *J. Chem. Phys.*, **119**, 357-363, (2003).

[64] B. Qiao, C. Krekeler, R. Berger, L. Delle Site, C. Holm, *J. Phys. Chem. B*, **112**, 1743-1751, (2008).

[65] We analyzed a MD simulation trajectory containing 2048 ion pairs of the same IL to study the correlation length (if any) between ions which share mobility indices. This effort too did not provide any definitive conclusions.

Chapter 3

Low-Frequency Vibrational Modes of Room Temperature Ionic Liquids

3.1 Introduction

The previous chapter demonstrated the complex dynamics present in RTILs, which is a consequence of the variety of possible interactions among the ions. RTILs are composed of large molecular ions which not only interact via Coulombic forces but could also exhibit interactions such as dispersion, hydrogen bonding [1–3], and π stacking [4]. Hence, the energy basins (landscape) in which the ions are situated is likely to be rich [5–10]. The curvature of the local minima in which the ions are located is related to the frequency spectrum. The characterization of vibrational modes of room temperature ionic liquids (RTILs) is a topic of intense current research. Specifically, the low frequency (less than 100 cm^{-1}) region of the vibrational spectrum is believed to probe interactions between ions. A large number of experimental studies such as terahertz spectroscopy [11,12], dielectric spectroscopy [13–15], nuclear magnetic resonance spectroscopy [15], heterodyne-detected Raman-induced Kerr effect [14, 16, 17], infrared spectroscopy (FTIR) [18, 19] along with *ab initio* calculations [20–25] have been carried out in the past to characterize the ionic motions in ILs. Recent attention has been focussed on the features present in the low frequency region of the vibrational spectra of many ionic liquids [26–36].

Ludwig *et al* investigated this region of the spectra using far-infrared (IR) spectroscopy, augmented by zero temperature, density functional theory (DFT) calculations of small clusters of neutral ion pairs in gas phase [26, 27, 29]. They assigned the low-frequency modes present between 50 and 120 cm^{-1} to bending and stretching motions of hydrogen bonds that exist between the cations and anions (C^{+}–H...A^{-}) [26,27]. In addition, they compared the far IR spectra of two ILs with the same anion, BF_4 but with different cations, $[C_4C_1\mathrm{im}]^+$, and $[C_4C_1\mathrm{mim}]^+$ [29]. The latter cannot form a cation-anion hydrogen bond through the C_2 site, while the former can [29]. Although a broad band exists in both the liquids below 100 cm^{-1}, it was found to be slightly blue shifted in the liquid containing the first cation. Thus hydrogen bonding capability appears to harden the potential energy surface. While the vibrational feature in aprotic ILs appears below 150 cm^{-1}, it is considerably blue shifted to about 250 cm^{-1} in a protic IL containing a cation such as propylammonium [29]. To investigate the role of hydrogen bonded interactions in determining the spectrum in the far infrared regime, they recently carried out FTIR measurements of ILs containing imidazolium based cations possessing methyl group substitutions at the second and the third positions of the imidazolium ring [32]. They observed a linear dependence between the number of possible cation-anion hydrogen bonds and the position of the low frequency peak [32]. A linear dependence was also observed between the ion binding energy (calculated from quantum chemical calculations of a tetramer) and the peak frequency.

Buffeteau *et al* have combined polarized attenuated reflection and transmittance spectra and were able to determine the optical constants of imidazolium based ILs in the far-infrared region [34]. Specifically, they found a red shift of around 9.5 cm^{-1} in the peak position of the low frequency band when a methyl group is bonded to the C_2 position of the cation, compared to that for the protiated cation. However, they did not observe any change in the intensity of the peak. In addition, they observed a large band in this region for the ionic liquid, $[NBuMe_3][TFSI]$ which does not have any cation-anion hydrogen bond. Based on these observations, they concluded that the low frequency band cannot exclusively be caused by the motions involving the C_2-H...A^- hydrogen bond. They also suggested that the band could arise from long range electrostatic interactions and that molecular dynamics (MD) simulations may constitute a more appropriate approach.

The present study attempts to obtain an understanding of the ion motions related to the low frequency modes in room temperature ionic liquids. Towards this aim, we have carried out Hessian calculations of four bulk liquids modelled using empirical potential based atomistic molecular dynamics simulations. These results are augmented further by gas phase quantum chemical calculations of ion pairs and also by Hessian calculations of crystalline $[bmim][PF_6]$ using both empirical force field and density functional theory. Anticipating our results, we state that these modes are interionic in character; they are not localized to the C-H...A atoms alone. The low frequency band arises primarily from short range interionic interactions and the exact peak position is modulated by the cation-anion hydrogen bond strength.

3.2 Details of Simulation and Methodology

Empirical potential based simulations: Classical molecular dynamics (MD) simulations of four different ionic liquids *viz.,* 1-*n*-butyl-3-methylimidazolium nitrate ($[bmim][NO_3]$), 1-*n*-butyl-3-methylimidazolium tetrafluoroborate ($[bmim][BF_4]$), 1-*n*-butyl-3-methylimidazolium hexafluorophosphate ($[bmim][PF_6]$), 1-*n*-butyl-3-methylimidazolium bis(trifluoromethanesulfonyl)imide ([bmim][NTf_2]) have been carried out. The force field and interaction parameters for the [bmim][PF_6] system has been taken from the work of Bhargava and Balasubramanian [37], and that for [bmim][BF_4] from the model developed by Wang *et al* [38]. [bmim][NTf_2] and [bmim][NO_3] were modelled using Ludwig *et al*'s [39] and the Lopes-Padua [40] force fields respectively. The simulations were performed at a temperature of 300 K in the canonical ensemble, using the Nosé-Hoover thermostat. Densities of these liquids were determined by carrying out constant pressure-constant temperature MD simulations (at 1 atmosphere pressure). These were later used in obtaining the dimensions of the simulation box for the four liquids. Each of the liquid simulation contained 100 ion pairs in a cubic box. The corresponding number of atoms in the systems were 2900, 3000, 3200, and 4000 for [bmim][NO_3], [bmim][BF_4], [bmim][PF_6], and [bmim][NTf_2] respectively. Three dimensional periodic boundary conditions were employed.

In addition, simulations of the triclinic crystalline form of [bmim][PF_6] [41, 42] consisting of 128 ion pairs (4096 atoms) were performed at a temperature of 100 K. The simulation box consisted of 4x4x4 unit cells along the crystallographic axes. LAMMPS [43] program has been used to perform the MD simulations.

The equations of motion were integrated using the velocity Verlet algorithm with a time step of 0.5 fs. Particle-particle particle-mesh (PPPM) [44] k-space solver has been employed for the Coulombic interactions and long range corrections for the energy and pressure were applied. The cut-off distance for the non-bonded interactions were set to 13 Å for [bmim][PF_6] and to 12 Å for the other liquids. The equilibration period for each system was around 5 ns. Later, analysis trajectories were generated over a duration of 10 ns during which atom coordinates were stored at an interval of 500 ps, to obtain 20 frames for each IL.

Quenched normal modes (QNM) : The twenty configurations obtained from each IL were quenched (energy minimization with respect to atom coordinates) to respective local minima using the conjugate gradient method in LAMMPS. Since the systems investigated here are in bulk, tight optimizations such as those achieved in gas phase were not possible. In practice, we found that the maximum force on any atom present in the energy minimized configuration was around 0.2 kcal/mol/Å.

We had earlier developed a normal mode analysis (NMA) code to calculate the second derivative matrix (Hessian or dynamical matrix) of the potential energy with respect to the atom coordinates [45]. The components of the Hessian matrix are given by,

$$H_{ij}^{\alpha\beta} = \frac{1}{\sqrt{m_i m_j}} \left(\frac{\partial^2 U}{\partial \beta_j \partial \alpha_i} \right) \tag{3.1}$$

where i, j are atomic indices and α, β represent the Cartesian components of atom coordinates, while m_i is the mass of atom i. The matrix is of order 3N, where N is the number of atoms in the system. Each term in the force field (such as stretch, bend, torsion, non-bonded Lennard-Jones and Coulombic) contributed to every element in the matrix. Analytical second derivatives for each of these force field terms (including that for the k-space part of the Ewald sum) were obtained. The correctness of these derivatives were determined by comparing the same against numerical second derivatives for a given configuration. Also, each term in the potential energy of a system as obtained from this NMA code was checked against values obtained from LAMMPS and were found to match. The dynamical matrix was diagonalized and its eigen values and eigen vectors were obtained. The spectrum (histogram) of eigen values was averaged over results from each of the twenty quenched configurations for every IL. A bin width of 1 cm^{-1} was used to obtain such histograms. Each of these spectra sum to the corresponding total number of degrees of freedom. The eigen vectors were visualized to study atomic displacements corresponding to a mode. The spectrum of frequencies obtained from the dynamical matrix is the vibrational density of states (VDOS) obtained within the harmonic approximation.

One can also obtain the VDOS from the MD trajectory as the power spectrum (Fourier transform) of the time autocorrelation function of the atomic velocities (VACF). The expression is given by,

$$G(\omega) = \frac{1}{k_B T} \sum_j m_j \left[\frac{1}{2\pi} \int_{-\infty}^{\infty} dt \; exp\left(-i\omega t\right) \langle \mathbf{v}_j(0).\mathbf{v}_j(t) \rangle \right] \tag{3.2}$$

where $\mathbf{v}_j(t)$ is the velocity of atom type j at time t and the angular brackets denote an average over the ensemble and over time 0. Such a power spectrum will contain anharmonic contributions as well. Towards this purpose, the velocities of atoms were stored at an interval of 5 fs in a separate MD trajectory generated for 50 ps.

The spatial extent of a mode can be gauged from its participation ratio (PR) [46–48]. It provides the fraction of atoms involved in a normal mode. It is defined as [49],

$$PR_j = \frac{\left(\sum_{i=1}^{N} |\vec{u}_{ij}|^2 \right)^2}{N \sum_{i=1}^{N} |\vec{u}_{ij}|^4} \tag{3.3}$$

where $\vec{u}_{ij}$ is the displacement vector of atom i in vibrational mode j and N is the total number of atoms present in the system. PR is unity for a mode in which all atoms are displaced.

Gas phase calculations: Density functional theory based calculation for one ion pair of [bmim][PF_6] was performed by using the plane wave code, CPMD [50]. The Perdew, Burke and Ernzerhof (PBE) exchange-correlation functional [51] was used with an energy cut off of 150Ry for the wave function and six times this value for the electronic density. Optimizations were carried out under isolated conditions in a cubic box of length 16.0 Å. The Hockney method [52] was used to solve the Poisson equation. Optimizations were pursued until the maximum value of the gradient on the nuclei was 10^{-5} a.u. Normal mode frequencies within the harmonic approximation were obtained.

Calculations on [bmim][PF_6] crystal:

The vibrational density of states (VDOS) of [bmim][PF_6] crystal was obtained both in the harmonic approximation and from a Car-Parrinello molecular dynamics trajectory, using the CPMD software [50]. The simulations were carried out in a periodic box of one unit cell of the crystal. The initial cell parameters and atomic coordinates were taken from experimental data [41]. The Kohn-Sham orbitals were expanded in a plane wave basis with an energy cutoff of 150 Ry for the expansion of the wave function. The energy cutoff for the density was set to six times this value. The Perdew, Burke and Ernzerhof (PBE) exchange-correlation functional [51] was used. The effect of core electrons and the nuclei on the valence electrons was treated with the Troullier-Martins [53] norm conserving pseudopotentials. The cell parameters and atomic positions of the crystal were optimized iteratively to find out their values at which the energy is a minimum. The cell parameters thus obtained differed by less than 0.5% of the experimental values. The forces on the atoms were converged to less than 10^{-5} a.u. In addition, Monkhorst-Pack [54] mesh of size 2x2x2 was used to sample k-points in reciprocal space. The final configuration was used to calculate the VDOS within the harmonic approximation.

Ab initio molecular dynamics (AIMD) simulations were carried out using the Car-Parrinello molecular dynamics algorithm [55]. A Nosé-Hoover chain thermostat [56] was used to maintain the temperature of ions at 100 K with a coupling constant of 3000 cm^{-1}. The equations of motion were integrated with a time step of 3 a.u. An electronic mass of 500 a.u. was used. No restrictions were placed on the temperature of electrons. These simulations were carried out with an energy cut off of 85 Ry for the wave function and four times this value for the electronic density. A trajectory was generated for 18 ps. The conserved quantity was found to be stable with no drifts and the degree of conservation was around 8 parts in 10^7. The generated trajectory was used to calculate the VDOS using the Fourier transform of the velocity autocorrelation function of the ions.

Assignment of the modes was performed by visualizing the atomic displacements in Jmol [57,58].

3.3 Results and Discussions

3.3.1 Force field based calculations

Figure 3.1 compares the low-frequency spectra obtained from NMA and the VDOS obtained from the VACF. The non-zero intensity at zero frequency corresponds to rigid body translation. As is customary, imaginary frequencies are shown on the negative x-axis. The intensity corresponding to such imaginary frequencies is very low and the values of the "frequencies" too are quite small. These arise due to the liquid configuration not being quenched adequately to the local minimum, possibly due to the fact that there exists a force discontinuity at the cutoff for the Lennard-Jones terms. Despite the harmonic approximation used in obtaining the NMA spectrum, it compares very well with the VDOS in all the four liquids. The comparison is excellent for frequencies greater than 500 cm^{-1} , as expected.

Figure 3.2 compares the low-frequency spectra ($<$250 cm^{-1}) obtained from NMA between the four ILs. A prominent feature below 100 cm^{-1} is observed in all the four spectra. Such a feature is present in the experimental far IR data as well. The position of the peaks are shown with arrows and are: 25 cm^{-1}, 35 cm^{-1}, 52 cm^{-1}, and 70 cm^{-1} for [bmim][NTf_2], [bmim][PF_6], [bmim][BF_4], and [bmim][NO_3] respectively. The peak shifts towards lower frequencies and narrows with increase in the size of the anion. The cation-anion interaction too is expected to decrease with increase in the anion size. This behavior is consistent with known experimental data. Danten *et al* [34] compared the spectra for [bmim][PF_6] and [bmim][BF_4]. In

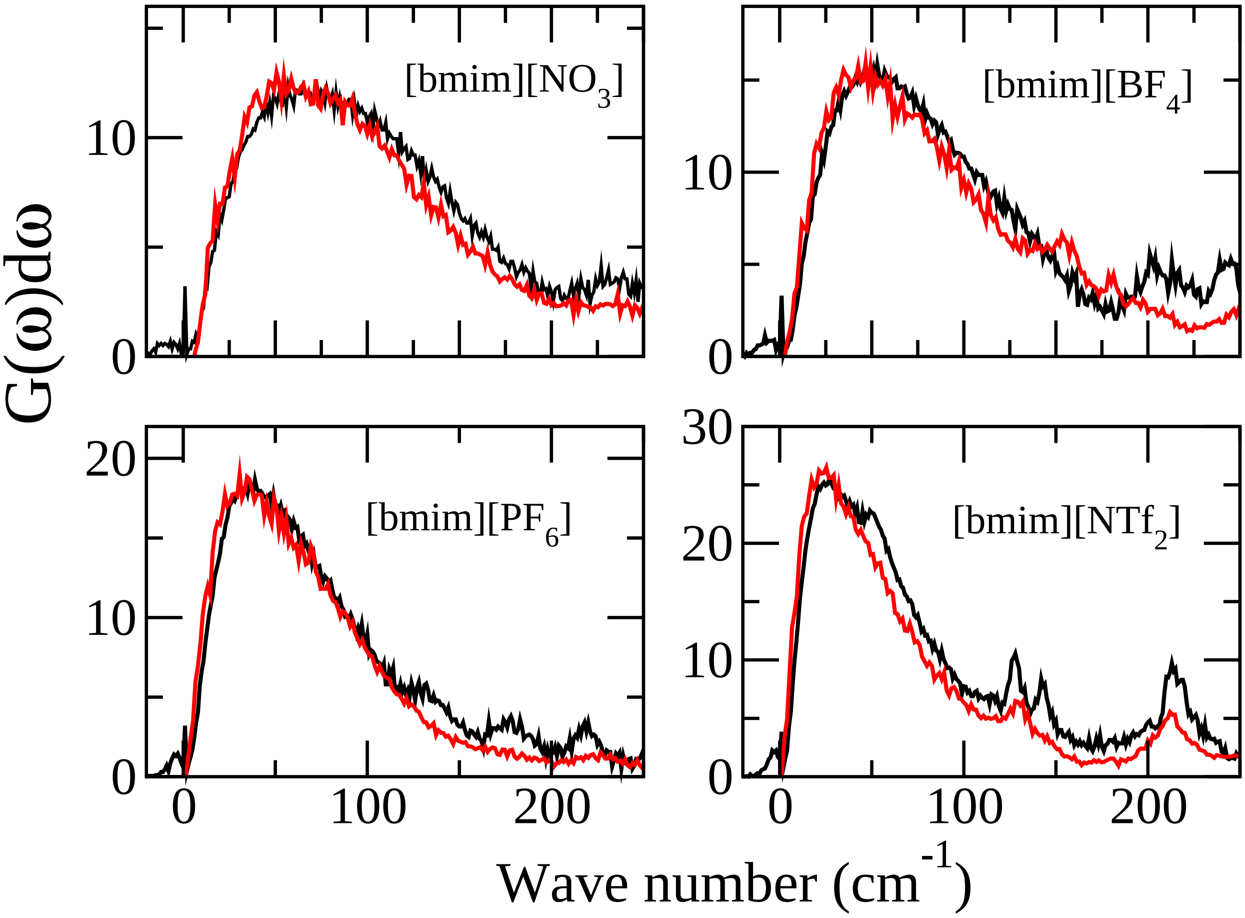

Figure 3.1: Comparison of the low-frequency region of the vibrational density of states (VDOS) obtained from a normal mode analysis (NMA) and as the power spectrum of the velocity autocorrelation function from a MD trajectory for the four ionic liquids. Black and red lines represent the NMA and power spectrum results respectively.

their data too, the low frequency feature for the former is shifted towards lower values and is narrower.

The acidic hydrogen in the imidazolium ring of the cation can form a hydrogen bond with sites on the anion. In [bmim][NO$_3$], the hydrogen bonding site on the anion is the oxygen while in the other three ILs, it is the fluorine atom. Ludwig and coworkers have argued the low frequency feature to arise due to the “stretch” and the “bend” of the D-H...A hydrogen bond (where D and A denote donor and

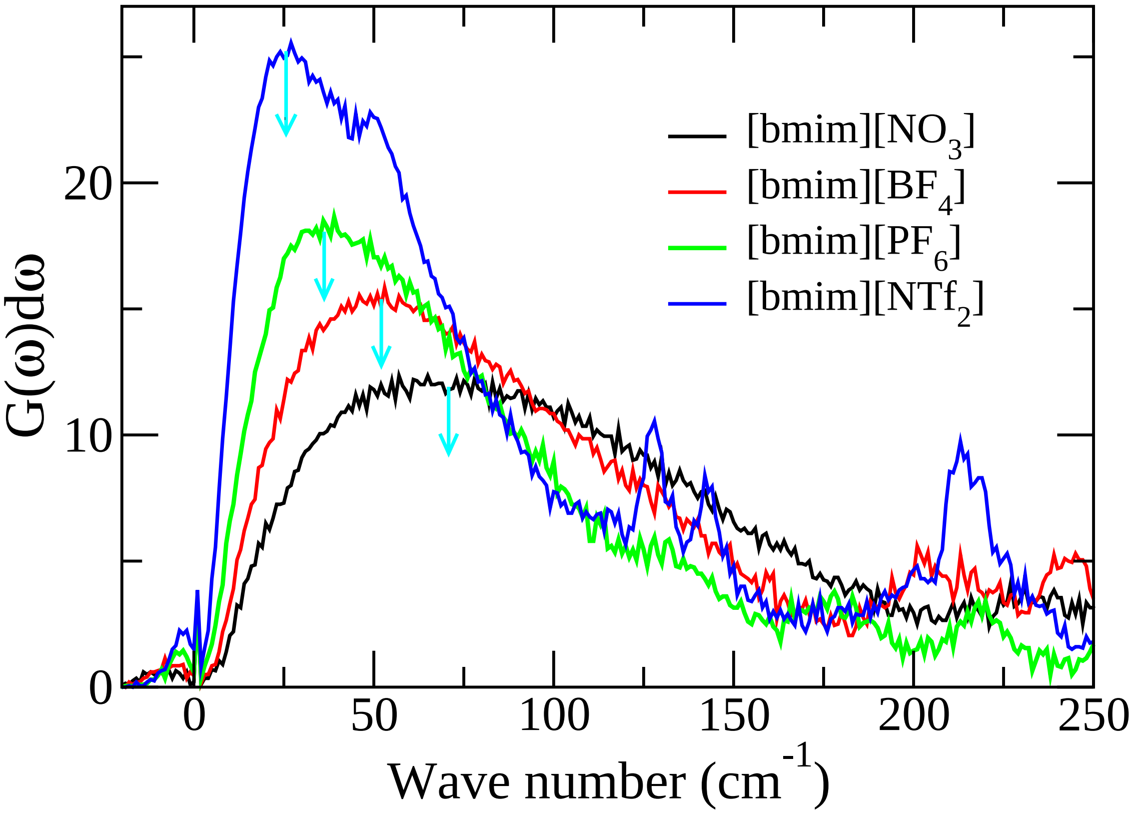

Figure 3.2: Low frequency region of the VDOS obtained from NMA for the four ionic liquids.

acceptor atoms respectively) [32]. They based this assignment from gas phase quantum chemical calculations of clusters of ion pairs. In a recent study, Danten and coworkers differed from this interpretation. In an ionic liquid where the acidic hydrogen of the cation was substituted by a methyl group (thus making it incapable of forming hydrogen bonds with the anion through this site), they found the low frequency feature to be present, with negligible change in the intensity. However, in agreement with the results of Ludwig *et al* [32], they found the peak position in the hydrogen bonded IL to be blue shifted compared to the one that does not have cation-anion hydrogen bonds. This finding coupled with other observations made them to conclude that localised motions due to hydrogen bonding effects are unlikely to cause the sub-100 cm^{-1} feature in ILs. As an alternative, they postulated that long range electrostatics could contribute to this peak.

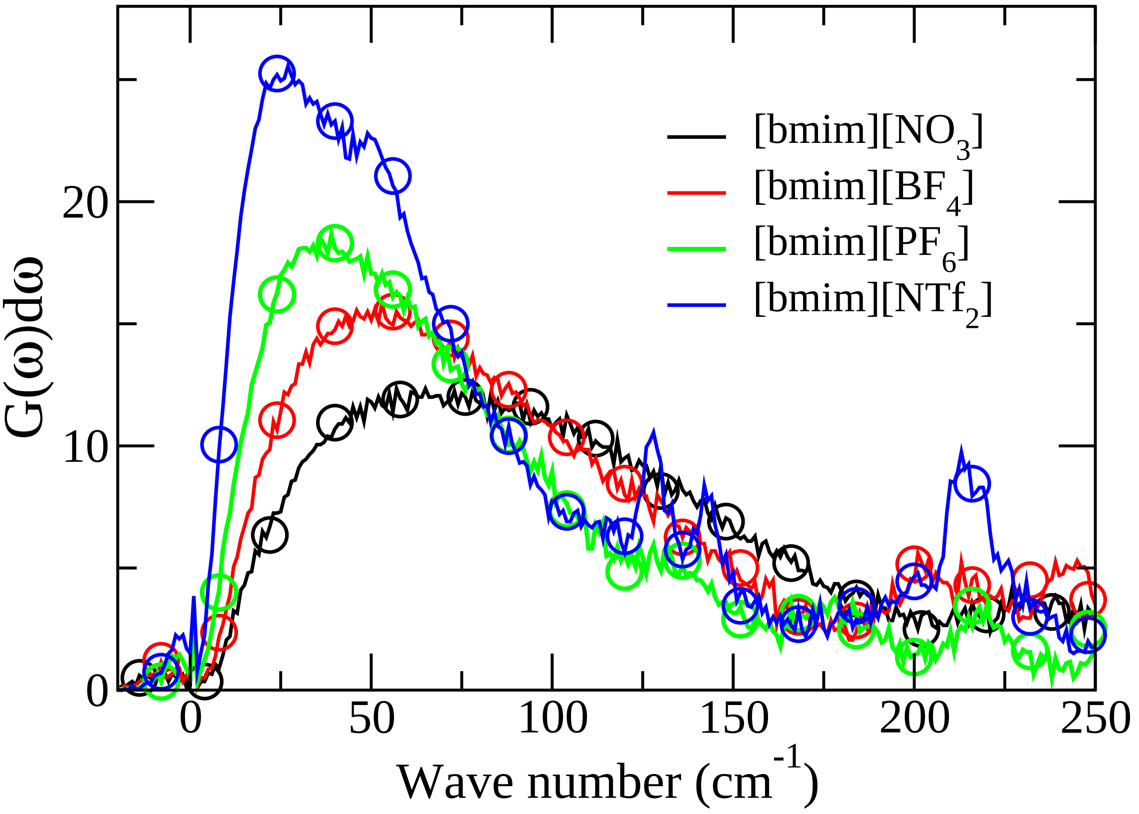

Figure 3.3: Comparison of the low frequency region of VDOS for cation ring deuterated analogs (symbols) against that for the protiated counterparts (lines).

One way to test if the feature arises from motions involving the cation-anion hydrogen bond is to study the isotope effect. One can selectively deuterate the three hydrogen sites on the imidazolium ring of the cation and recalculate the frequency spectrum. In this process, we assumed that the deuterated liquids sample the same potential energy basins as the protiated ones. This implies that we do not have to rerun the MD trajectory for the ring-deuterated cation, and can use the quenched configurations of the protiated liquids. Figure 3.3 shows the frequency calculated for the ring-deuterated ILs using NMA. There is no change in the low-frequency region of the spectra when compared to the protiated counterparts. Had the modes been due to localised motion involving the cation-anion hydrogen bond, a red shift depending on the mass ratio would be expected.

In fact, such a shift is clearly seen for a few of the high frequency modes (related to C-H stretch, N-C-H bend etc..). Shown in Figure 3.4 is the spectrum for [bmim][NO_3] in the range 2100-3000 cm^{-1}. The shift in the C-H stretching mode frequency upon deuteration from a value of $\sim$2920 cm^{-1} to a value of $\sim$2190 cm^{-1} is clear. The ratio between the two stretch frequencies is around 1.33, which is close to the reduced mass ratio of 1.32 between C-H and C-D. The absence of such a shift in the far infrared region suggests that the sub-100cm^{-1} feature cannot be assigned to localized motions involving the cation-anion hydrogen bond.

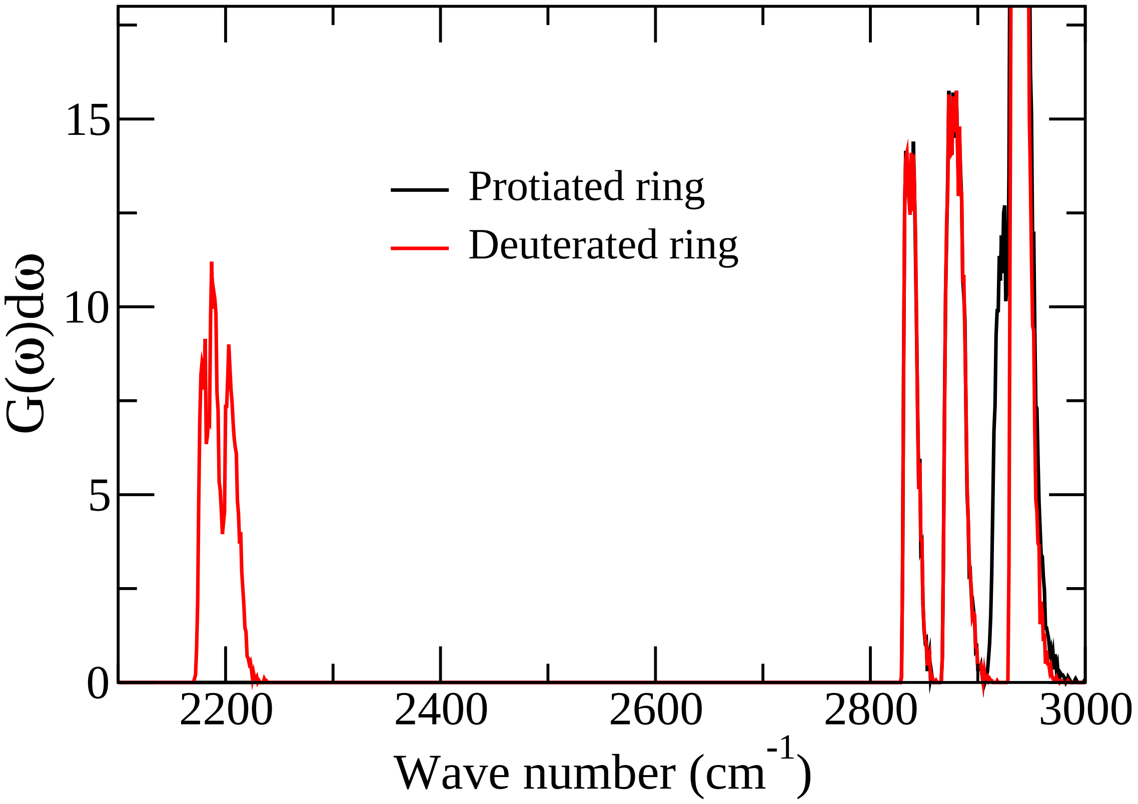

Figure 3.4: VDOS in the C-H (C-D) bond stretch region in [bmim][NO_3] for protiated and ring deuterated samples.

What then is the origin of the low frequency feature? To probe the contribution from long range interactions to the vibrational spectrum below 100 cm^{-1}, we carried out another set of NMA calculations in which the nonbonded interaction cutoff was changed to 6Å for both the Lennard-Jones and the Coulombic terms. Further, the latter was treated as purely a $1/r$ interaction, i.e., without the Ewald summation. The modified potential thus contains only short-range interactions. The spectra for the four liquids obtained using such a seemingly drastic procedure is compared against the original NMA results in Figure 3.5.

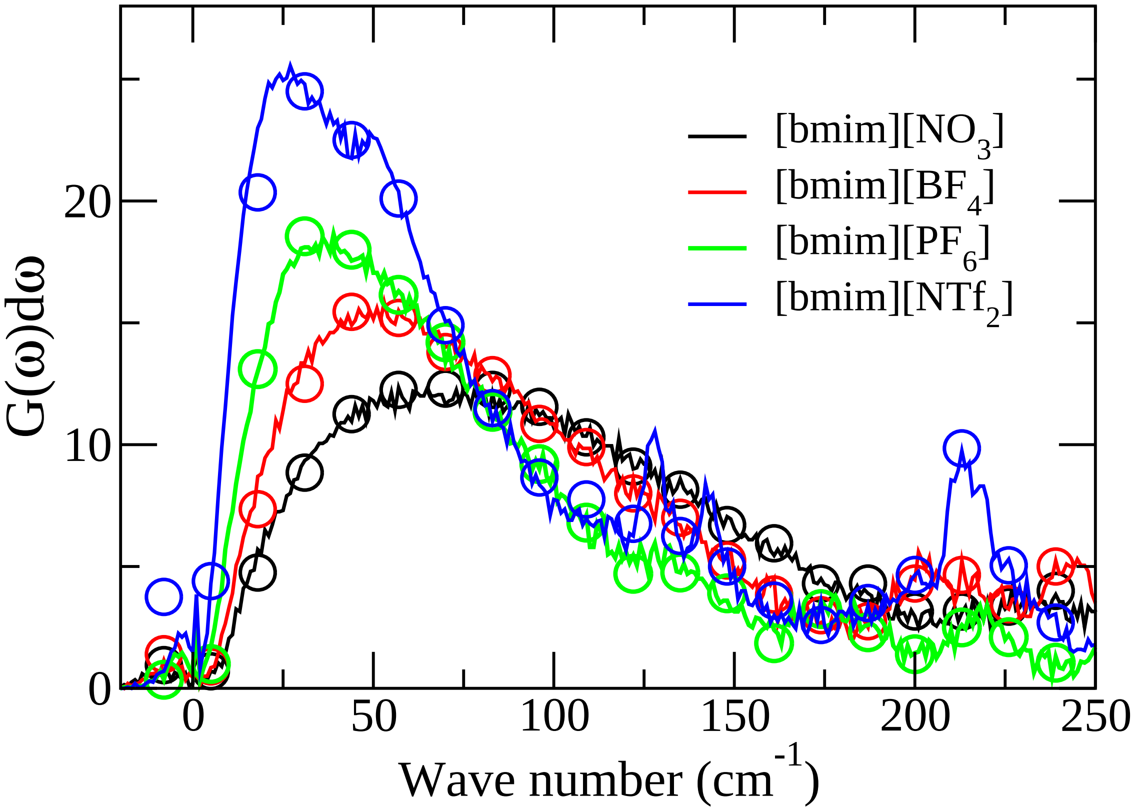

Figure 3.5: Comparison between VDOS (i) obtained with a 12 Å cutoff distance for non-bonded interactions along with the Ewald summation for the long range part of Coulomb interaction (straight lines) and (ii) obtained with a 6 Å cutoff distance for non-bonded interactions and in the absence of contribution from Ewald summation (symbols). See text for more details.

Surprisingly, these spectra nearly match those obtained with the full interaction potential. A further reduction in the interaction cutoff distance leads to significant changes in the low frequency spectra. With a 6Å cutoff for the Lennard-Jones term and a straightforward spherical cutoff for the electrostatics, the potential energy for a given liquid configuration is of course vastly different from one calculated with the complete force field. However, the spectrum of eigen values (or frequencies) are not seemingly affected, i.e., although the basin energies are changed, their curvatures do not. This demonstrates that the latter is only weakly dependent on long range interactions. *Short range interactions dominate the curvature of the potential energy surface near the minimum.* It should also be noted that the effect of changing the cutoff does not significantly alter the spectrum along the negative x-axis. Modes with imaginary frequencies do not grow much in intensity with the "revised" force field. Hence, it is safe to assume that the atoms are present in their local minima in the force field with the shorter cutoff as well.

Another quantity which describes the number of atoms participating in a mode is the participation ratio, PR, calculated using Equation 3. For localized modes such as C-H stretch, this value is found to be around 0.001. The behaviour of PR in the far infrared region is shown in Figure 3.6. The values are around 0.2 for all the ILs. When all the atoms take part in a mode, PR is unity and when only one atom is involved, the PR value is approximately $1/N$, where N is the number of atoms present in the system. The inset to the figure compares PR values for the crystalline and liquid [bmim][PF_6]. The values for the crystal are higher than that for the liquid in the far-infrared region.

The results on the participation ratio, seen in combination with those obtained from the effect of deuteration convey that modes in imidazolium based room temperature ionic liquids with frequencies less than 100 $cm^{-1}$are inter-ionic in character. Their frequencies are largely determined by the local structure (first coordination shell) and interactions arising therein. Hydrogen bonding between cations and anions can only modulate this band. It does not solely determine the position of the low frequency feature.

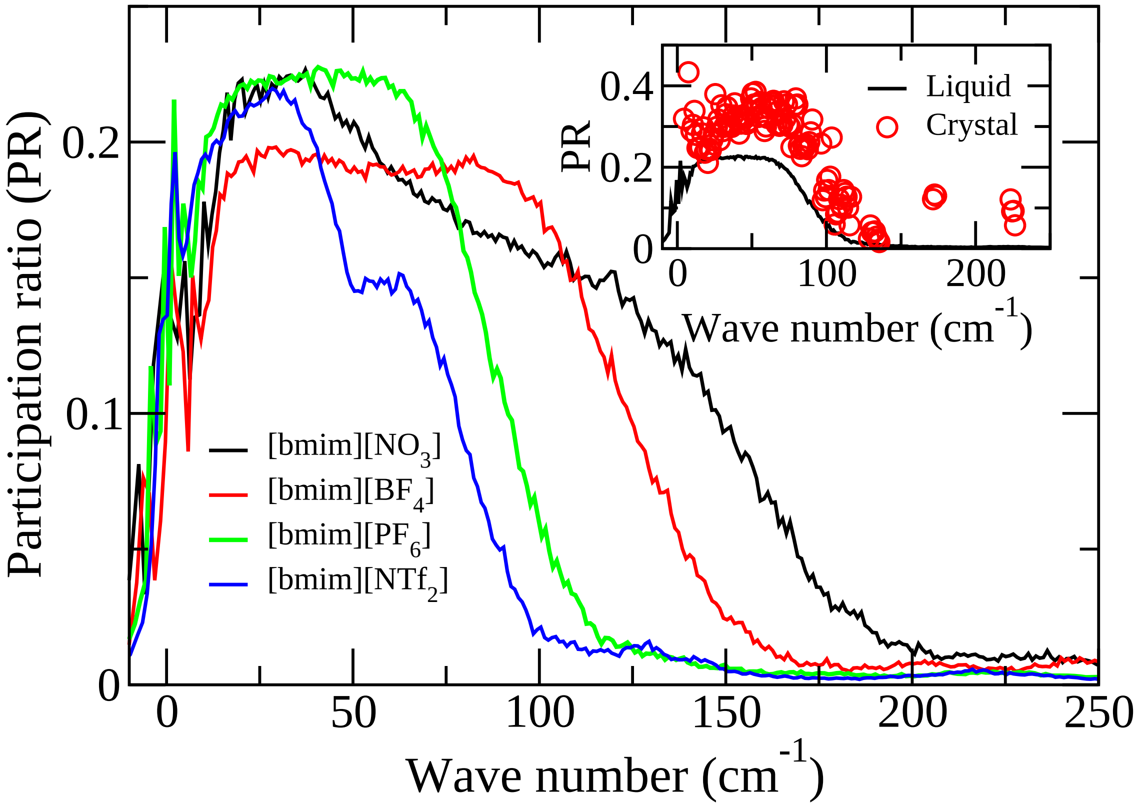

Figure 3.6: Participation ratio (PR) of modes against frequency for all the liquids. Inset: PR of liquid and crystalline [bmim][PF$_6$] using force field calculations.

3.3.2 Density functional theory based calculations

The vibrational density of states for the four liquids obtained from empirical potentials clearly show the interionic character of the modes at low frequencies. This observation is further substantiated by zero temperature Hessian calculations and density functional theory based finite temperature molecular dynamics simulations of the crystal of [bmim][PF$_6$].

The MD trajectory obtained in the latter can be used to calculate the autocorrelation function of the ion velocities whose Fourier transform is the VDOS. The VDOS obtained thus is compared to that obtained from a harmonic analysis within the DFT framework, and against results for the crystal obtained from our force field, in Figure 3.7. Also shown are the discrete frequencies obtained for an ion pair of

[bmim][PF_6] using the PBE functional.

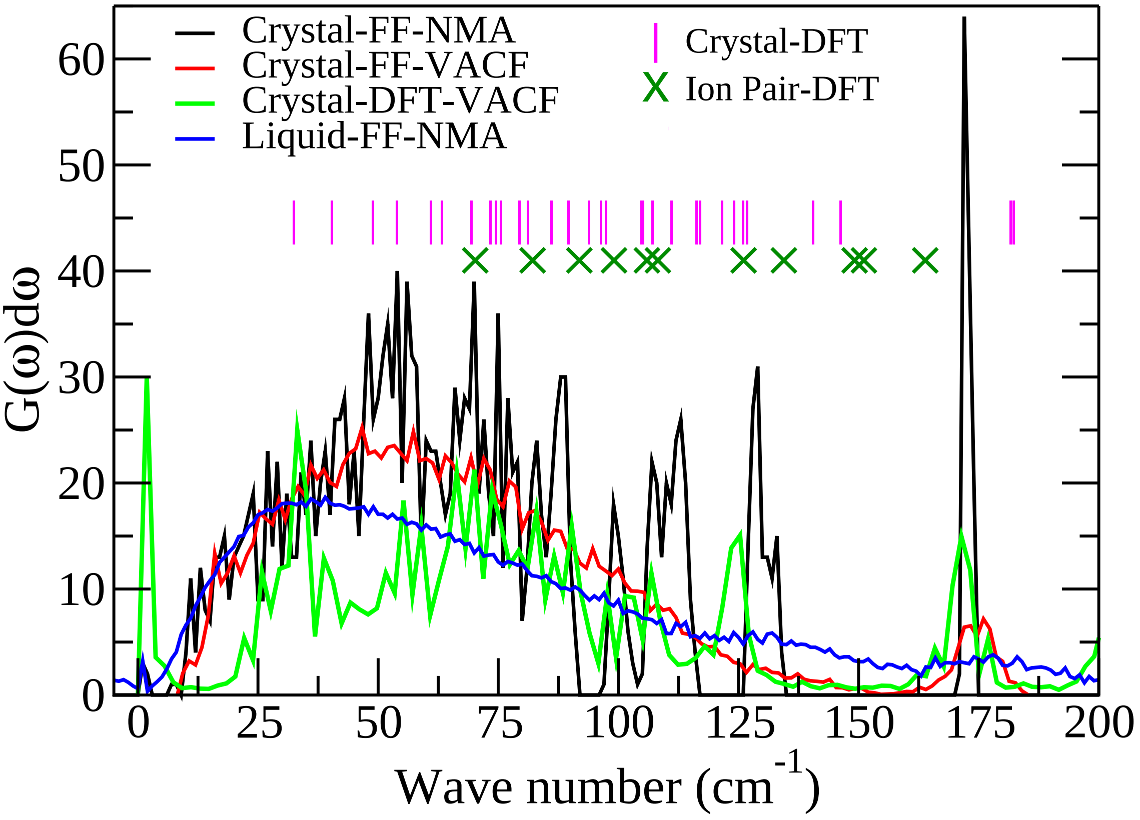

Figure 3.7: Frequency spectra of crystalline [bmim][PF_6] obtained from force field based simulations and from CPMD simulations. The liquid [bmim][PF_6] NMA spectrum is shown for comparison. Small, discrete vertical lines are values of frequencies obtained from density functional theory of the crystal within the harmonic approximation, denoted as "Crystal-DFT". Green crosses, denoted as "Ion Pair-DFT" are discrete frequencies for an isolated ion pair obtained using DFT. "FF" stands for results obtained from force field. NMA is the result within the harmonic approximation, while "VACF" stands for the power spectrum of velocity autocorrelation function obtained from the MD trajectory.

The frequencies obtained from DFT for the crystal is red shifted with respect to that for the ion pair. The density of states for the crystal, obtained from both zero temperature DFT calculations and finite temperature AIMD simulations are shifted to slightly higher frequencies when compared to those obtained from force field based calculations. However, there is qualitative agreement between all these spectra.

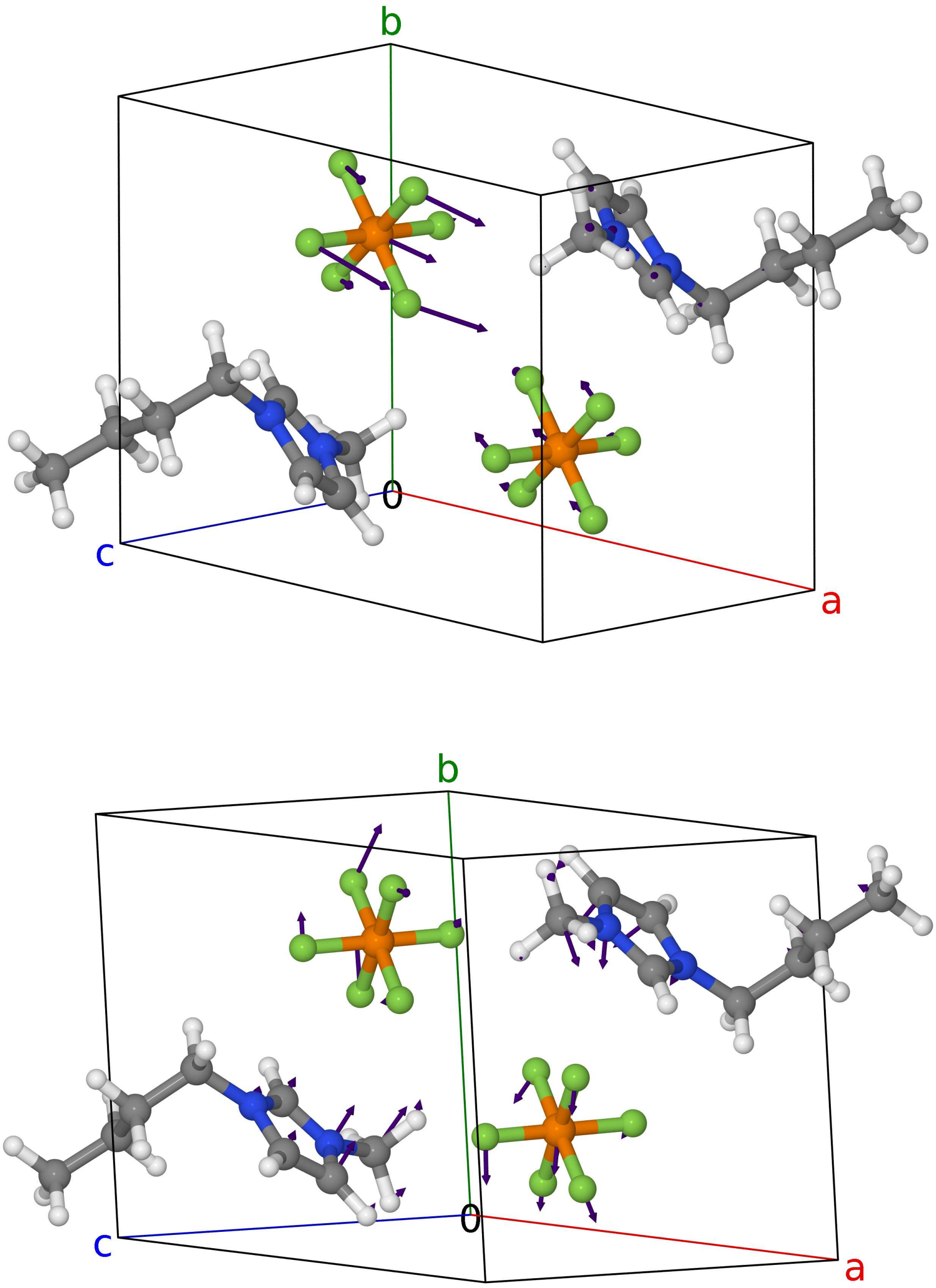

Figure 3.8: Interionic character of selected modes in crystalline [bmim][PF_6] calculated using DFT. (a) 32 cm^{-1} (b) 75 cm^{-1}. Carbon: Gray; Nitrogen: Blue; Hydrogen: White. Atomic displacement vectors are shown as black arrows.

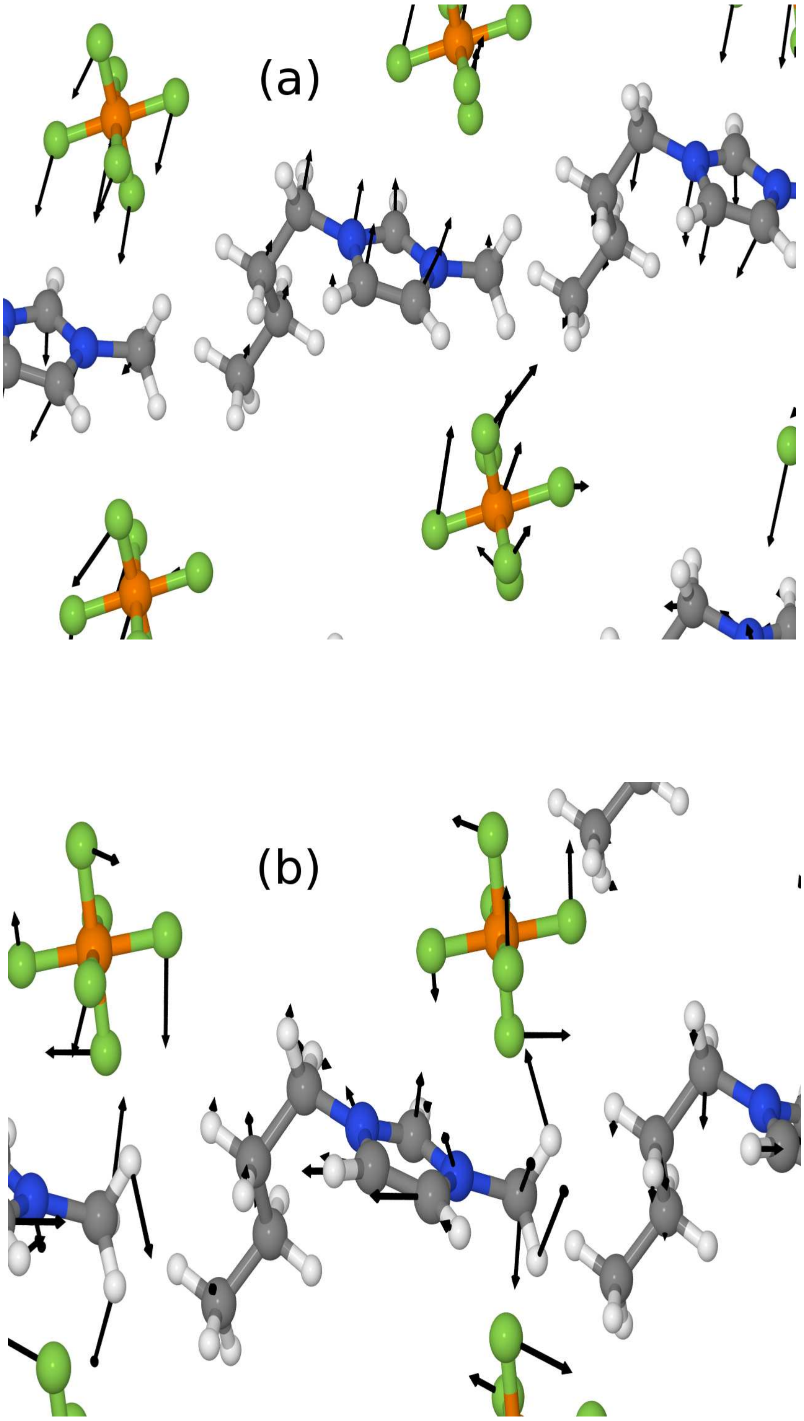

Figure 3.9: Interionic character of modes in crystalline [bmim][PF_6]calculated using force field. Only a section of the simulated crystal is shown. (a) 35.6 cm^{-1}, (b) 55.7 cm^{-1}. Carbon: Gray; Nitrogen: Blue; Hydrogen: White. Atomic displacement vectors are shown as black arrows and are scaled by a factor for better visualization.

An examination of the atomic displacements at low frequencies obtained from DFT calculations for the crystal demonstrate, once again their interionic character. These are shown in Figures 3.8 and 3.9. Another surprising finding is the overall agreement in the low frequency feature between that obtained for the liquid and for the crystal, both from force field simulations. Given that the near neighbour shell of an ion in the liquid is similar to that in the crystal [59], the similarity between the low frequency band for the two systems shows that it arises from short range interactions.

3.4 Conclusions

We have studied the far infrared region of the vibrational spectrum of room temperature ionic liquids using various computational methods. Molecular dynamics trajectories were generated for four different ionic liquids using force fields appropriate for each of these systems. The power spectra of these liquids were obtained from the velocity auto time correlation function, a standard procedure to obtain the vibrational density of states. In addition, the VDOS was obtained within the harmonic approximation, from many quenched configurations of the liquids, using a program developed in our group. The procedure not only yields the spectrum of frequencies but also the atomic displacements of the modes. The harmonically approximated VDOS closely mirrors the total density of states, even at low frequencies. This is a key observation. A distinct band is observed around 30 to 80 cm^{-1} in all the liquids. The peak position shifts to higher frequencies with an increase in the strength of the cation-anion interaction, consistent with experiments [26,29,34].

Our calculations also show that the low frequency band in the VDOS is unchanged upon deuteration of the three ring hydrogens on the imidazolium cation. Had this feature arisen from localized motions of the cation-anion hydrogen bond, a shift towards lower frequencies would have been seen. The absence of such a shift indicates the non-local character of the modes contributing to this band. The calculation of the participation ratio of each mode attests to this fact. This quantity is large for modes whose frequencies are less than 100 cm^{-1} in all the liquids studied, implying that a large number of atoms are sufficiently displaced by these modes.

The low frequency band in room temperature ionic liquids arises primarily from interionic interactions, a fact agreed upon by both the groups of Ludwig and Buffeteau. Our calculations show that the band can be nearly reproduced by short-range interactions. These conclusions are further confirmed from the density functional theory based gas phase calculations of ion pairs as well as the periodic calculations of crystalline [bmim][PF_6].

The modes contributing to the low frequency band is interionic in character; its presence has been documented even in ionic liquids which lack the capability to form ion-ion hydrogen bonds [32,34,35]. Hydrogen bonds modulate the peak frequency of this band. The visualization of the atomic displacements for these modes from the Hessian calculation for the bulk RTILs along with that of the [bmim][PF_6] crystal confirms their inter-ionic character.

Bibliography

[1] S.Tsuzuki, H. Tokuda, K. Hayamizu, M. Watanabe, *J. Phys. Chem. B*, **109**, 16474, (2005).

[2] N. R. Dhumal, H. J. Kim, J. Kiefer, *J. Phys. Chem. A*, **113**, 10397, (2009).

[3] Z. Liu, T. Chen, A. Bell, B. Smit, *J. Phys. Chem. B*, **114**, 4572., (2010).

[4] E. J. Maginn, *J. Phys. Cond. Matt.*, **21**, 373101, (2009).

[5] T. I. Morrow, E. J. Maginn, *J. Phys. Chem. B*, **106**, 12807, (2002).

[6] M. G. Del Popolo, G. A. Voth, *J. Phys. Chem. B*, **108**, 1744, (2004).

[7] Z. Hu, C. J. Margulis, *Proc. Nat. Acad. Sci. USA*, **103**, 831, (2006).

[8] Z. Hu, C. J. Margulis, *Acc. Chem. Res.*, **40**, 1097, (2007).

[9] D. Roy, N. Patel, S. Conte, M. Maroncelli, *J. Phys. Chem. B*, **114**, 8410, (2010).

[10] D. Jeong, M. Y. Choi, H. J. Kim, Y. Jung, *Phys. Chem. Chem. Phys.*, **12**, 2001, (2010).

[11] K. Yamamoto, M. Tani, M. Hangyo, *J. Phys. Chem. B*, **111**, 4854, (2007).

[12] A. Stoppa, J. Hunger, R. Buchner, G. Hefter, A. Thoman, H. Helm, *J. Phys. Chem. B*, **112**, 4854, (2008).

[13] C. Daguenet, P. J. Dyson, I. Krossing, A. Oleinikova, J. Slattery, C. Wakai, H. Weingärtner, *J. Phys. Chem. B*, **110**, 12682, (2006).

[14] D. A. Turton, J. Hunger, A. Stoppa, G. Hefter, A. Thoman, M. Walther, R. Buchner, K. Wynne, *J. Am. Chem. Soc.*, **131**, 11140, (2009).

[15] K. Nakamura, T. Shikata, *ChemPhysChem*, **11**, 285, (2010).

[16] G. Giraud, C. M. Gordon, I. R. Dunkin, K. Wynne, *J. Chem. Phys.*, **119**, 464, (2003).

[17] D. Xiao, J. R. Rajian, L. G. Jr. Hines, S. Li, R. A. Bartsch, E. L. Quitevis, *J. Phys. Chem. B*, **112**, 13316, (2008).

[18] A. Dominguez-Vidal, N. Kaun, M. J. Ayora-Canada, B. Lendl, *J. Phys. Chem. B*, **111**, 4446, (2007).

[19] A. Yokozeki, D. J. Kasprzak, M. B. Shiflett, *Phys. Chem. Chem. Phys.*, **9**, 5018, (2007).

[20] S. Tsuzuki, H. Tokuda, M. Mikami, *Phys. Chem. Chem. Phys.*, **9**, 4780, (2007).

[21] P. A. Hunt, I. R. Gould, B. Kirchner, *Aus. J. Chem.*, **60**, 9, (2007).

[22] S. Zahn, J. Thar, B. Kirchner, *J. Chem. Phys.*, **132**, 124506, (2010).

[23] V. Kempter, B. Kirchner, *J. Mol. Struct.*, **972**, 22, (2010).

[24] T. Cremer, C. Kolbeck, K. R. J. Lovelock, N. Paape, R. Wölfel, P. S. Schulz, P. Wasserscheid, H. Weber, J. Thar, B. Kirchner, F. Maier, H. Steinrück, *Chem. Eur. J.*, **16**, 9018, (2010).

[25] A. H. Pakiari, S. Siahrostami, T. Ziegler, *J. Mol. Struct.*, **955**, 47, (2010).

[26] K. Fumino, A. Wulf, R. Ludwig, *Angew. Chem. Int. Ed.*, **47**, 3830, (2008).

[27] K. Fumino, A. Wulf, R. Ludwig, *Angew. Chem. Int. Ed.*, **47**, 8731, (2008).

[28] T. Köddermann, K. Fumino, R. Ludwig, J. N. C. Lopes, A. A. H. Padua, *ChemPhysChem*, **10**, 1181, (2009).

[29] K. Fumino, A. Wulf, R. Ludwig, *Phys. Chem. Chem. Phys.*, **11**, 8790, (2009).

[30] A. Wulf, K. Fumino, R. Ludwig, *J. Phys. Chem. A*, **114**, 685, (2010).

[31] A. Wulf, K. Fumino, R. Ludwig, P. F. Taday, *ChemPhysChem*, **11**, 349, (2010).

[32] A. Wulf, K. Fumino, R. Ludwig, *Angew. Chem. Int. Ed.*, **49**, 449, (2010).

[33] Y. Danten, M. I. Cabaco, M. Besnard, *J. Phys. Chem. A*, **113**, 2873, (2009).

[34] T. Buffeteau, J. Grondin, Y. Danten, J. Lassegues, *J. Phys. Chem. B*, **114**, 7587, (2010).

[35] J. Grondin, J. Lassegues, D. Cavagnat, T. Buffeteau, P. Johansson, R. Holomb, *J. Raman Spectrosc.*, (2010), DOI 10.1002/jrs.2754.

[36] S. S. Sarangi, W. Zhao, F. Müller-Plathe, S. Balasubramanian, *ChemPhysChem*, **11**, 2001, (2010).

[37] B. L. Bhargava, S. Balasubramanian, *J. Chem. Phys.*, **127**, 114510, (2007).

[38] Z. Liu, S. Huang, W. Wang, *J. Phys. Chem. B*, **108**, 12978, (2004).

[39] T. Köddermann, D. Paschek, R. Ludwig, *ChemPhysChem*, **8**, 2464, (2007).

[40] J. N. C. Lopes, J. Deschamps, A. A. H. Padua, *J. Phys. Chem. B*, **108**, 2038, (2004).

[41] A. R. Choudhury, N. Winterton, A. Steiner, A. I. Cooper, K. A. Johnson, *J. Am. Chem. Soc.*, **127**, 16792, (2005).

[42] S. M. Dibrov, J. K. Kochi, *Acta. Cryst.*, **C62**, o19, (2006).

[43] S. J. Plimpton, *J. Comp. Phys.*, **117**, 1, (1995).

[44] R. W. Hockney, J. W. Eastwood, *Computer Simulation Using Particles*, **2nd ed.** IOP, (1988).

[45] M. Krishnan, S. Balasubramanian, *Phys. Rev. B*, **68**, 064304, (2003).

[46] M. Cho, G. R. Fleming, S. Saito, I. Ohmine, R. M. Stratt, *J. Chem. Phys.*, **100**, 6672, (1994).

[47] T. Wu, S. Tsay, *J. Chem. Phys.*, **105**, 9281, (1996).

[48] S. D. Bembenek, B. B. Laird, *J. Chem. Phys.*, **114**, 2340, (2001).

[49] M. Krishnan, S. Balasubramanian, *J. Phys. Chem. B*, **109**, 1936, (2005).

[50] J. Hutter, J. P. Ballone, M. Bernasconi, P. Focher, E. Fois, S. Goedecker, D. Marx, M. Parrinello, M. E. Tuckerman, CPMD Version 3.11.1, Max Planck Institut fuer Festkoerperforschung, Stuttgart, and IBM Zurich Research Laboratory, 1990-. Version 3.13.2

[51] J. P. Perdew, K. Burke, M. Ernzerhof, *Phys. Rev. Lett.*, **77**, 3865, (1996).

[52] R. W. Hockney, *Meth. Comput. Phys.*, **9**, 136, (1970).

[53] N. Troullier, J. L. Martins, *Phys. Rev. B*, **43**, 1993, (1991).

[54] H. J. Monkhorst, J. D. Pack, *Phys. Rev. B*, **13**, 5188, (1976).

[55] R. Car, M. Parrinello, *Phys. Rev. Lett.*, **55**, 2471, (1985).

[56] G. J. Martyna, M. L. Klein, M. Tuckerman, *J. Chem. Phys.*, **97**, 2635, (1992).

[57] Jmol:An open-source Java viewer for chemical structures in 3D. http://www.jmol.org/

[58] B. McMahon, R. M. Hanson, *J. Appl. Crystallogr.*, **41**, 811, (2008).

[59] H, V. R. Annapureddy, H. K. Kashyap, P. M. De Biase, C. J. Margulis, *J. Phys. Chem. B*, DOI: 10.1021/jp108545z.

Chapter 4

Molecular Dynamics Simulations of Ionic Liquid-Vapour Interfaces: Effect of Cation Symmetry on Structure at the Interface

4.1 Introduction

The interface of ionic liquids is an important component as it can be used to understand electron transfer in catalytic reactions [1], wetting phenomena of ionic surfaces [2], double-layer effects at molten salt interfaces [3], and many other interfacial reactions. In a recent study, Iwahashi *et al* have conducted ultraviolet photoemission spectroscopy and metastable atom electron spectroscopy on a series of ILs and showed that both cations and anions are present at the surface of ILs with shorter alkyl chains and that the surface is covered with the alkyl groups in ILs with longer alkyl chains [4]. They concluded that the non-polar groups point towards the vacuum side and the polar groups face towards the bulk side forming a double layered structure at the interface. Very recently, Baldelli and co-workers have reported results of SFG, surface potential, and surface tension experiments on a group of ILs consisting of [C_4C_1im] cations and have proposed a model for the arrangement of ions at the IL-vapour interface [5]. In this model, both cations and anions are present on the surface, however the anions are located at a slightly lower plane than the cations. They conclude that the surface had contributions from both van der Waals and Coulombic interactions indicating the presence of alkyl chains as well as of ions at the interface.

Lynden-Bell *et al* have carried out several simulations studying the interfacial properties of many ILs [6–10]. Following the x-ray reflectivity measurements of Deutsch *et al* [11], MD simulations of the ionic liquid-vapour interface of 1-alkyl-3-methyl imidazolium hexafluorophosphate were carried out [12]. These simulations confirmed the enhancement in the electron density near the surface as was earlier seen in the experiment. Later, few differences in the experimental and simulation results on the electron density profile were reconciled [13]. Many other simulation studies too have examined the nature of the IL-vapour interface and have affirmed the oscillatory behaviour of ion density profiles [14–16].

All the above mentioned works were carried out on imidazolium cation based ionic liquids having asymmetric alkyl group substitutions on the two nitrogen atoms of the imidazolium ring. Recent studies on the phase behavior of symmetric cations (in which the length of these alkyl groups are identical) showed that they too can be liquids at or near ambient conditions [17]. The structure, dynamics, and morphology of this category of ionic liquids has attracted some attention recently [18–20]. Symmetric, [$C_nC_n$im] cation based ILs are generally more structured and more viscous than asymmetric [$C_nC_1$im] cation based ILs. The presence of two alkyl groups in the former enhances the van der Waals (vdW) interactions relative to Coulomb, leading to greater nanostructural order.

In the present work, the effect of molecular (specifically, the cation) symmetry on the structure of the ionic liquid-vapour interface has been studied. An attempt has been made to examine the impact of enhanced vdW interactions (due to the presence of a cation with two equivalent alkyl groups) on the interfacial structure and properties, while retaining the strength of the electrostatic interaction. Hence this study probes the influence of molecular symmetry as well as the effect of enhanced van der Waals interactions on the interfacial properties of RTILs. These twin goals have been attained by symmetrizing the alkyl group substitutions on the imidazolium ring. Traditional imidazolium based IL salts possess a methyl group at the 3-position and a generic alkyl group at the 1-position of the ring. In the current article, ionic liquids which have equivalent alkyl substitutions on both these positions have been investigated. The next section details the procedures of the simulation, which is followed by the presentation and discussion of the results. Anticipating the results, significant differences in the interfacial structures as well as properties between ionic liquids which have symmetric and asymmetric cations were found.

4.2 Details of Simulation and Methodology

Classical MD simulations have been carried out on four different ionic liquids. The anion in each of the liquid is bis(trifluoromethylsulfonyl)imide (NTf_2). Cations were of the form, 1-R-3-R'-imidazolium (where R and R' are two alkyl groups) (denoted later as C_nC_m). The systems studied were: 'Asymmetric' ILs – $[C_3C_1][NTf_2]$, and $[C_5C_1][NTf_2]$, and 'symmetric' ILs – $[C_3C_3][NTf_2]$, and $[C_5C_5][NTf_2]$. Figure 4.1 depicts the schematic pictures of the ions studied. In each case, the system consisted of 1,000 ion pairs with the number of atoms ranging from 37,000 to 55,000. The simulations were carried out in the constant NVT ensemble at a temperature of 300 K using Nosé-Hoover thermostats.

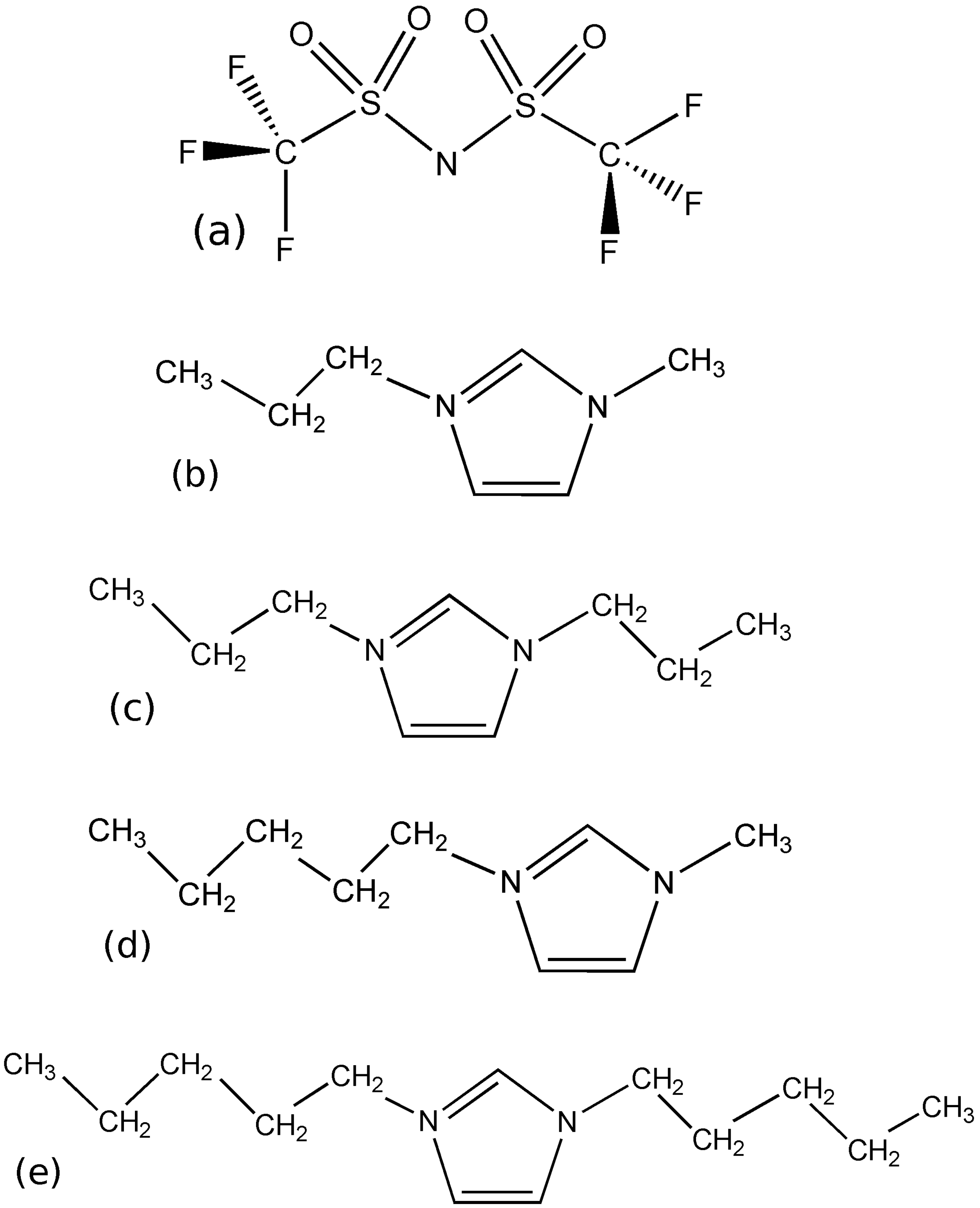

Figure 4.1: Schematic pictures of the ions. (a) bis(trifluoromethylsulfonyl)imide, (b) 1-propyl-3-methylimidazolium, (c) 1,3-dipropylimidazolium, (d) 1-pentyl-3-methylimidazolium, (e) 1,3-dipentylimidazolium

Well equilibrated liquids in three-dimensionally periodic cubic simulation boxes were taken from a previous work on these ILs in bulk [20]. The box length in the z-direction was changed to 150 Å in order to create two liquid-vapour interfaces. A liquid slab whose thickness was around 80 Å was thus created. The LAMMPS program [21] was employed to carry out the simulations. Fully flexible force field parameters were taken from the all-atom model developed by Ludwig and co-workers [22], and polarization effects were not included in this model. The potential includes intramolecular interactions (stretching, bending, dihedral, improper terms) and non-bonded Lennard-Jones and Coulombic terms. A real space cutoff distance of 12 Å was applied for the non-bonded interactions. Three-dimensional particle-particle particle-mesh (PPPM) [23] method with an accuracy of 1×10^{-5} was employed to carry out the lattice sum of the long range Coulombic interactions. The box lengths in the lateral directions for the $[C_3C_1][NTf_2]$, $[C_5C_1][NTf_2]$, $[C_3C_3][NTf_2]$, and $[C_5C_5][NTf_2]$ systems were 77.3232 Å, 80.3526 Å, 80.4282 Å, and 85.883 Å respectively. The surface normal was along the z-direction.

The equations of motion were integrated with a time step of 0.5 fs using the velocity Verlet algorithm. Long range corrections to the potential energy and pressure were applied. The systems were equilibrated for a period of 10 ns, after which trajectories of 6 ns duration were generated. In the analysis phase, coordinates were stored at an interval of 5 ps and the pressure components at an interval of 0.5 ps. For each IL, three independent trajectories were generated, starting from different configurations of the bulk liquid. Results have been averaged over these three trajectories, as well as over the two interfaces present in each system. Various density profiles have been obtained with a bin width of 1.0 Å in the z-direction. In these plots, z=0 represents the z-coordinate of the centre of mass of the system.

4.3 Results and Discussions

4.3.1 Number Densities

The mass density profile of the liquid slabs are presented in Figure 4.2. Bulk densities of these ILs obtained from a recent constant pressure-constant temperature simulations agreed with experimental values [20]. The density of liquids in the bulk region obtained from the current interface calculations are consistent with these earlier observations. Mean densities obtained in a thin slab of width 10 Å from the centre of mass of the systems are (in units of g/cm^3): 1.44 (1.47), 1.37 (1.38), 1.37 (1.39), and 1.26 (1.29) for [C_3C_1][NTf_2], [C_3C_3][NTf_2], [C_5C_1][NTf_2] and [C_5C_5][NTf_2] respectively. The values in parentheses are experimental data of Quitevis [24].

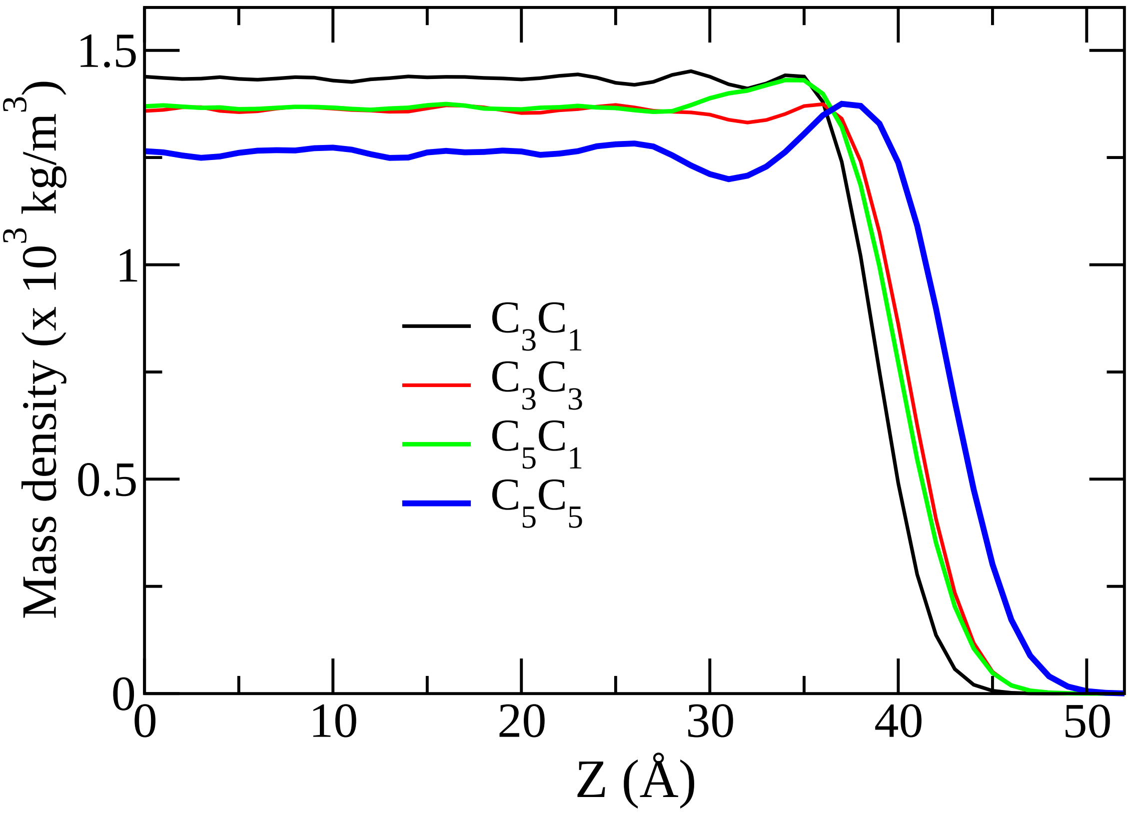

Figure 4.2: Mass density profiles of all the systems along the surface normal direction.

The bulk density values obtained in these interface calculations are about 2% smaller than the values obtained through bulk NPT simulations [20]. This is because the bulk simulations contained long range corrections to pressure, which is lacking in the interface simulations. This contribution (which is generally attractive) increases the density. Thus the slightly smaller bulk density values obtained here can be rationalized.

The density profiles exhibit weak oscillations near the interface. There exists a narrow region at the interface where the density is larger than the bulk value. The ratio of the density maximum at the interface to its bulk value is highest for the [C_5C_5][NTf_2] system. The ratio for the [C_5C_1][NTf_2] liquid is higher than that for [C_3C_3][NTf_2] although both have identical number of carbon atoms in alkyl groups. The interfacial density oscillations thus appear to be crucially dependent on the length of the larger alkyl group of the cation. Longer alkyl groups are likely to be more organized at the liquid-vapour interface thus enhancing vdW interactions. Since the positive charge on the cation resides largely on the imidazolium ring, the ordering of alkyl groups may also enable the efficient packing (see later, the scaled number density profiles of cations and anions) of the anions and cation rings at the interface.

To explore the structures at the interface, the number densities of different entities in the liquid have been calculated. The interfacial behaviour greatly depends on the specifics of the anion and the length of the alkyl chains of the cation as confirmed from simulations [10,25] as well as from experiments [26–28]. For the cation, the number densities of the geometric centre of the ring (denoted as cation in the figure) and the terminal carbon atoms on each of the alkyl groups (attached to the two nitrogens) and for the anion, that of its centre of mass of have been obtained. Figure 4.3 shows the number density profiles for all the systems along the surface normal direction. The number density profiles for the alkyl chains of symmetric systems have been divided by a factor of two, for ease of comparison with the data for asymmetric ILs.

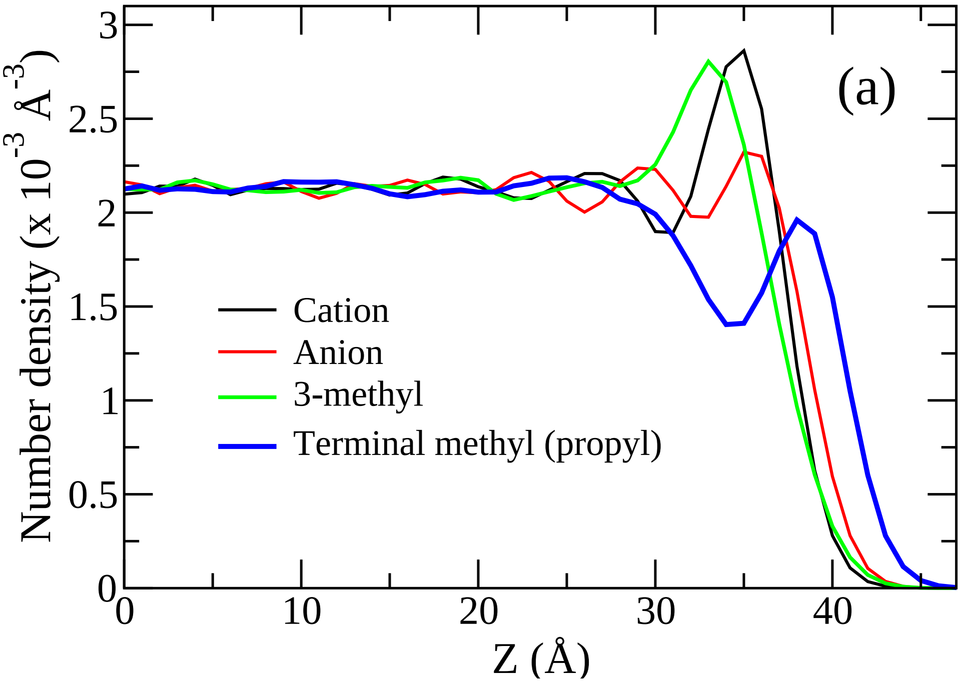

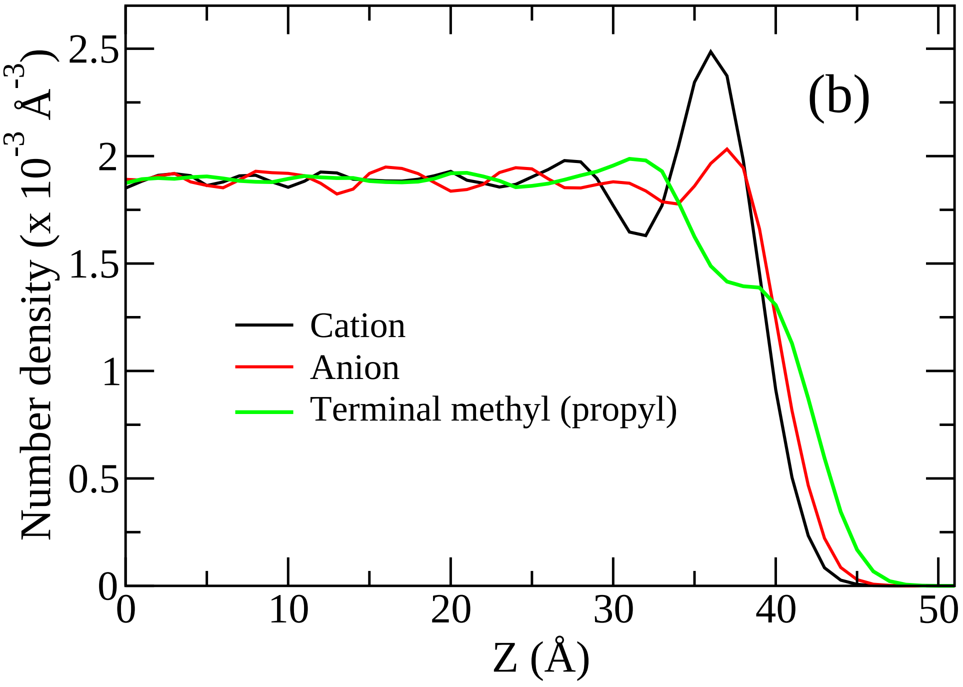

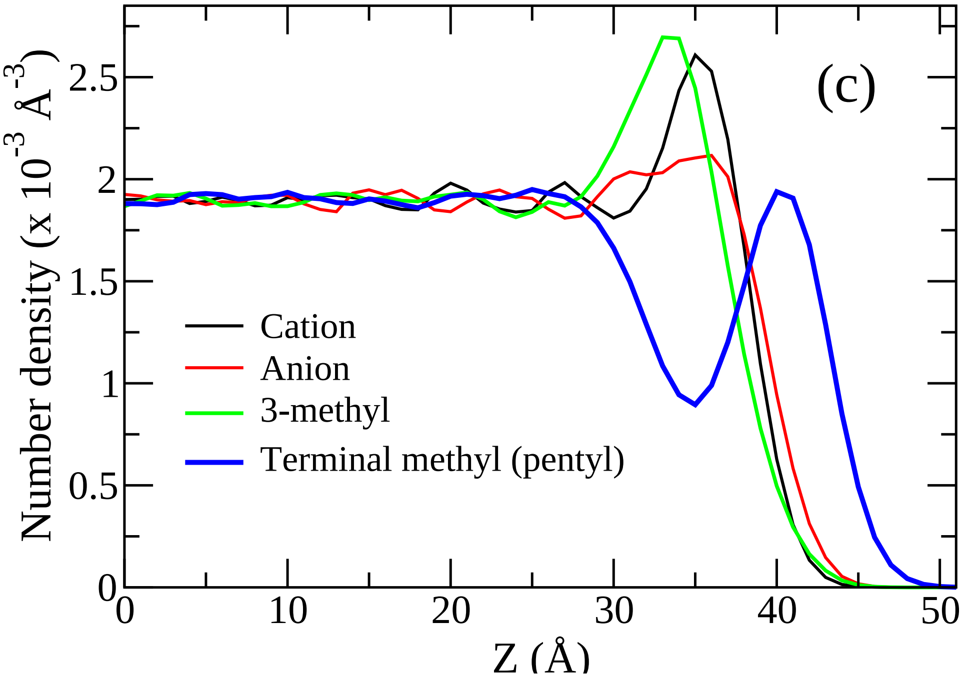

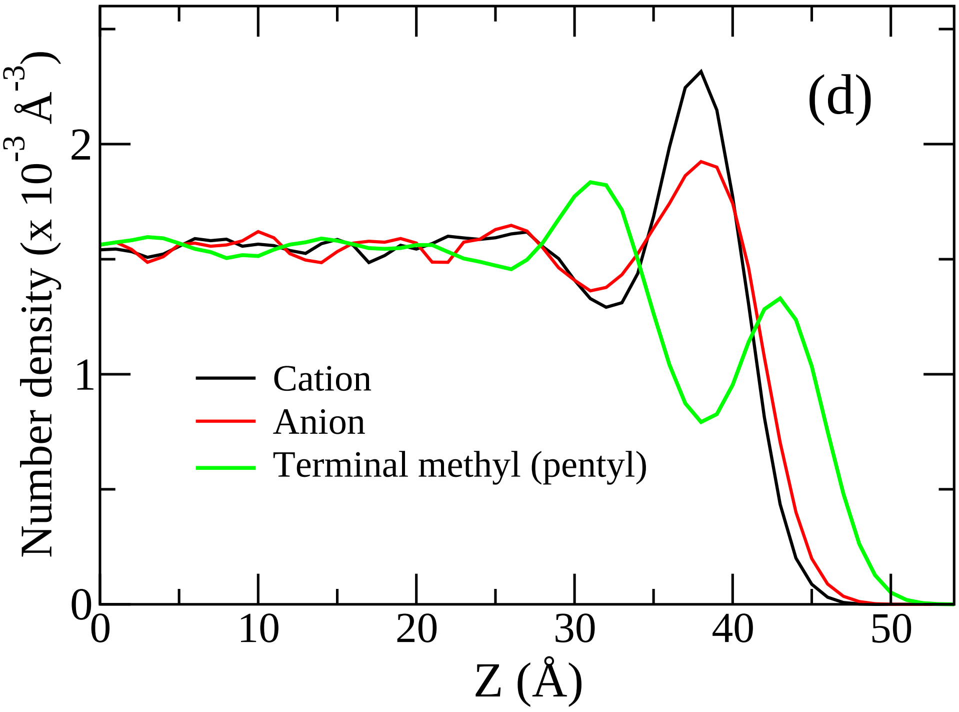

Figure 4.3: Number density profiles in (a) [C_3C_1][NTf_2] (b) [C_3C_3][NTf_2] (c) [C_5C_1][NTf_2] (d) [C_5C_5][NTf_2]. Profiles for the terminal methyl group of alkyl chains in symmetric ILs (i.e., in panels (b) and (d)) have been divided by a factor of two for ease of comparison.

The density profiles of the alkyl groups extend more into the vapour phase in ILs with longer chains. Both cations and anions are present at the surface, but the extent to which anions are exposed to the vacuum is marginally higher than that for the cation rings in all the four ILs. In asymmetric ILs, the methyl group occupies the innermost position and the alkyl chains are the outermost ones. In symmetric ILs, the alkyl groups lie on the outermost part of the interface, as expected. Noticeable long-range oscillations are observed in the number density profiles for all the systems, in agreement with earlier reports on other planar and non-planar IL-vapour interfaces [6–9, 12, 14, 29, 30]. The magnitude and range of these oscillations increases with the length of the alkyl group. At the interface, the cation density has a sharp and distinct peak while the oscillations in the anion density profile are weaker and broader. The interfacial segregation of polar (ring centre of cation and anion) and non-polar groups (alkyl chains) can be seen from these number density profiles; deep minima found in the profiles for the alkyl chain (attached to N1) are correlated with maxima in the densities of ring centre and anions.

An interesting behavior is seen in the profiles of the methyl groups among these four ILs. It must be kept in mind that in the symmetric systems, the profile for the terminal methyl has been divided by a factor of two for ease of visualization. In Figure 4.3, one observes that the profile for the terminal methyl of the 1-alkyl group in every IL exhibits a deep first minimum except for the case of the $[C_3C_3][NTf_2]$ compound (panel (b)). This apparent difference can be rationalized if one plots the density profile of the methyl group (irrespective of its position) in each IL (i.e., the sum of the profiles of the methyls belonging to the two alkyl groups attached to the nitrogens of the imidazolium ring). Such a plot is presented in Figure 4.4.

One finds that the deep minimum present in the profiles of $[C_3C_1][NTf_2]$ and the $[C_5C_1][NTf_2]$ systems (Figure 4.3) have transformed into a shallow shoulder in the total methyl profiles.

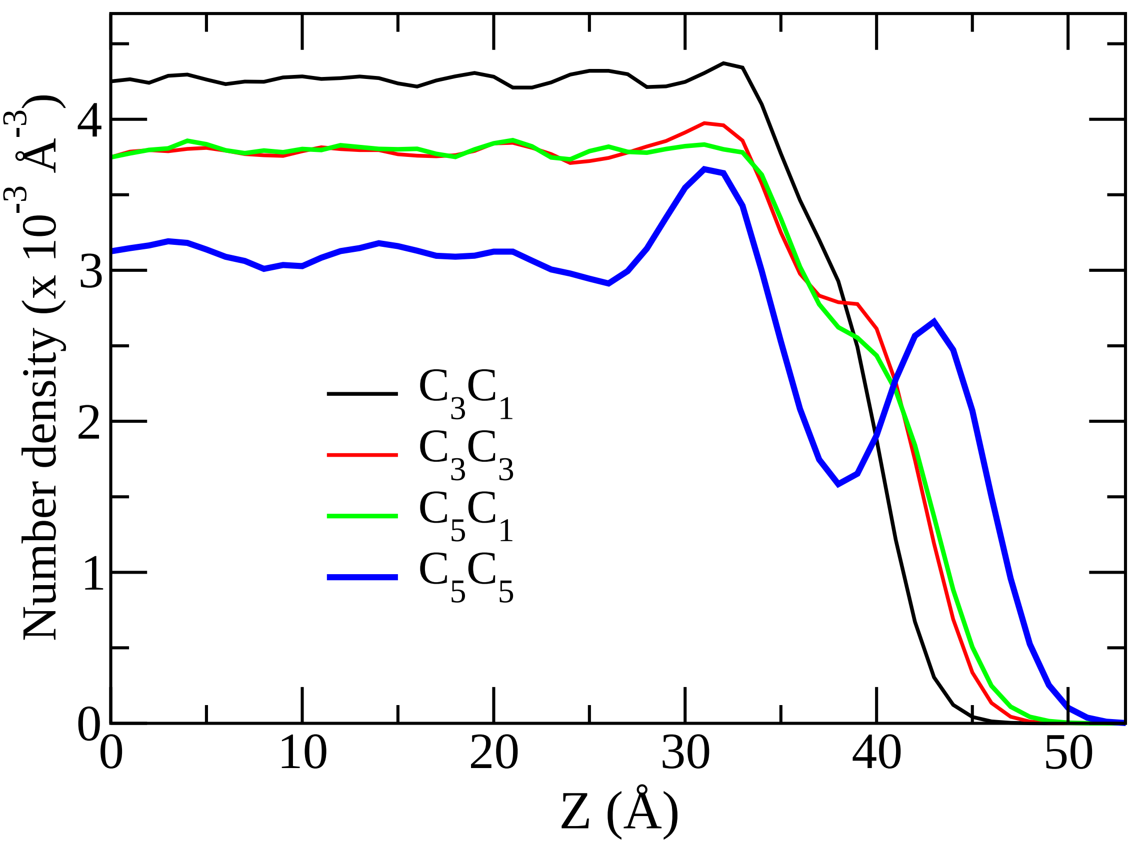

Figure 4.4: Number density profile of methyl groups along the surface normal direction.

Obviously, the additional substantial contribution at this location has come from the peak present in the number density of the 3-methyl group (see Figure 4.3(a) for example). Hence in terms of the total density of methyl groups, the [C_3C_3][NTf_2] system is similar in behaviour to [C_5C_1][NTf_2] and [C_3C_1][NTf_2] ILs. However, the [C_5C_5][NTf_2] IL exhibits a deep minimum in the total methyl density profile as well. It can be predicted that ILs with short chains (propyl or shorter) may not exhibit a deep minimum in the density profile of methyl group. With increase in the length of the alkyl group, the minimum in the number density profile of the longer alkyl group deepens. Note also the presence of two strong peaks in the total methyl density profile for the [C_5C_5][NTf_2] system (Figure 4.4) at 31.3 Å and 43.1 Å respectively. These correspond to the two terminal methyl groups of the pentyl chains. The total methyl density profiles can be better compared between these interfaces, if one scales the values by the respective methyl density values in the bulk region. Such a 'scaled' plot is shown in Figure 4.5.

Although the [C_3C_1][NTf_2] liquid had the highest interfacial total methyl density in absolute scale, one finds that this is likely due to its comparatively larger bulk density. Normalizing for this effect among the four liquids studied, it can be observed that indeed the [C_5C_5][NTf_2] liquid exhibits quite large values of scaled methyl density at the interface. This demonstrates the dominant role played by the length of the alkyl group in determining the relative density at the interface when compared to bulk.

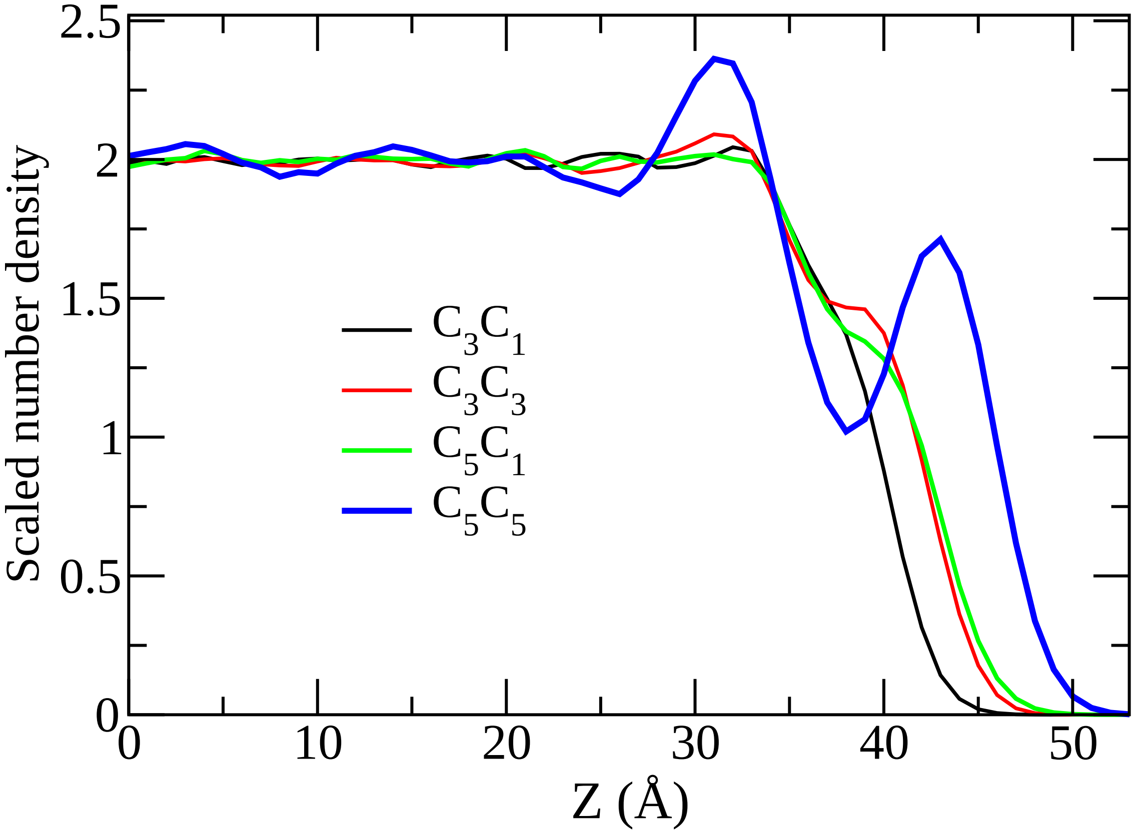

Figure 4.5: Scaled number density profile of methyl groups along the surface normal direction.

Figure 4.6 compares the number density profiles of cation among the four ILs.

Interfacial density is highest for the [C_3C_1][NTf_2] cation and decreases with increasing chain length. This observation is in line with the findings of Slattery and co-workers [26, 31]. They carried out studies on the scattering dynamics of hyperthermal oxygen atoms from IL surfaces on [C_2C_1][NTf_2] and [C_2C_{12}][NTf_2 systems and inferred that [C_{12}mim][NTf_2] is more reactive than [C_2mim][NTf_2] due to the relative rigidity of the latter.

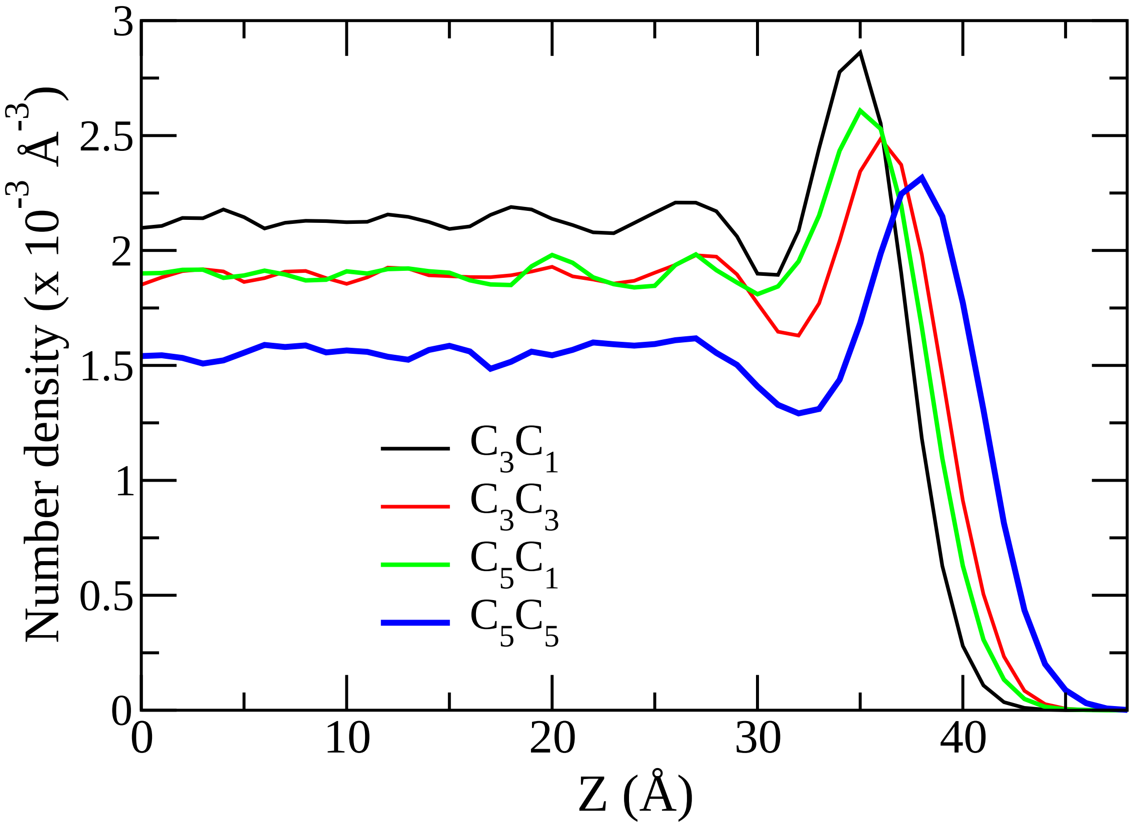

Figure 4.6: Cation number density profiles along the surface normal direction.

From Figure 4.6, it is clear that the interfacial cation number density for the [C_5C_1][NTf_2]system is higher than that for its symmetric isomer, [C_3C_3][NTf_2]. Asymmetric cations allow for better packing of the rings at the interface. The thickness of the liquid slab for symmetric systems is slightly larger due to the reduced bulk number density. A comparison of the profiles for [C_3C_3][NTf_2] and [C_5C_1][NTf_2] in Figure 4.6 reveals this aspect. These two systems have the same mass (isomers).

It can be seen that the profile for [C_3C_3][NTf_2] is more extended towards the vacuum than that for [C_5C_1][NTf_2]. Their bulk densities are comparable; however, [C_5C_1][NTf_2] exhibits a taller peak at the interface for the cation number density. Thus, asymmetric systems have marginally higher cation density at the interface than their isomeric symmetric ILs.

Differences in the ring density profile of these four ionic liquids can arise due to variations in packing efficiency at the interface and/or due to differences in their respective bulk densities. In order to identify the contribution from the former, each of the cation ring number density profiles has been scaled by the corresponding number densities in the bulk region. Such a plot is exhibited in Figure 4.7.

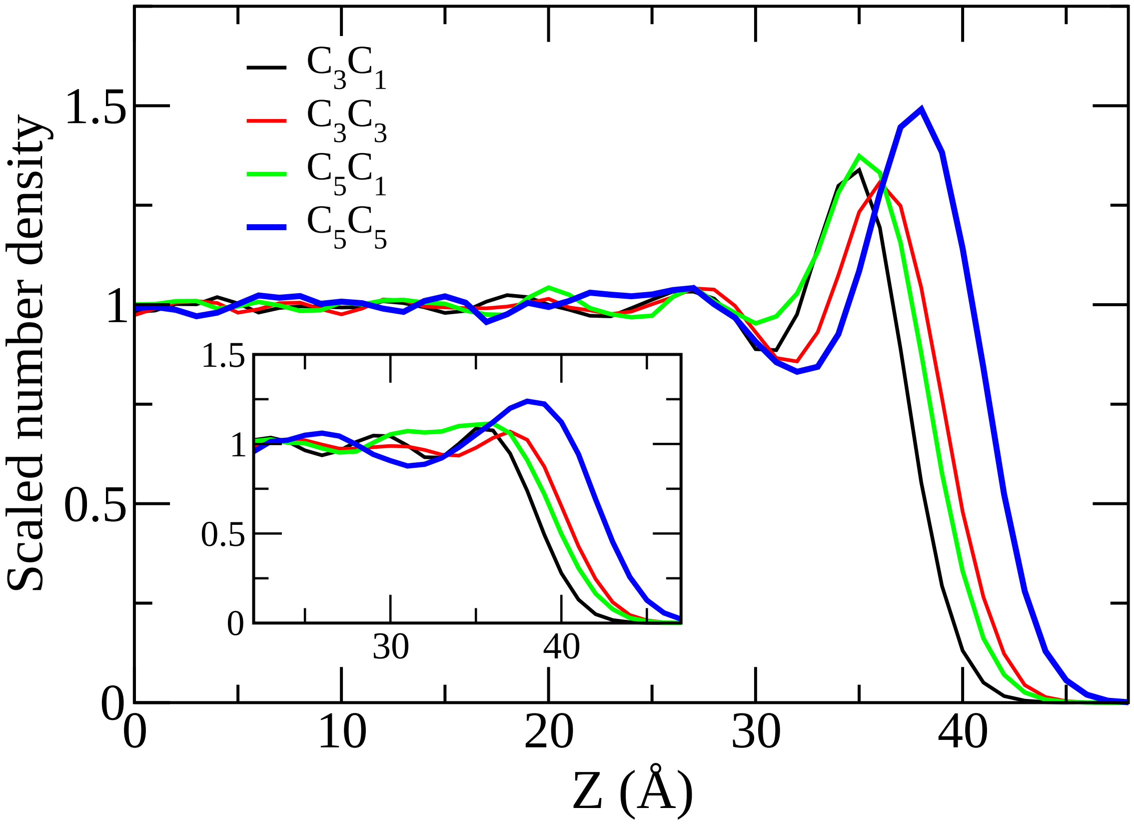

Figure 4.7: Scaled cation number density profiles of all liquids along the surface normal direction. Inset: Corresponding data for anions.

In this representation, the dominant density oscillations of the $[C_5C_5][NTf_2]$ system are clearly seen. Layering of the imidazolium ring leads to its high (relative) density at the interface. This effect permeates into the liquid giving rise to three to four oscillations in the profile. The length of the alkyl group necessarily determines the amplitude and range of these oscillations. ILs having a pentyl chain exhibit such strong characteristics as opposed to those with one (or two) propyl chain(s). The inset to this figure shows a similar plot for the scaled anion number density. An important observation here is the nearly flat profile of the anion density for the $[C_5C_1][NTf_2]$ system at the interface. The minimum of the first peak (at the interface) that is present in all the other liquids is absent in the $[C_5C_1][NTf_2]$ liquid, possibly due to the longer length of the alkyl chain.

4.3.2 Orientation

An understanding of the orientation of the cation at the IL-vapour interface is important. The angles between the surface normal vector (z-axis) and various vectors characterizing the orientation of the cations, such as; (i) the vector normal to the imidazolium ring plane (ring-normal), (ii) the vector joining the first nitrogen atom (N1) and the terminal carbon atom of the alkyl group (chain), and (iii) the vector passing through the two nitrogen atoms of the ring (NN), defined as the coordinate of the nitrogen attached to the methyl group minus that attached to the alkyl group, have been calculated. For the symmetric systems, the angle for the chain vectors are averaged over those made by the two identical alkyl chains.

Molecules that are present with magnitudes of z-coordinate larger than the first minimum in the number density profile are defined as "belonging" to the interface. Figure 4.8 shows the probability distribution of the cosine of the angle made by the ring normal, chain, and the NN vector with the z-axis for all the liquids.

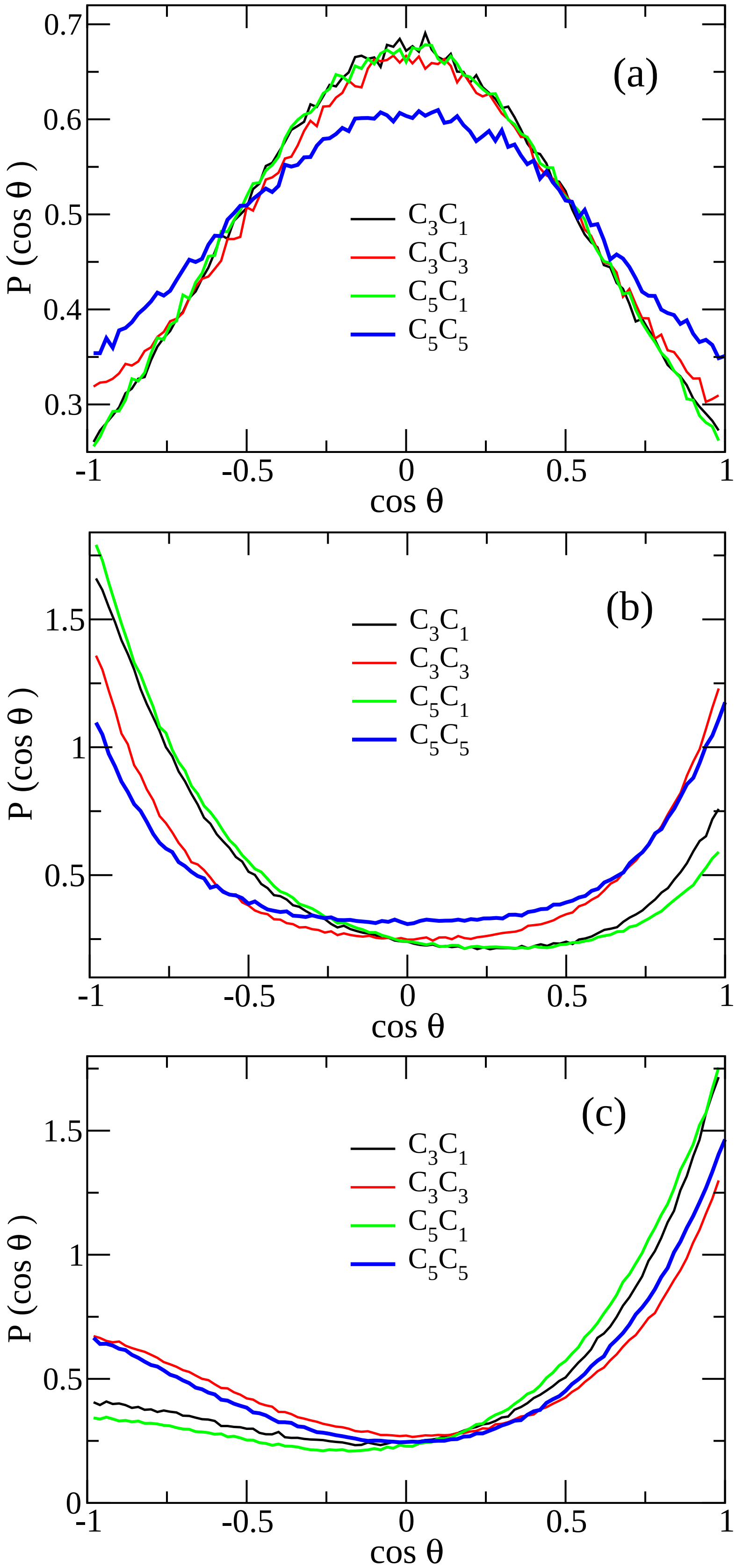

Figure 4.8: Probability distribution of cosine of the angle between the surface normal vector and (a) ring-normal vector (b) NN vector (c) alkyl chain vector.

Although the distributions are not narrow, the most probable orientation for the ring normal is perpendicular to the surface normal, the NN vector prefers to be parallel to the surface normal and the alkyl chain vector (NC) too is parallel to the surface normal. *These orientational preferences decrease for the symmetric cation.* This observation actually explains the difference between the cation number density profiles among symmetric and asymmetric systems. Lynden-Bell [6] had earlier explained that the ring normal being perpendicular to the surface normal and the alkyl chain vector being parallel to it increases the packing at the interface and hence the number density. Extending this argument, it is noted that when the cation is symmetrized, preferential orientations of the rings and of the alkyl chains decrease at the interface; the packing efficiency too decreases leading to a reduction in the number density at the interface compared to the corresponding asymmetric system.

In symmetric ILs, for a cation whose alkyl chain projects out into the vapour phase, the second alkyl group needs to be oriented in the opposite direction, i.e., into the liquid phase. Shown in Figure 4.9 are the probability distributions for the angle made by the NC vector of an alkyl group with the surface normal, provided the other NC vector is nearly parallel to the surface normal (in practice, it was demanded that cosθ values be greater than 0.8).

It is noticed that this conditional probability clearly favours a NC orientation anti-parallel to the surface normal for the case of [C_3C_3][NTf_2]. This is necessitated due to the geometry of the imidazolium cation. The presence of such a hydrophobic alkyl group in a region rich in polar interactions between the ring and the anion is energetically unfavourable. Hence the overall propensity of alkyl chains to orient themselves in a direction parallel to the surface normal is lesser for symmetric ILs when compared to asymmetric ILs. In the case of [C_5C_5][NTf_2], the second alkyl group prefers either to be parallel or anti-parallel to the surface normal. The parallel

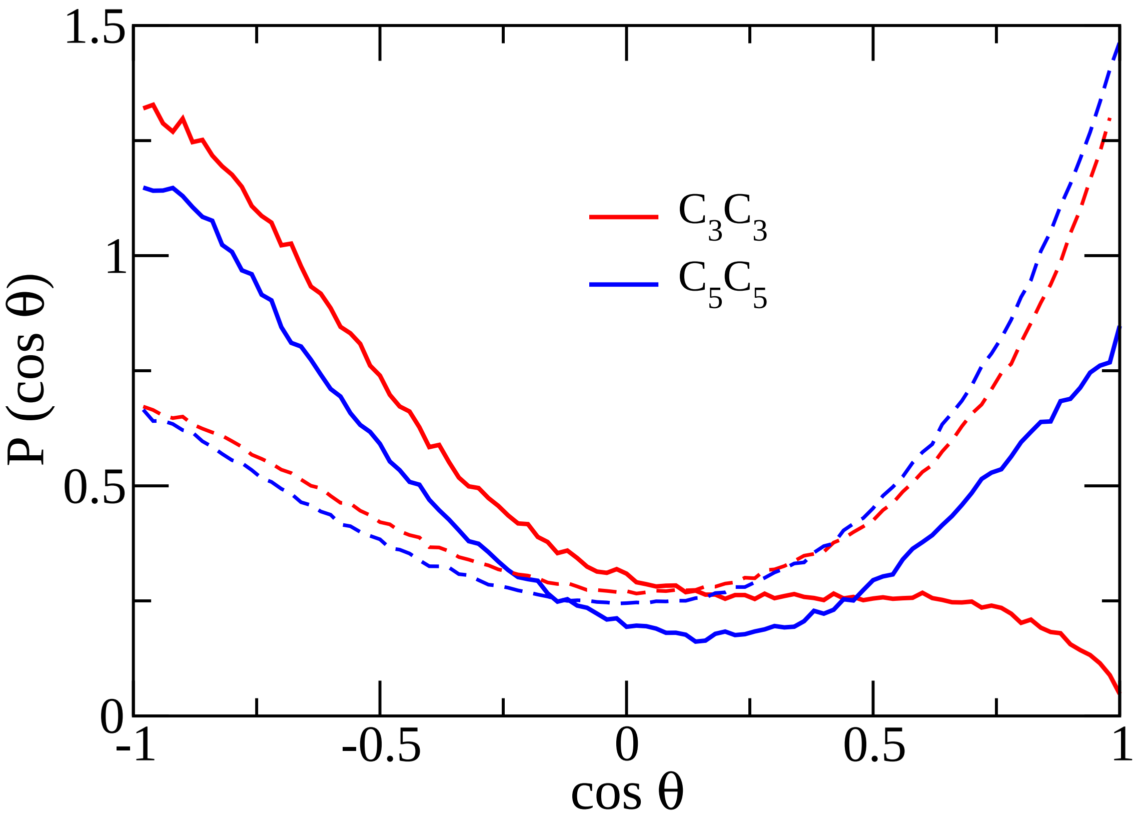

Figure 4.9: Probability distribution of cosine of the angle between the surface normal vector and one of the alkyl chain of the cation when the other alkyl chain is nearly parallel to the surface normal (continuous lines). Shown in dashed lines are the data reproduced from Figure 4.8 (c) for comparison.

orientation (given that the first alkyl is already parallel) is likely to be attained by the formation of gauche defect(s), whose occurrence probability increases with chain length. Figure 4.10 depicts snapshots of the symmetric and asymmetric cations at the interface showing their orientations.

The dependence of these orientational preferences on the location of the ions can be studied using the second order Legendre polynomial function ($\mathrm{P}_2(\theta)$) [6, 7, 14].

$$\langle P_2(\theta)\rangle = \langle \frac{1}{2}(3\cos^2\theta - 1)\rangle \tag{4.1}$$

The function attains a value of zero for isotropic distribution. Its value is one and -0.5 for parallel and perpendicular orientations respectively.

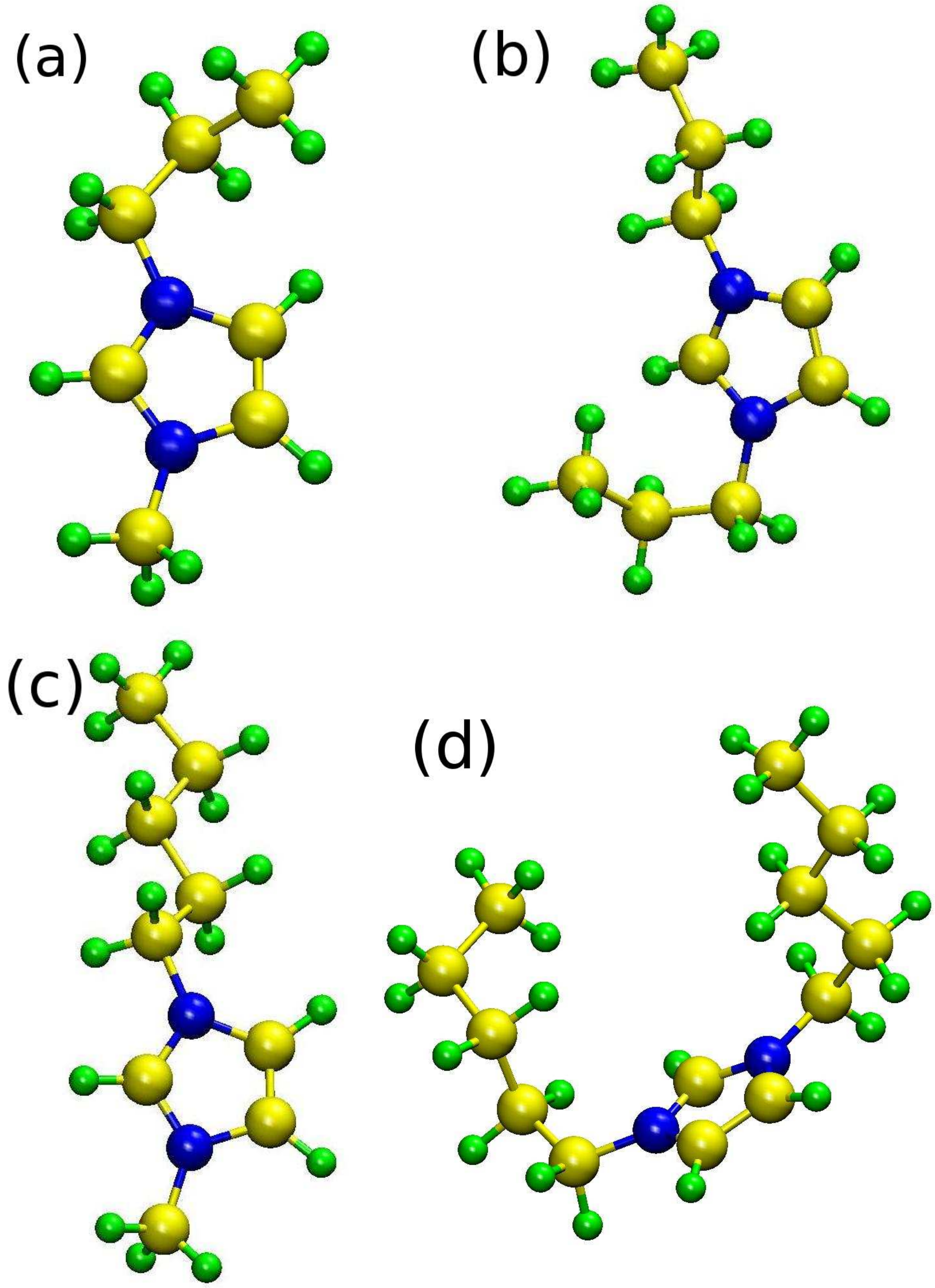

Figure 4.10: Illustrating the orientation of cations at the interface : (a) $[C_3C_1]^+$ (b) $[C_3C_3]^+$ (c) $[C_5C_1]^+$ (d) $[C_5C_5]^+$. The colour scheme is – Yellow: Carbon, Green: Hydrogen, Blue: Nitrogen

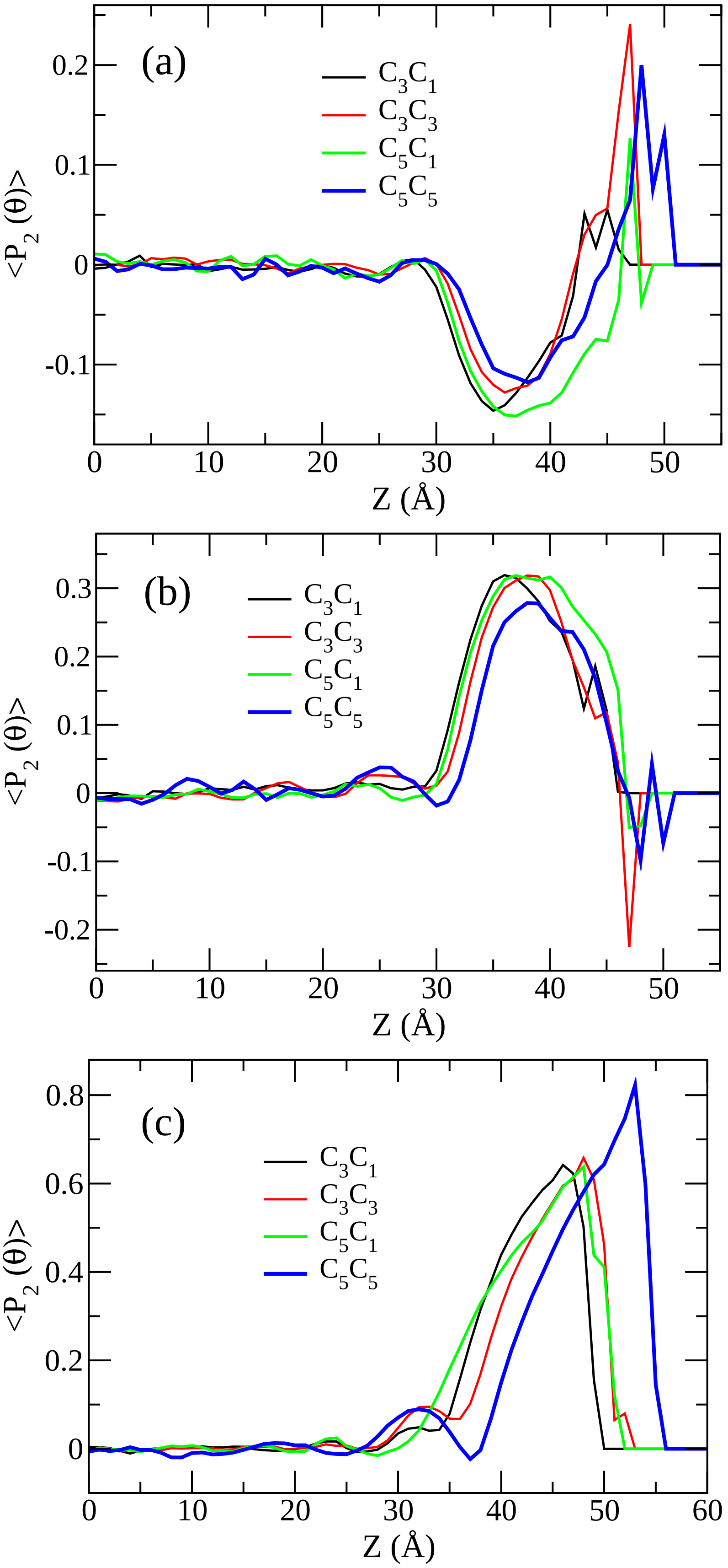

Figure 4.11: Second order Legendre polynomial function for (a) ring-normal vector (b) NN vector (c) alkyl chain vector.

Figure 4.11 shows the average of this function for angles that the ring normal, NN vector and the alkyl chains make with the surface normal. In agreement with earlier studies [6,14,32,33], at the interface, it is observed that $\langle P_2(\theta) \rangle$ is negative for the ring normal and is positive and large for the alkyl chain. This shows that the cations are aligned perpendicular to the surface. The NN axis and the alkyl chain are parallel to the surface normal at the interface region. The sharp features at the vapour edge of the interface arise from very few molecules (based on number density). These show orientational preferences opposite to that seen in the densest region of the interface. Although the alkyl chains of these few molecules project out into the vapour phase, their ring planes lie on the liquid surface. In an earlier experimental study, Baldelli and co-workers [34] have shown that anions present on the surface do not influence much the orientation of cations. The important deciding factors for the orientational preferences of the cations (studied in this work) at the interface are their symmetry and chain length. The probability of the cation ring being perpendicular and the alkyl chains being parallel to the surface normal decrease for the symmetric systems, relative to those with asymmetric cations.

4.3.3 Charge Densities and Electrostatic Potentials

The profiles for charge densities of the systems were obtained by integrating over all the individual atomic charges of the ions in each layer and are shown in Figure 4.12. As the anions are exposed more towards the interface than the ring centre of the cations, the total charge at the interface is negative. Although the alkyl groups of the cations occupy the outermost layer, they carry almost negligible charge and hence they play a less active role in determining the charge density. As the chain length gets longer, a small positive charge density can be observed on the surface possibly arising from the alkyl group. Yet, the total interfacial charge density is predominantly negative. A large positive region is also observed beneath the negative region which arises from the presence of cation ring centres. The presence of alternating positive and negative charge density regions is a direct evidence of out-of-phase oscillations in the cation and anion number density profiles, as documented earlier by us [12].

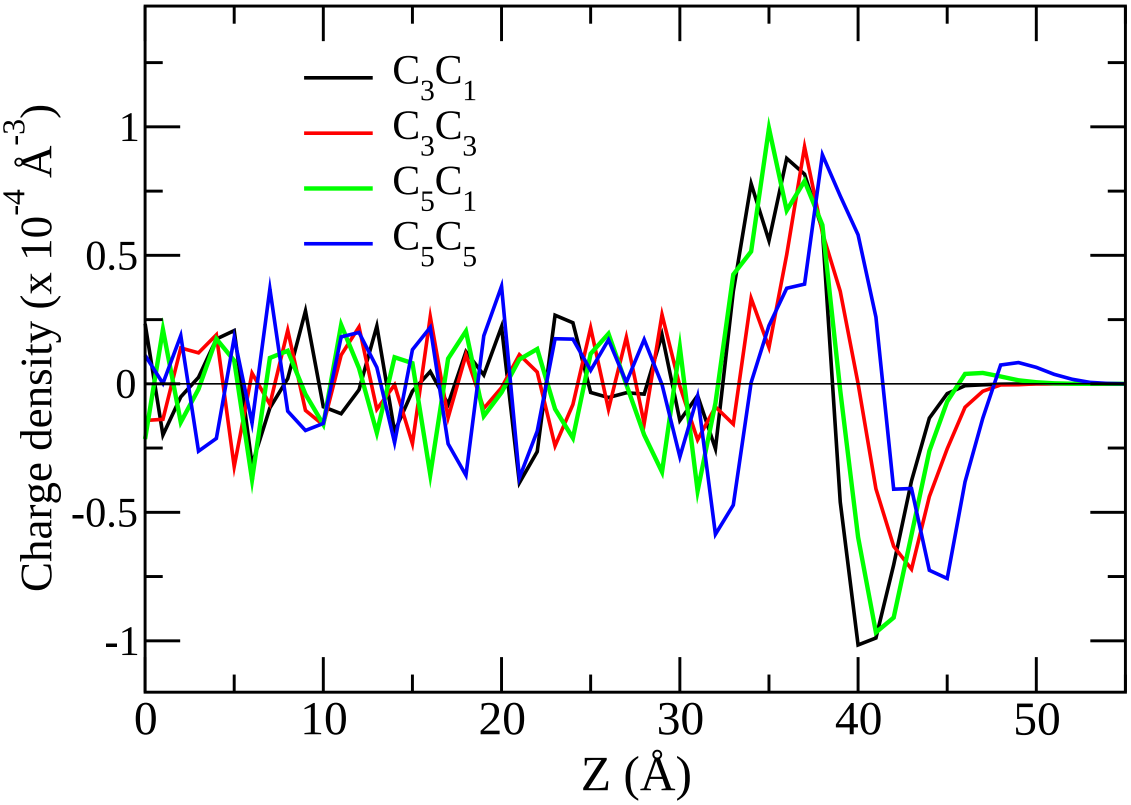

Figure 4.12: Charge density profiles as a function of distance along the surface normal.

Profiles of the electrostatic potential were obtained by integrating Poisson's equation along the direction of the surface normal. The expression is,

$$\phi(z_0) = \frac{1}{\epsilon_0}\int_{-\infty}^{z_0}(z - z_0)\rho(z)dz \tag{4.2}$$

where ρ(z) is the charge density at position 'z' in the direction of surface normal.

Figure 4.13 shows the electrostatic potential (esp) profiles along the surface normal (z-direction) for all the systems. The potential difference between vacuum and bulk mirrors the behavior of the charge density profile. [C_3C_1][NTf_2] compound shows the largest difference while [C_5C_5][NTf_2] shows the least.

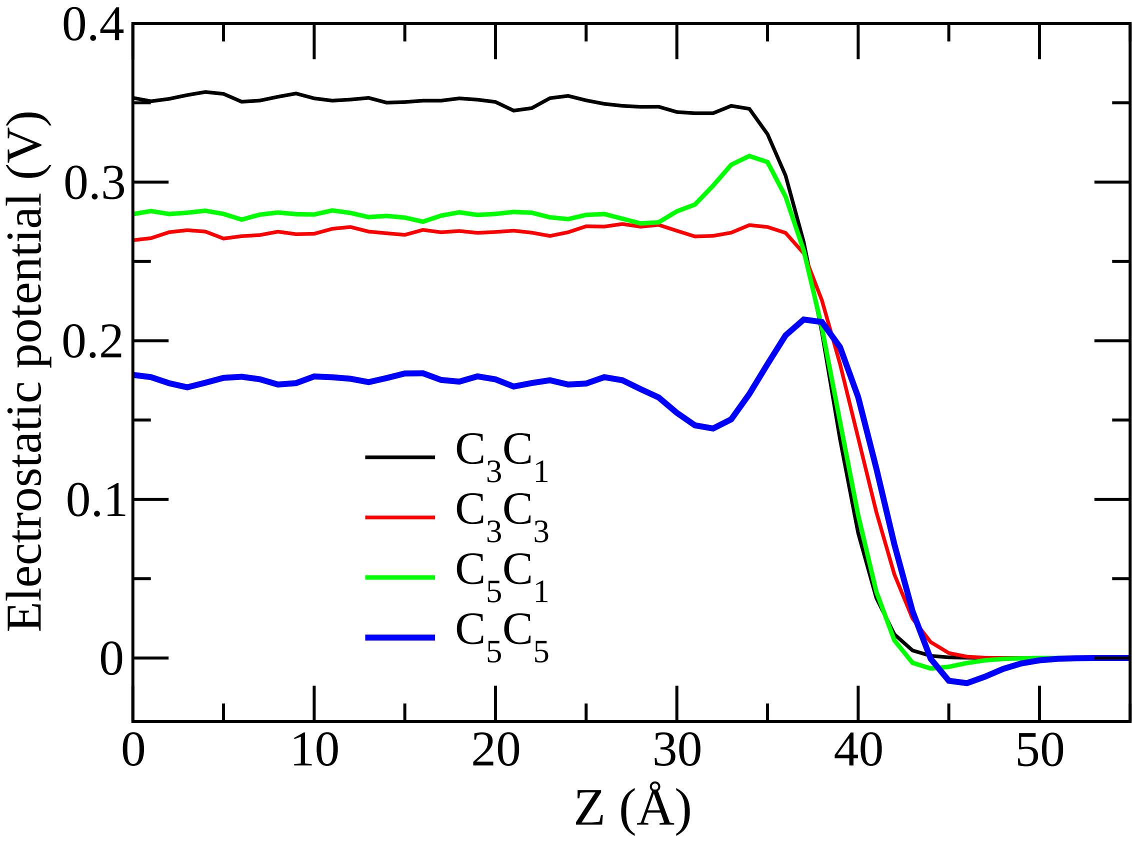

Figure 4.13: Electrostatic potential profiles in the surface normal direction.

The electrostatic potential determines the potential experienced by a test charge moving across the interface. Systems with smaller alkyl chains ([C_3C_1][NTf_2], [C_3C_3][NTf_2]) exhibit large negative charge densities at the interface which leads to a large positive potential. In longer alkyl chain systems ([C_5C_1][NTf_2], [C_5C_5][NTf_2]), the potentials have a small negative value just at the interface due to the presence of alkyl groups projecting out of the liquid into the vapour phase. Padua and co-workers have studied recently the surface properties of [C_6C_1][NTf_2] [35], and observed an electrostatic potential of around 0.2 V in bulk at 423 K. The potential difference for [C_5C_1][NTf_2] was found to be around 0.28 V at 300 K, which is not inconsistent with their data. The mean potential values in bulk are 0.35 V, 0.27 V, 0.28 V, and 0.18

V for $[C_3C_1][NTf_2]$, $[C_3C_3][NTf_2]$, $[C_5C_1][NTf_2]$, and $[C_5C_5][NTf_2]$ respectively. The effect of size difference between the cation and anion on the interfacial electrostatic potential has been studied by Bresme and co-workers on a primitive model [36] and by Lynden-Bell and co-workers on imidazolium based ILs [10].

Comparing the esp profiles for $[C_3C_3][NTf_2]$ and $[C_5C_1][NTf_2]$, it can be observed that the former does not exhibit any peak at the interface unlike the latter, consistent with observations made earlier on their number density profiles.

4.3.4 Surface Tension

The surface tension (γ) of the liquids were calculated from the pressure components in the direction parallel and perpendicular to the interface as,

$$\gamma = \frac{L_z}{2}(\langle P_{zz}\rangle - \frac{1}{2}[\langle P_{xx}\rangle + \langle P_{yy}\rangle]) \tag{4.3}$$

where P_{xx}, P_{yy}, and P_{zz} are the three principal components of the pressure tensor and L_z(=150 Å) is the box length along the surface normal. The factor of 2 takes care of the presence of two equivalent surfaces.

Earlier studies [14, 37–39] have shown that the surface tension of ionic liquids decreases with increase in the alkyl chain length of the cation and their branching. In an IL-vapour interface, the less active alkyl chains constitute the interface and the more active moieties (rings) are directed towards the bulk in order to minimize the surface energy [34]. Figure 4.14 shows the running average of the calculated surface tension for all the systems. The data has been averaged over the three independent trajectories.

The calculated surface tension values for the asymmetric IL systems are not in perfect agreement with experimental values [39]. The values are: 24.7 mN/m

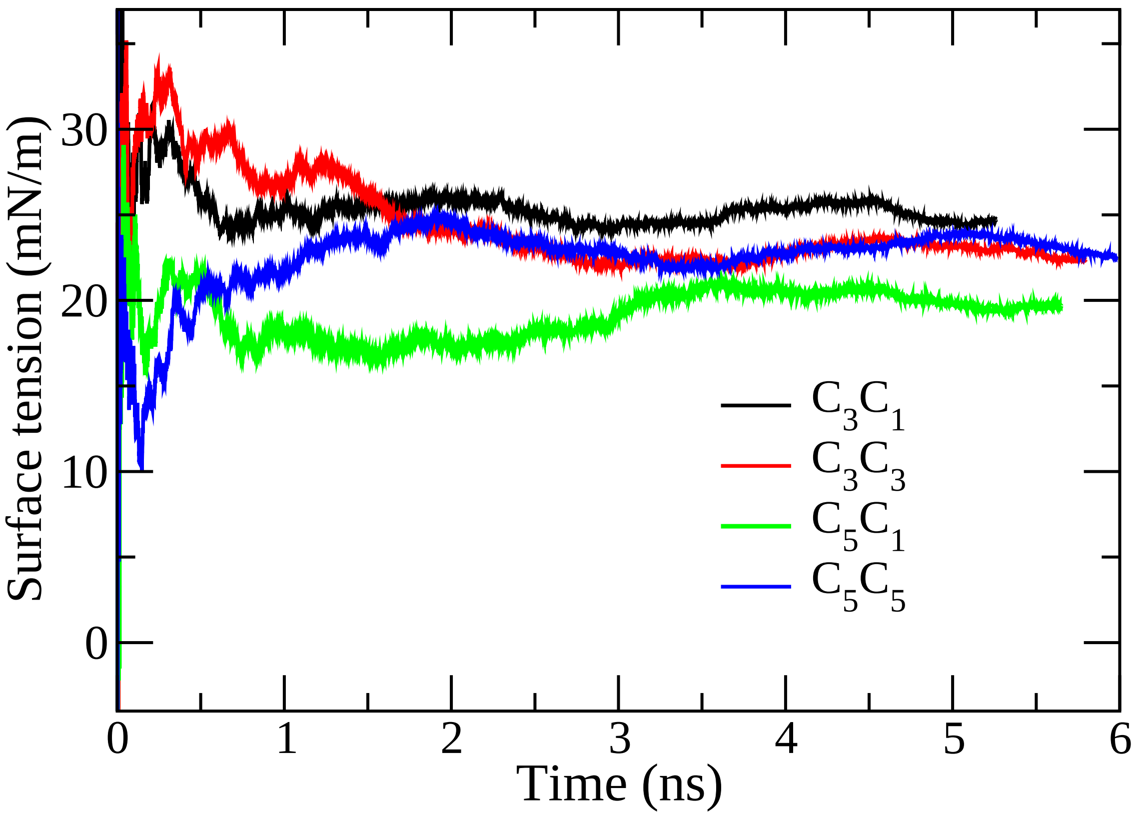

Figure 4.14: Running average of surface tension for all the systems.

(34.22) and 19.7 mN/m (32.41) for [C_3C_1][NTf_2] and [C_5C_1][NTf_2] respectively (experimental values in parentheses). The existence of finite size effects in the computational determination of surface tension has been documented earlier by Bresme and coworkers [40]. This could play a role in the current calculations also.

Coutinho *et al* have carried out a series of surface tension measurement experiments to systematically study the surface tension of ILs as a function of anion, cation alkyl chain length, cation alkyl chain symmetry, and temperature [38,39,41]. They report surface tension values of 35.37 mN/m and 34.22 mN/m for ([C_2C_2][NTf_2]) and ([C_3C_1][NTf_2]) [41] respectively. Consistent with their findings, it is noticed that the symmetric IL system [C_3C_3][NTf_2] has a higher surface tension (23 mN/m) than its asymmetric counterpart [C_5C_1][NTf_2] (19.7 mN/m) [C_5C_1][NTf_2] due to the presence of shorter alkyl chains in the former.

4.4 Conclusions

Atomistic molecular dynamics simulations of the liquid-vapour interfaces of four different ionic liquids have been carried out and the effect of the length of the alkyl groups and of the molecular symmetry of the imidazolium cations on the nature of the interface have been examined. The cation in many common ILs are asymmetric in the alkyl substitutions they carry on the ring, the current study compares MD results on the liquid-vapour interface for ILs containing symmetric and asymmetric cations. The properties of these liquids in bulk were studied by us earlier [20].

The density of these liquids in the bulk region of the current simulations agree well with experimental values. The surface of symmetric ILs is coated with alkyl chains, similar to that seen for asymmetric ILs. While both cations and anions are present in the densest region of the interface, the anions are located slightly towards the vapour side and the imidazolium ring centre of the cations are located slightly inwards, towards the liquid region. Among the liquids studied, the density of methyl groups at the interface is the highest for the $[C_3C_1][NTf_2]$ primarily due to its high bulk density. However, if one normalizes the methyl density profile by the respective bulk values, $[C_5C_5][NTf_2]$ possesses the highest relative interfacial methyl density, illustrating the dominant role played by the length of the alkyl group. This observation is also corroborated by a similar analysis for the cation ring number density.

The alkyl groups are oriented normal to the surface plane and this propensity decreases for symmetric ILs. This is due to the fact that if one alkyl group is oriented outwards and normal to the liquid surface, the other alkyl group has to perforce be oriented into the liquid due to the intrinsic geometry of the cation. The presence of such a hydrophobic group oriented into the polar liquid and normal to the interface is likely to be energetically prohibitive. This explains the reduction in the probability of cations with alkyl chains oriented normal to the interface in symmetric ionic liquids. However, this situation can be avoided by the formation of *gauche* defects on the chain which is likely in cations with long alkyl groups. To summarize, orientational preferences of the ions at the interface are diminished in symmetric ILs, relative to asymmetric ones. This is a new observation.

The orientational preferences of the ions are sustained into the liquid to about 15 to 20 Å from the interface. Despite being more dense, interfacial oscillations in the number density profiles for ILs with asymmetric [$C_nC_1$im] cations are reduced both in amplitude and in range than those in ILs constituted by symmetric ([$C_nC_n$im]) cations. The larger bulk density in the former is seen to naturally lead to a larger electrostatic potential difference in the bulk region of the liquid, with respect to vacuum.

Bibliography

[1] C. Aliaga, C. S. Santos, S. Baldelli, *Phys. Chem. Chem. Phys.*, **9**, 3683, (2007).

[2] T. Z. Timan, D. Ceresoli, U. Tartaglino, E. Tosatti, *Phys. Rev. Lett.*, **94**, 176105, (2005).

[3] T. J. Sluckin, *J. Chem. Soc. Faraday Trans.2*, **77**, 1029, (1981).

[4] T. Iwahashi, T. Nishi, H. Yamane, T. Miyamae, K. Kanai, K. Seki, D. Kim, Y. Ouchi, *J. Phys. Chem. C*, **113**, 19237, (2009).

[5] I.S. Martinez, S. Baldelli, *J. Phys. Chem. C*, **114**, 11564, (2010).

[6] R.M. Lynden-Bell, *Mol. Phys.*, **101**, 2625, (2003).

[7] R.M. Lynden-Bell, J. Kohanoff, M.G. Del Popolo, *Faraday Discuss.*, **129**, 57, (2005).

[8] C. Pinilla, M.G. Del Popolo, R.M. Lynden-Bell, J. Kohanoff, *J. Phys. Chem. B*, **109**, 17922, (2005).

[9] R.M. Lynden-Bell, M.G. Del Popolo, *Phys. Chem. Chem. Phys.*, **8**, 949, (2006).

[10] R.M. Lynden-Bell, M.G. Del Popolo, T.G.A. Youngs, J. Kohanoff, C.G. Hanke, J.B. Harper, C.C. Pinilla, *Acc. Chem. Res.*, **40**, 1138, (2007).

[11] E. Sloutskin, B.M. Ocko, L. Tamam, I. Kuzmenko, T. Gog, M. Deutsch, *J. Am. Chem. Soc.*, **127**, 7796, (2005).

[12] B.L. Bhargava, S. Balasubramanian, *J. Am. Chem. Soc.*, **128**, 10073, (2006).

[13] E. Sloutskin, R.M. Lynden-Bell, S. Balasubramanian, M. Deutsch, *J. Chem. Phys.*, **125**, 174715, (2006).

[14] T. Yan, S. Li, W. Jiang, X. Gao, B. Xiang, G.A. Voth, *J. Phys. Chem. B*, **110**, 1800, (2006).

[15] M. Sha, G. Wu, H. Fang, G. Zhu, Y. Liu, *J. Phys. Chem. C*, **112**, 18584, (2008).

[16] M. Sha, G. Wu, Y. Liu, Z. Tang, and H. Fang, *J. Phys. Chem. C*, **113**, 4618, (2009).

[17] S.V. Dzyuba, R.A. Bartsch, *Chem. Commun.*, 1466, (2001).

[18] D. Xiao, L.G. Hines Jr., S. Li, R.A. Bartsch, E.L. Quitevis, O. Russina, A. Triolo, *J. Phys. Chem. B*, **113**, 6426, (2009).

[19] S.G. Raju, S. Balasubramanian, *J. Mater. Chem.*, **19**, 4343, (2009).

[20] S.G. Raju, S. Balasubramanian, *J. Phys. Chem. B*, **114**, 6455, (2010).

[21] S.J. Plimpton, *J. Comp. Phys.*, **117**, 1, (1995).

[22] T. Köddermann, D. Paschek, R. Ludwig, *ChemPhysChem*, **8**, 2464, (2007).

[23] R.W. Hockney and J.W. Eastwood, Computer Simulation Using Particles, 2nd ed., 1988, IOP.

[24] E. Quitevis (Private Communication).

[25] J.N.A.C. Lopes, A.A.H. Padua, *J. Phys. Chem. B*, **110**, 3330, (2006).

[26] C. Waring, P.A.J. Bagot, J.M. Slattery, M.L. Costen, K.G. McKendrick, *J. Phys. Chem. Lett*, **1**, 429, (2010).

[27] C. Waring, P.A.J. Bagot, J.M. Slattery, M.L. Costen, K.G. McKendrick, *J. Phys. Chem. A*, **114**, 4896, (2010).

[28] F. Maier, T. Cremer, C. Kolbeck, K.R.J. Lovelock, N. Paape, P.S. Schulz, P. Wasserscheid, H.-P. Steinrück, *Phys. Chem. Chem. Phys.*, **12**, 1905, (2010).

[29] W. Jiang, Y. Wang, T. Yan, G.A. Voth, *J. Phys. Chem. C*, **112**, 1132, (2008).

[30] S.S. Sarangi, B.L. Bhargava, S. Balasubramanian, *Phys. Chem. Chem. Phys.*, **11**, 8745, (2009).

[31] B. Wu, J. Zhang, T.K. Minton, K.G. McKendrick, J.M. Slattery, S. Yockel, G.C. Schatz, *J. Phys. Chem. C*, **114**, 4015, (2010).

[32] S. Rivera-Rubero, S. Baldelli, *J. Phys. Chem. B*, **110**, 4756, (2006).

[33] C.S. Santos, S. Baldelli, *J. Phys. Chem. B*, **111**, 4715, (2007).

[34] C. Aliaga, S. Baldelli, *J. Phys. Chem. B*, **111**, 9733, (2007).

[35] A.S. Pensado, P. Malfreyt, A.A.H. Padua, *J. Phys. Chem. B*, **113**, 14708, (2009).

[36] F. Bresme, M. Gonzalez-Melchor, J. Alejandre, *J. Phys: Cond. Matt.*, **17**, S3301, (2005).

[37] S.V. Dzyuba, R.A. Bartsch, *ChemPhysChem*, **3**, 161, (2002).

[38] M.G. Freire, P.J. Carvalho, A.M. Fernandes, I.M. Marrucho, A.J. Queimada, J.A.P Coutinho, *J. Coll. Inter. Sci.*, **314**, 621, (2007).

[39] P.J. Carvalho, M.G. Freire, I.M. Marrucho, A.J. Queimada, J.A.P. Coutinho, *J. Chem. Eng. Data*, **53**, 1346, (2008).

[40] M. Gonzalez-Melchor, F. Bresme, J. Alejandre, *J. Chem. Phys.*, **122**, 104710, (2005).

[41] P.J. Carvalho, C.M.S.S. Neves, J.A.P. Coutinho, *J. Chem. Eng. Data*, **55**, 3807, (2010).

Chapter 5

Nanoclusters of Room Temperature Ionic Liquids: A Molecular Dynamics Simulation Study

5.1 Introduction

Nearly all the studies on the ionic liquid (IL)-vapour interface have considered a planar interface. They agree that the surface is hydrophobic, with the alkyl groups of the cation projecting out into the vapour phase [1,2]. Oscillations in the number density of the ions and consequently in the electron density were observed. One of the features brought out by these MD simulations is the out-of-phase oscillations present in the density profiles of the cation and anion at the interface, which implies charge ordering [1].

So far, there have been no studies on the structure of large, free standing clusters of ionic liquids. These are required to identify possible differences in the structure of the liquid at the interface between a planar and a curved surface. Studies on IL clusters are also important as model systems of ternary microemulsions. Various workers have studied microemulsions in which ILs form the polar core, water or an organic solvent (cyclohexane or toluene) being the continuous medium and a surfactant such as Triton X-100 (TX-100) mediating these two components [3–9]. Kankan and co-workers have done femtosecond solvation dynamics experiments on a microemulsion consisting of a polar pool of IL (1-pentyl-3-methyl-imidazolium tetrafluoroborate) and the surfactant TX-100 molecules forming the non-polar peripheral shell around the IL pool [6]. The IL pool in such systems is typically spherical with values of the hydrodynamic diameter ranging between 8 and 20 nm in the case of water [3] and close to 100 nm in the case of organic solvents [3, 9]. Figure 5.1 depicts a cartoon form of the above described ternary microemulsions.

Small angle neutron scattering experiments on [hmim][BF_4]/TX-100/cyclohexane microemulsions have shown that the diameter of the IL core plus the stabilizing surfactant layer is around 2 nm [7]. The constitution of the vapour phase of ILs is believed to be ion pairs [10–13]. Slightly larger aggregates could also exist, but are rare. Recently, Pinilla and co-workers have studied ground state geometries of small clusters (less than 32 ion pairs) of the ionic liquid [bmim][Tf], using *ab initio* and empirical potential computer simulations [14]. Ludwig has obtained thermodynamic properties of ILs by applying quantum chemical calculations to small (up to 16 ion pairs) clusters [15]. Maginn *et al* have calculated the enthalpy of vaporization for IL clusters as a function of temperature and alkyl chain lengths [13]. They proved that non-neutral clusters have much higher vaporization enthalpies than their neutral counterparts. Hunt *et al* [16] have investigated structures of ion pairs to understand liquid state properties.

In the current work, the focus was on nanometric sized ionic liquid droplets present in free space at room temperature. Their structural (sizes, shapes, number

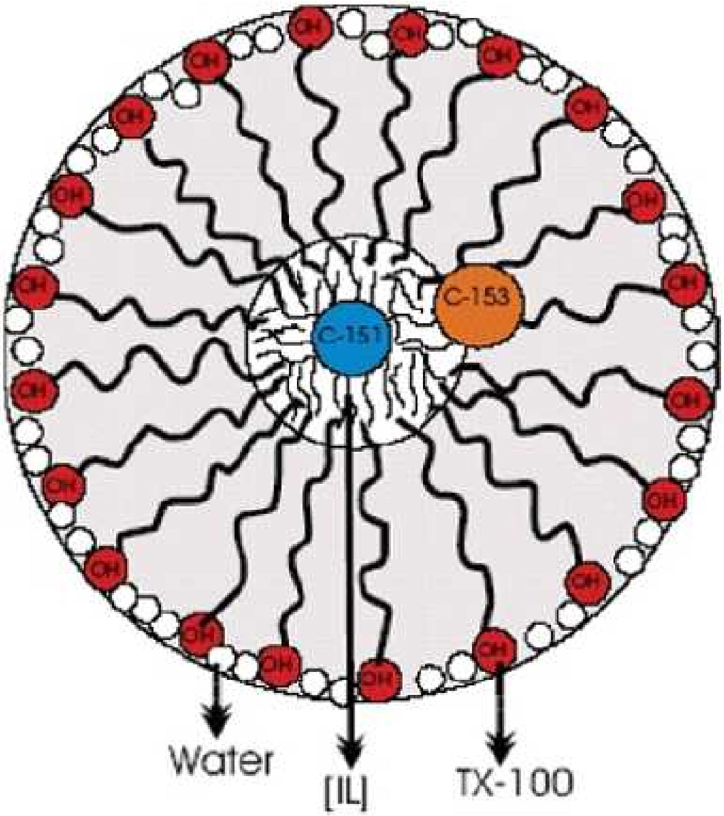

Figure 5.1: Model picture of a ternary microemulsion having the ionic liquid in the core

densities of ions, orientations), energetics(cohesive energies), and electrostatic characteristics (charge densities and electrostatic potentials) were determined through molecular dynamics simulations using a well tested empirical potential model [17]. This model has been benchmarked against *ab initio* MD simulations and predicts experimental quantities such as density (as a function of temperature and pressure), surface tension, enthalpy of vapourization, X-ray and neutron structure factors and small angle X-ray scattering very well. The effective potential of interaction between these clusters as a function of the inter-cluster center of mass separations has also been investigated, which can be used in developing coarse grain models of IL based microemulsions.

5.2 Methodology and Details of Simulation

Clusters containing 32, 100, 256, 360, and 600 ion pairs (1024, 3200, 8192, 11520, 19200 atoms respectively) of the ionic liquid 1-*n*-butyl-3-methylimidazolium hexafluorophosphate, [bmim][PF_6] have been studied using the all-atom model developed by us [17]. The potential model is fully flexible. Intramolecular interactions include stretching, bending, and dihedral terms while site-site Lennard-Jones and Coulombic terms constitute the non-bonded interactions. Classical molecular dynamics simulations were performed with the LAMMPS program [18] at a temperature of 300 K. Temperature control was achieved by coupling the system to a Nosé-Hoover thermostat with a coupling constant of 0.5 ps. The simulations were carried out without periodic boundary conditions in order to form and retain clusters. The non-bonded interactions were not cut off, and all site-site interactions were included in the calculation of the total potential energy. The equations of motion were integrated with a time step of 0.5 fs using the velocity Verlet algorithm. Three different simulations were carried out for each system size, except for the 600 ion pair system, for which ten independent trajectories were generated, each starting from a different initial configuration. The total run length was about 2 ns for all the system sizes after a period of equilibration. Coordinates of all the atoms were stored at an interval of 0.5 ps for further analysis. Calculated quantities were averaged over the above mentioned independent simulations and the error bars were obtained by block averaging.

In addition to these all-atom MD simulations, MD simulations of two clusters

(100 ion pairs and 6912 ion pairs) were carried out using a coarse grained model of [bmim][PF_6]. The force field for the coarse grained simulations were taken from [19].

The geometry of the clusters were characterized from the eigen values $\lambda_1 \leq \lambda_2 \leq \lambda_3$ of the radius of gyration tensor S. Which describes the second moments of position of all the atoms and defined as,

$$S_{mn} = \frac{1}{N} \sum_{i=1}^{N} r_m^{(i)} r_n^{(i)} \tag{5.1}$$

where $r_m^{(i)}$ is the mth Cartesian coordinate of the position vector $r^{(i)}$ of the ith atom. The trace $\sum_i \lambda_i$ gives the isotropic squared radius of gyration R_g^2, while the anisotropy of the cluster is measured from the asphericity parameter A_2 [20,21]. Gyration tensor is related to the moment of inertia tensor, the difference between them is that the atom positions are weighed by mass in the inertia tensor. Whereas the gyration tensor depends only on the particle positions. Hence, the gyration tensor would be proportional to the inertia tensor if all the particle masses are identical.

$$R_g^2 = \lambda_1 + \lambda_2 + \lambda_3 \tag{5.2}$$

Radius of gyration describes the way in which the area of a cross-section is distributed around its centroidal axis.

$$A_2 = \frac{(\lambda_1 - \lambda_2)^2 + (\lambda_2 - \lambda_3)^2 + (\lambda_3 - \lambda_1)^2}{2(\lambda_1 + \lambda_2 + \lambda_3)^2} \tag{5.3}$$

A_2 is always positive and it ranges from a value of zero for a symmetric sphere to one for a rod.

The radial profiles of the electrostatic potentials were determined using the equation,

$$\phi(r) = 1/4\pi\epsilon_0 \left[\left\langle \sum_{r_i<r} q_i/r + \sum_{r_i>r} q_i/r_i \right\rangle \right] \tag{5.4}$$

where q_i is the charge on the ith atom and r_i is the radial distance from the centre of mass (COM) of the cluster for the ith atom. Angular brackets represent the time average of the quantity.

The derivation of the formula is direct from classical electrodynamics. Suppose there is a charged sphere of radius R and net charge Q. In the case of symmetrically distributed charges, the electrostatic potential outside the sphere would be same as that from a point charge 'Q' placed at the centre of the sphere. Thus, for any point r > R,

$$\phi(r) = 1/4\pi\epsilon_0 * Q/r \tag{5.5}$$

For a conducting sphere, the electrostatic potential inside the sphere is same everywhere throughout the conductor, and is equal to the value of the potential at the surface. So, for any point r < R,

$$\phi(r) = 1/4\pi\epsilon_0 * Q/R \tag{5.6}$$

This formula was previously used to calculate the radial profile of electrostatic potential for water clusters with spherical geometry by Brodskaya and co-workers [22, 23].

In the case of a planar interface, one can calculate the density profile by using a constant slab width for binning. However, the use of a constant radial shell width to calculate similar profiles for the clusters studied here will lead to very few atoms contributing to shells near the core region of the cluster and much larger number of atoms contributing to shells far away from the core. In order to obtain reasonable statistics over the entire cluster, it has been chosen to bin the density using spherical shells of constant volumes. Using this procedure, one may not be able to obtain the profile very close to the COM of the cluster; however, the statistical noise in the profiles would be much reduced.

5.3 Results and Discussions

5.3.1 Shapes and Sizes of Clusters

The geometry of the clusters were studied in terms of their radii of gyration (R_g, Equation 1) and asphericity parameters (A_2, Equation 2). The eigen values of the radius of gyration tensor are listed in Table 5.1.

Figure 5.2(a) shows the radius of gyration as a function of cluster size (number of ion pairs, N). The dependence of R_g on N is inverse cubic, as expected. The asphericity parameter A_2 describes the shape of the clusters and its behaviour is shown in Figure 5.2(b). The small A_2 values indicate the spherical nature of all the clusters. Larger clusters are more spherical than smaller ones.

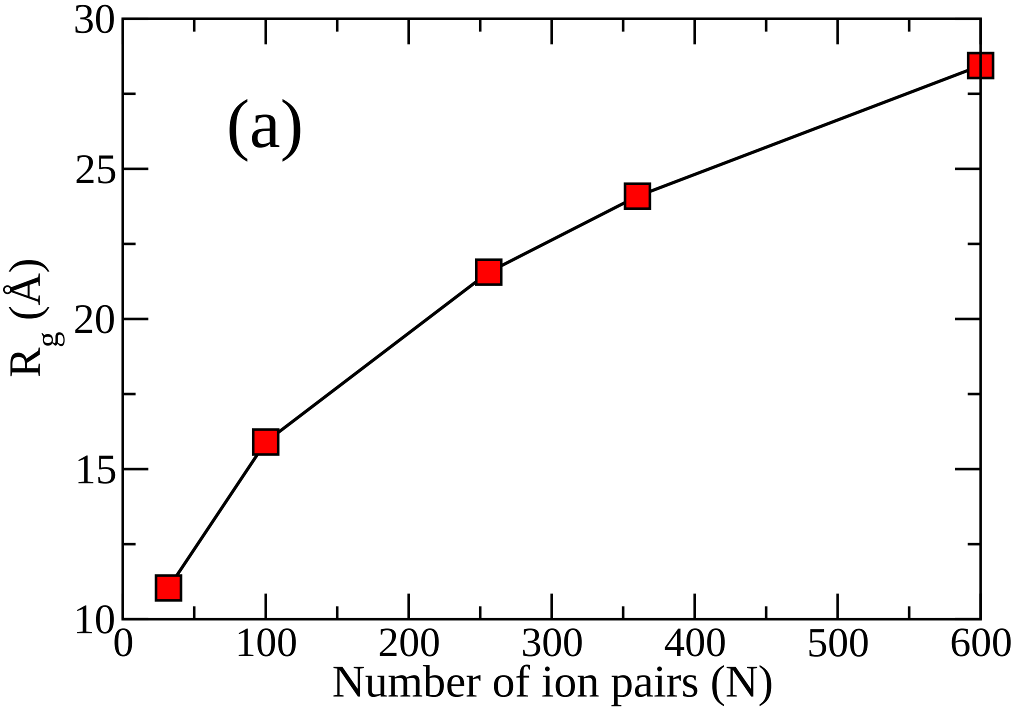

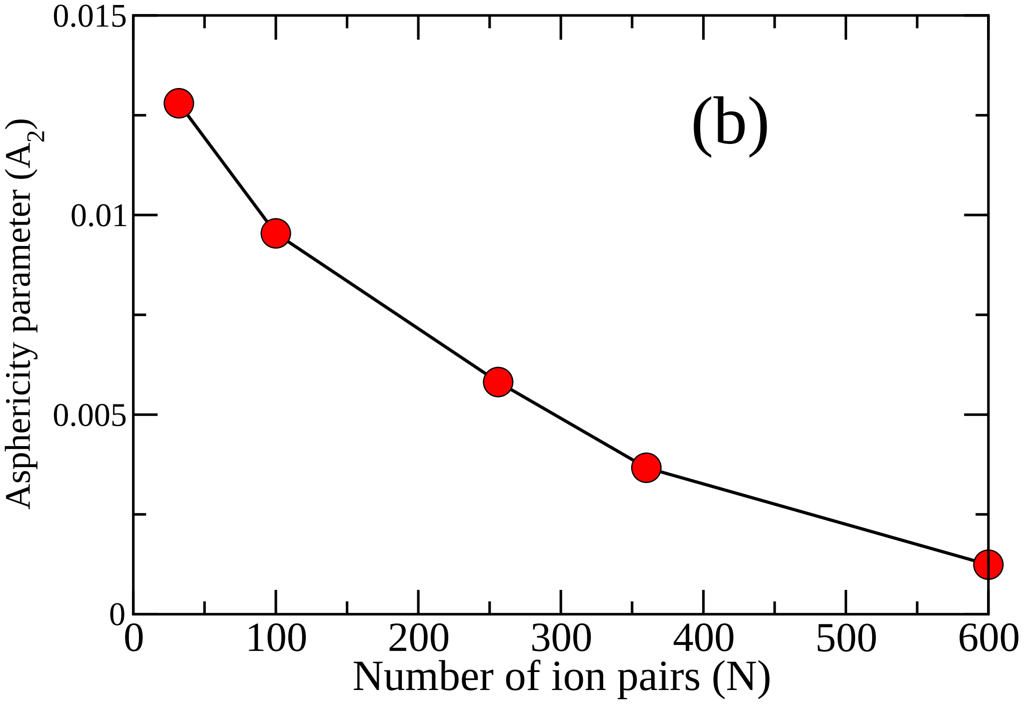

Figure 5.2: (a) Radius of gyration (b) Asphericity of clusters. The lines are drawn to guide the eye.

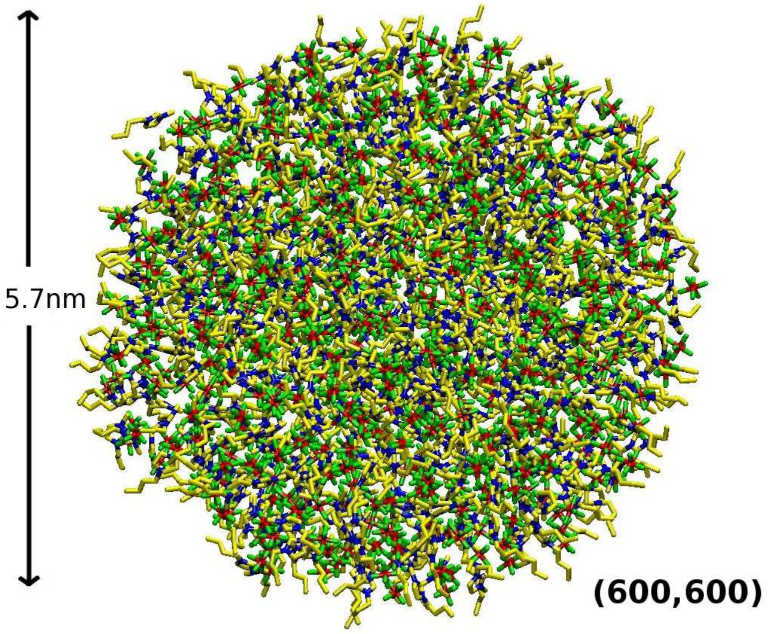

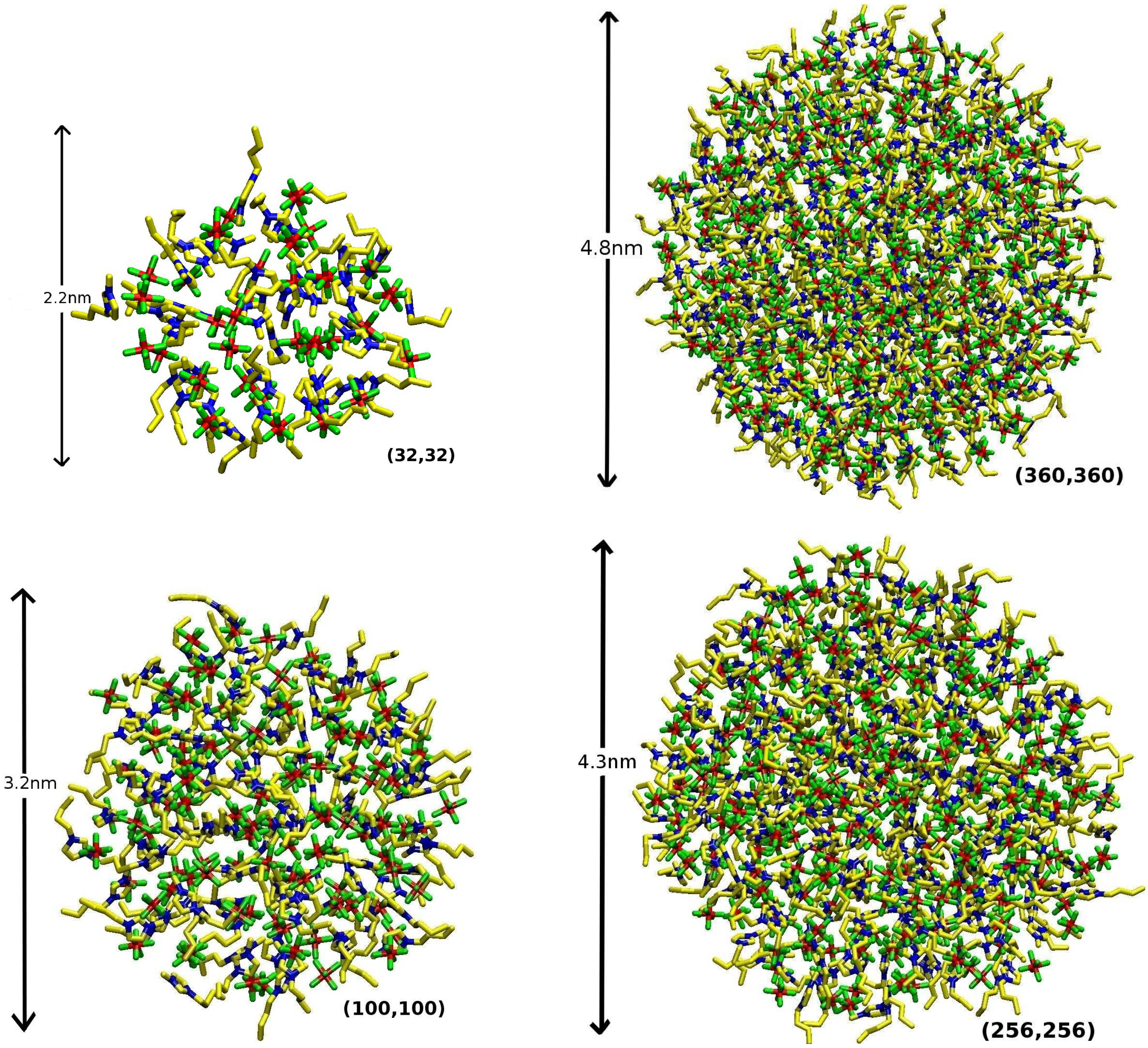

Figure 5.3: Snapshots of clusters. (n,n) is the number of cations and anions respectively. Hydrogen atoms have been removed for the sake of clarity. The colour scheme is as follows. Yellow: Carbon, Red: Phosphorus, Green: Fluorine, Blue: Nitrogen of the imidazolium ring. The bars on the left side of each of the snapshot shows the diameter of the respective cluster.

This can also be gleaned from the differences in the three eigen values of the gyration tensor shown in Table 5.1.

No. of ion pairs	λ_1 (Å^2)	λ_2 (Å^2)	λ_3 (Å^2)
32	33.2	39.4	48.6
100	71.7	83.0	98.2
256	134.0	158.4	174.6
360	175.2	186.7	204.4
600	254.6	267.2	276.1

Table 5.1: Eigen Values of the radius of gyration tensor

These observations are supported by snapshots of individual clusters shown in Figure 5.3.

5.3.2 Number Densities and Molecular Orientation

Shown in Figure 5.4 are the number density profiles of the ring centre of the cations, anion centres and that of the terminal carbon atom on the butyl chain of the cation, for the 600 ion pair cluster. The geometric centre of the imidazolium ring and the phosphorus atom are considered as cation and anion centres respectively.

Profound oscillations and layering are observed in the density profiles similar to those observed for planar ionic liquid-vapour interfaces [1, 24]. Many experimental [25] and simulation studies have shown that the butyl tails of the cations tend to face the vacuum side of the planar interface [2]. From the span of the number density profiles with the radial distance, it is inferred that the surface is populated with both cations and anions. However, the butyl tail groups of the cation are present on the outermost layer while the ring centres lie inside. Hence the surface will largely be hydrophobic. A marked difference between the cation and anion number densities is seen near the surface. The cation number densities show a clear maximum just below the surface (nearly 1.5 times of the number density in bulk region) while the first peak in the corresponding anion profile is flatter. The deep minima in the number density profile of the butyl chain occurs at the maxima of the cation and anion number density profiles at the surface region, indicating the polar (cation ring and anion groups) and non-polar (alkyl chains) phase segregation.

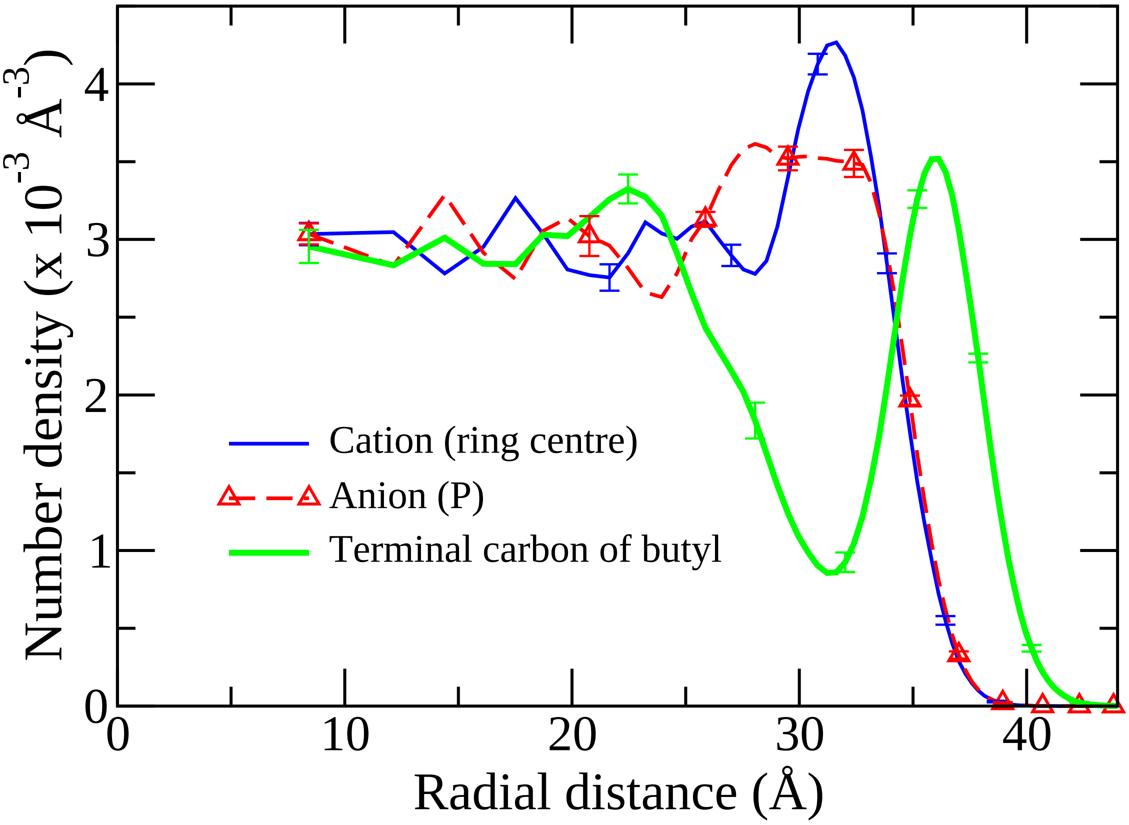

Figure 5.4: Number density profiles of cation ring centre, terminal carbon atom of the butyl group of the cation and of the anion for the cluster containing 600 ion pairs.

The number density profiles and orientaions for clusters of other sizes are similar to that discussed and the number density profiles for all clusters are shown in Figure 5.5.

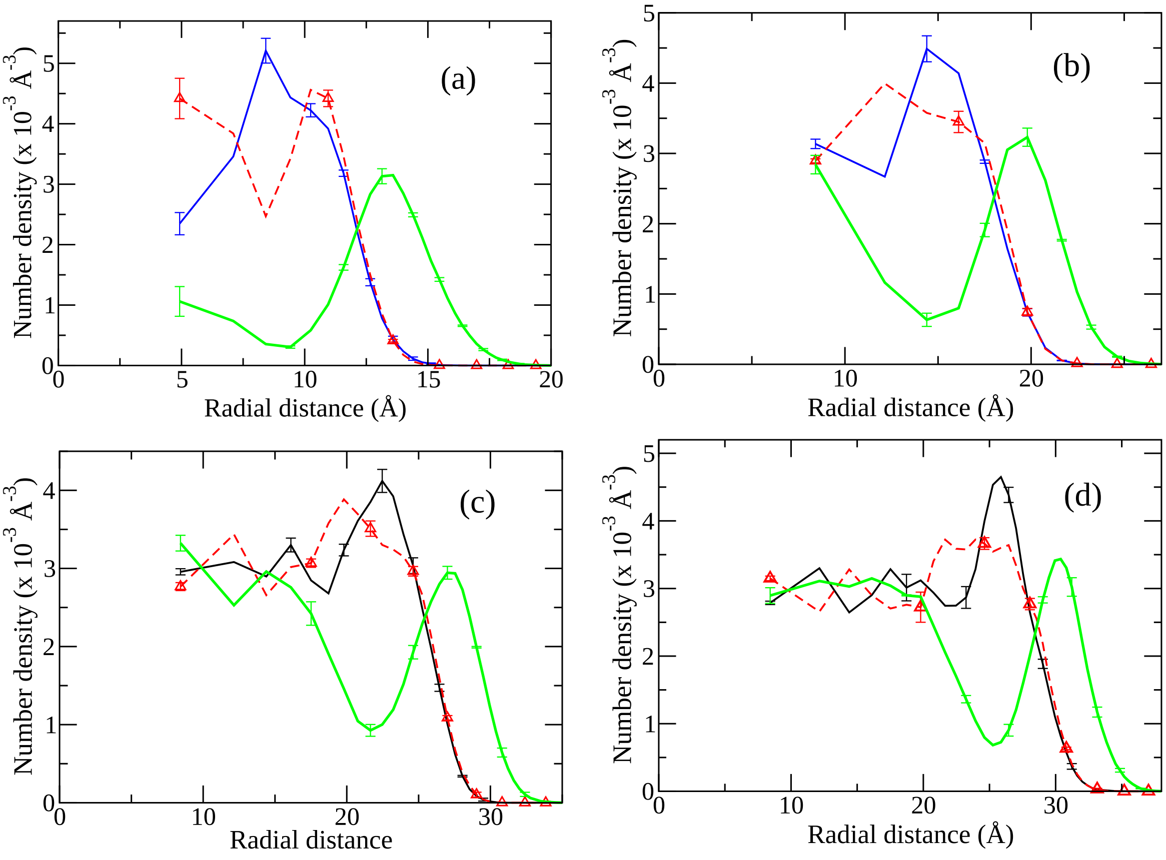

Figure 5.5: Number density profiles of cation ring centre, terminal carbon atom of the butyl group of the cation and of the anion for the cluster containing 600 ion pairs. (a)32 pairs, (b)100 pairs, (c)256 pairs, and (d) 360 pairs. The colour presentations are as follow, Black line : cation ring centre, Green lines : terminal carbon atom of the butyl group of the cation, Red lines with up-triangle symbols : anion

The orientation of the butyl chain and of the ring plane of the cations present on the surface of the cluster have been studied. The distribution of the angles formed by (a) the butyl chain and (b) the normal to the ring planes of cations with the radial vector (i.e., the vector joining the COM of the cluster to the the centre of the imidazolium ring) are shown in Figure 5.6. The most favoured orientation of the butyl chain is parallel to the surface normal and that of the ring centre is perpendicular to the surface normal. Such orientational preferences were also found by Del Popolo and co-workers for very small clusters of [bmim][Tf] [26].

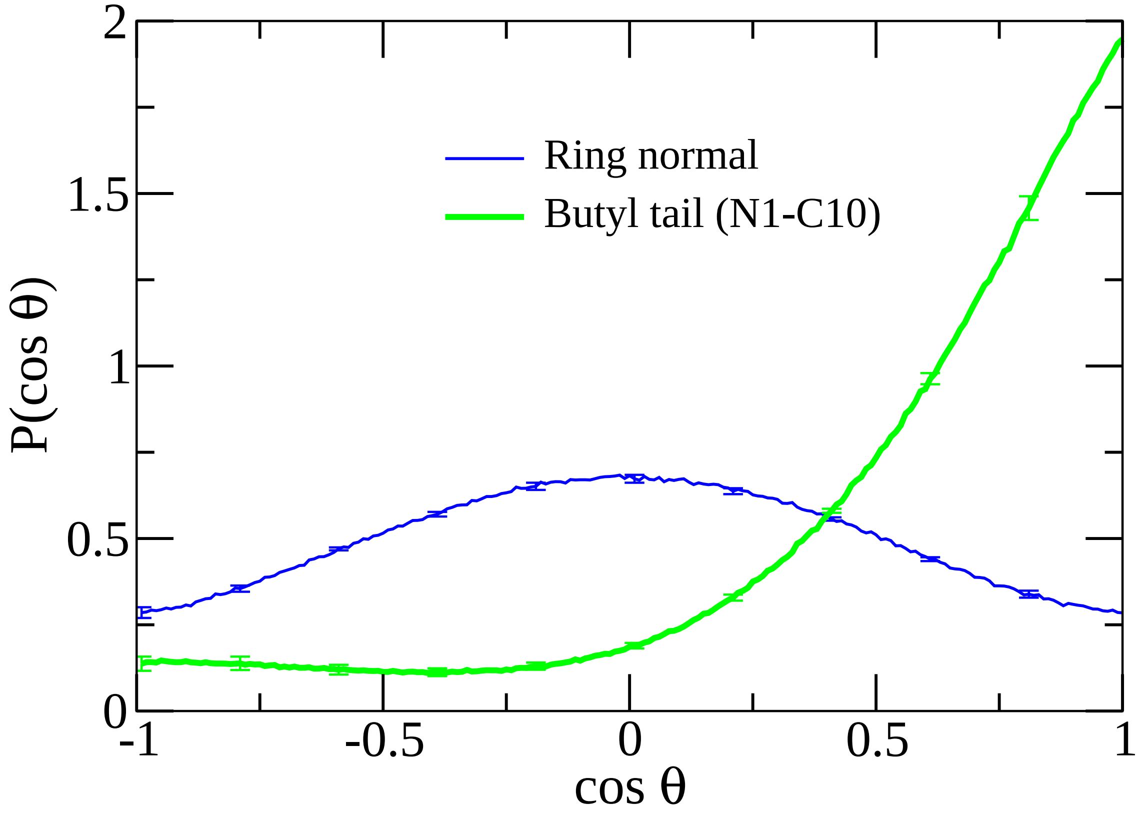

Figure 5.6: Distribution of the angle between the long axis of the butyl tail of the cation and of the normal to the imidazolium ring of the cation, with respect to the radial vector of the cluster. Data is shown for the 600 ion pair cluster.

5.3.3 Energy

The mean potential energy per ion pair in the cluster is larger (i.e., less negative) than that in the bulk ionic liquid as the molecules are energetically less stable on the surface of the cluster than in the bulk. In Figure 5.7 this difference in energy against the radius of gyration of the clusters is shown. One finds that even in the largest cluster studied using atomistic MD (the 600 ion pair one), the mean potential energy per ion pair is higher by 8.0 kJ/mole over the bulk value. However, for the 6912 ion pair cluster studied using coarse grained molecular dynamics (CGMD) simulations, this value is closer to that of the bulk, differing only by 1.0 kJ/mol. The difference in this energy arises from the undercoordinated ions present on the surface of the cluster. The most important message from Figure 5.7 is that the data

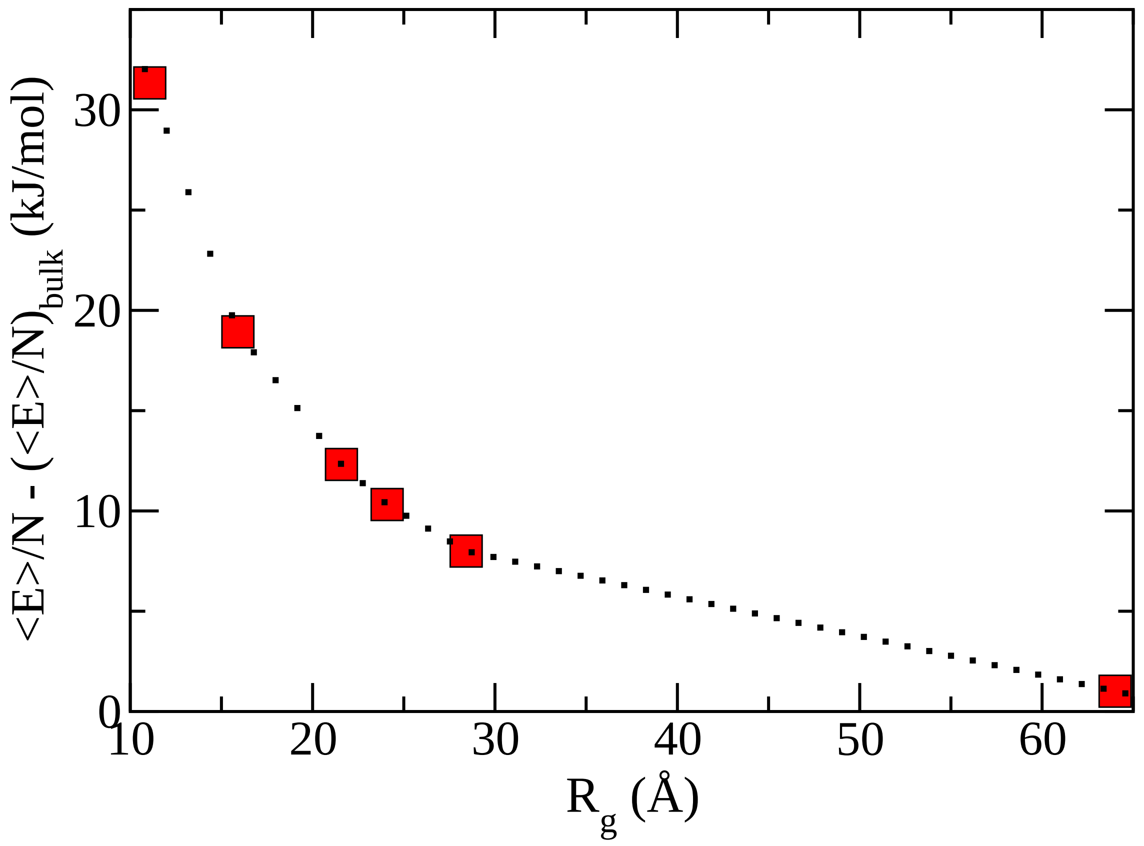

Figure 5.7: Difference in the potential energy per ion pair between clusters and bulk liquid plotted against their radii of gyration. The dotted line is a guide to the eye.

point from CGMD simulations fits neatly with the behaviour of the curve obtained from atomistic MD simulations (which was used to simulate clusters up to 600 ion pairs). The agreement between the two methods was also verified by carrying out simulations of a 100 ion pair cluster using the CGMD method. The difference in the mean energy per ion pair obtained from this simulation was 18.9 kJ/mol, relative to the energy of the bulk IL simulated using CGMD. This value is in exact agreement with the value obtained from atomistic MD simulations.

The distribution of the potential energies of the cations and anions as a function of their location away from the COM of the cluster have been evaluated and the same is illustrated in Figure 5.8 for the 600 ion pair system.

Note that the cations are in a deeper potential than the anions. This data can be

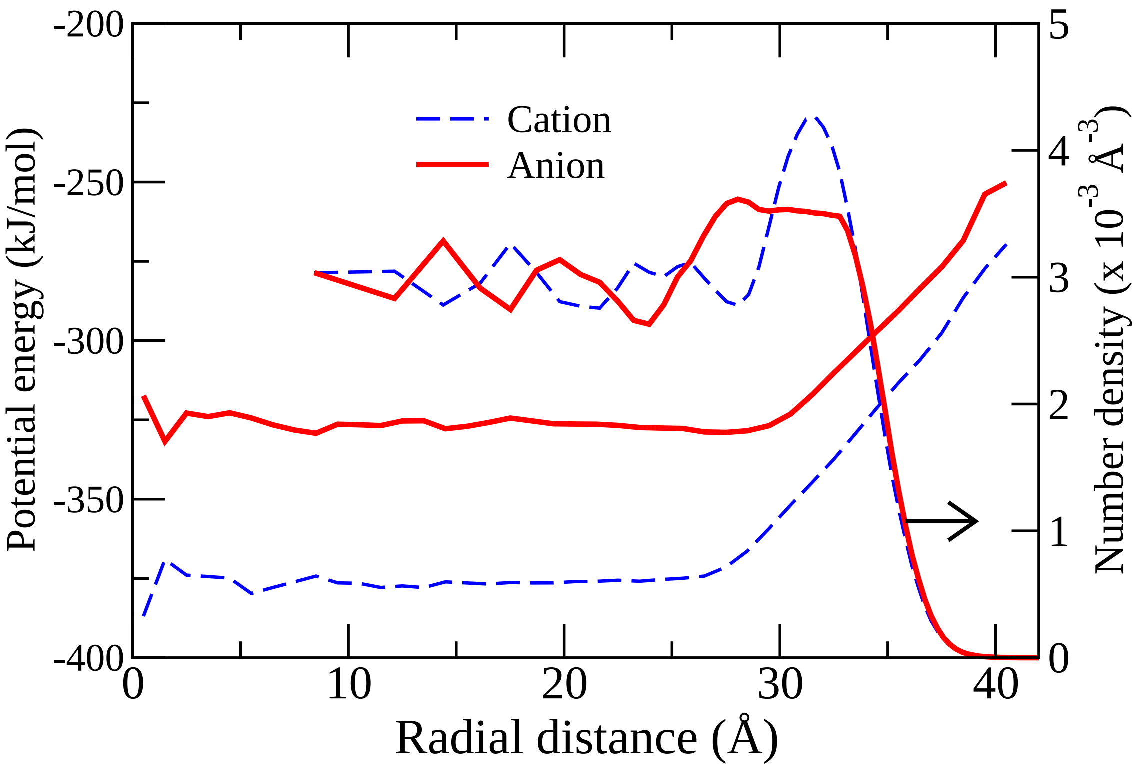

Figure 5.8: Dependence of the potential energy of ions on their position in the cluster with respect to the radial distance from the centre of mass of the cluster. The number density profiles are also shown for the sake of comparison. The data corresponds to the 600 ion pair cluster.

used to understand the origin of the difference between the potential energies of the cluster and that of the bulk liquid (shown in Figure 5.7). The contribution to the potential energy per ion pair for the cluster from those ions present on the surface has been calculated. For this purpose, those cations and anions which are present beyond a certain distance (28.5 Å and 30.5 Å respectively) from the cluster COM were identified as belonging to the surface. The mean value of their potential energy per ion pair is calculated to be -11.3 kJ/mol from Figure 5.8. This value is quite close to the difference between the potential energy per ion pair for the same cluster size and the bulk liquid (8.0 kJ/mol). Thus the weaker mean potential energy of the cluster with respect to the bulk arises from the undercoordinated ions present on the surface.

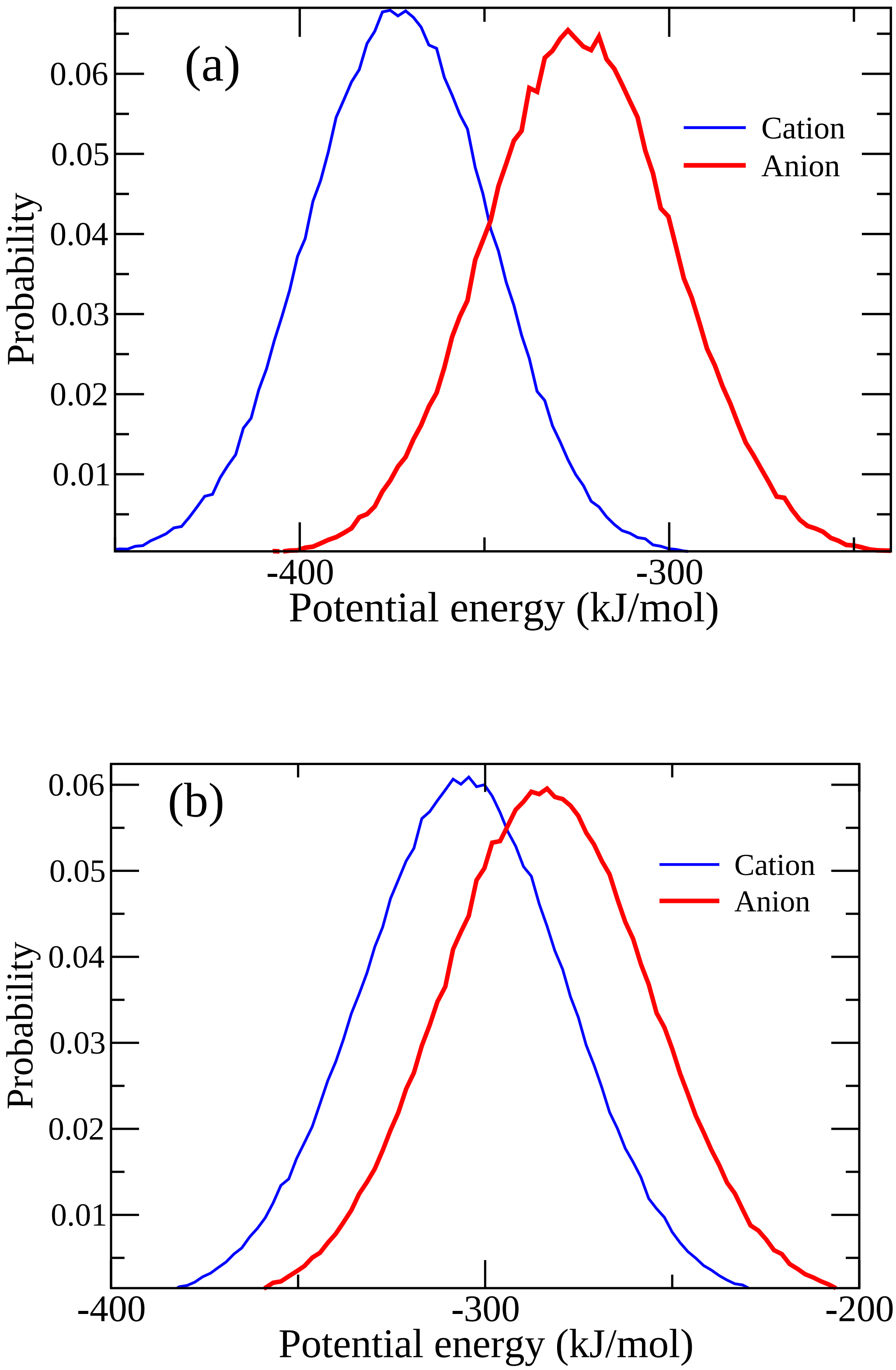

Figure 5.9: Distribution of the potential energy of cation and anion (a) in the bulk region (< 10Å from the COM of the cluster) (b) in the surface region (> 35 Å from the COM of cluster). The data pertains to the 600 ion pair cluster.

Figure 5.9(a) shows the probability distribution of the cation and anion potential energies in the bulk region (i.e., within 10 Å of the COM of the cluster) and Figure 5.9(b) shows the same for the ions residing on the surface of the cluster (i.e., beyond 35 Å of the COM of the cluster) for the 600 ion pair system. This quantity is the total potential energy of a tagged ion arising out of its interaction with all other ions in the system. In the bulk region, the most probable value of the potential energy for cation is more negative than that of the anion and the difference is around 46.0 kJ/mol. While the trend between cation and anion is retained at the surface, the difference in the most probable value reduces to about 25.1 kJ/mol. By comparing the radial profiles of number density (Figure 5.4) and the monomer potential energy (Figure 5.8), it can be concluded that only one layer of ions contribute to the surface energy.

5.3.4 Charge Density and Electrostatic Potential Profile

The profile of the charge density for the 600 ion pair system(Figure 5.10) shows a positive peak at the surface with a net negative value just below it – an electrical double layer at the interface is thus created. The profile is rather noisy in the bulk region, although one would expect it to have a value of zero on grounds of charge neutrality. The charge density profiles for the smaller clusters are even more noiser and hence not shown.

The electrostatic potential profiles were obtained from the atomic charges by using Equation 4. Figure 5.11 shows the block averaged radial profiles of electrostatic potential for the 600 ion pair cluster. The inset shows the same for all clusters. From classical electrodynamics, electrostatic potentials are nothing but the measure of the force experienced by a test charge upon crossing the surface. As the charge density is positive on the surface due to the presence of long butyl chains, the test charge encounters a positively charged surface and then a negative one and so on.

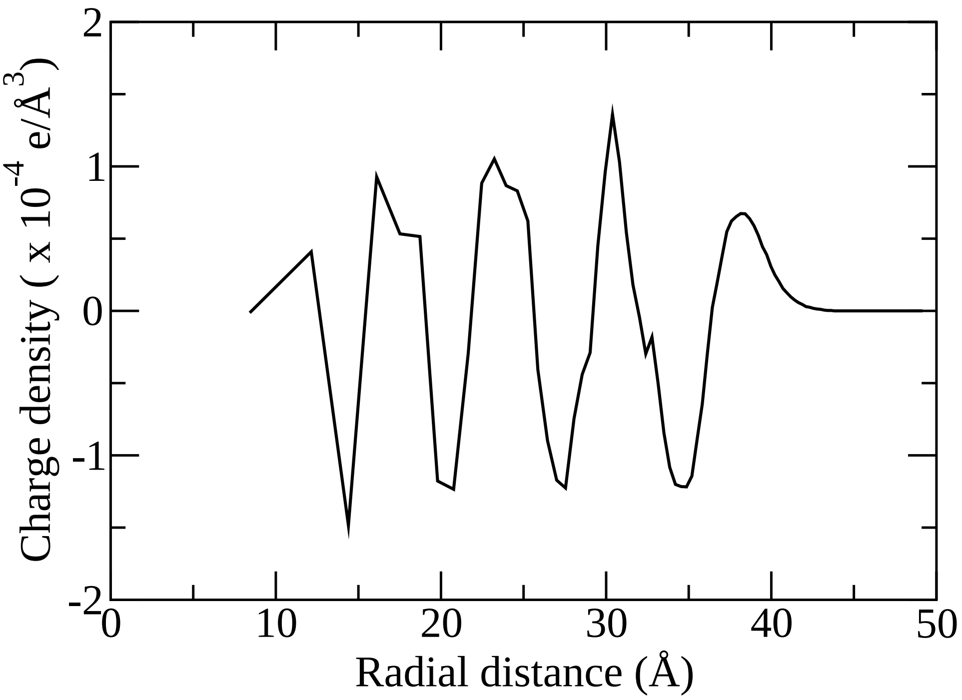

Figure 5.10: Radial profile of the charge density for the 600 ion pair system.

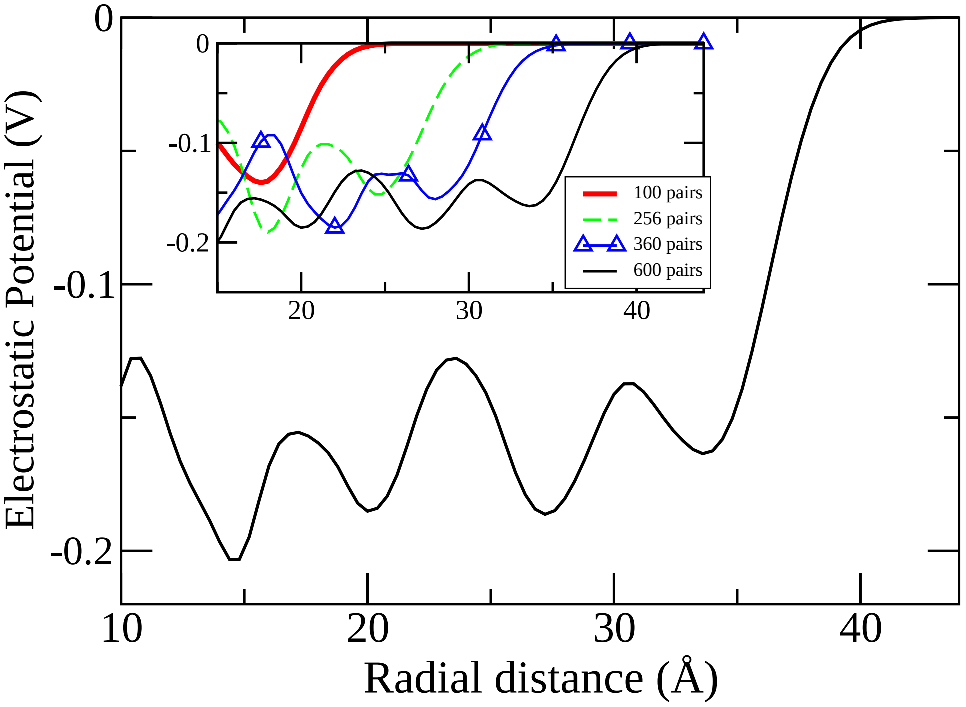

Figure 5.11: Radial profile of the electrostatic potential for the 600 ion pair system. Inset compares the same for various cluster sizes.

Hence, the surface potential in the ionic liquid cluster is found to be negative relative to the gas phase and then oscillates around the mean value, which is similar to the observations on a planar IL-vapour interface for same type of ILs [2, 27]. The average drop in the electrostatic potential for the 600 pair system is found to be -0.17 V and this value decreases marginally with decreasing cluster radius. Lynden-Bell *et al* had obtained a potential drop of -0.22 V for the planar ionic liquid ([bmim][PF_6])-vapour interface [2].

5.3.5 Inter-cluster Interaction

The effective interaction between nanoclusters of ionic liquid needs to be quantified in order to be able to model the phase behaviour of IL based microemulsions and other complex systems. In such microemulsions, the IL pool is "coated" with a surfactant layer [3]. The results reported in this section do not contain the effects of this layer and consider the interactions between two pure IL pools. The former will be addressed in future work.

The adopted procedure to obtain the interaction energy between two clusters is as follows: For a given cluster size, an arbitrary configuration from its MD trajectory is chosen. These coordinates are copied to form a replica cluster. The atoms of the second (replica) cluster are then translated in any of the cartesian direction by 100 Å . Thus, a system containing two clusters having a distance of 100 Å between their centers of mass is created. The total potential energy of the system containing these two clusters is calculated within the all-atom model (i.e., intramolecular, electrostatic and dispersive terms) for several values of the distance separating the centers of mass of the two clusters. The LAMMPS input script used to perform this calculation is provided below:

```
units           real

dimension       3
```

```
atom_style      full
boundary        f f f
read_data       data_1200
include         parm.bmimpf6

neighbor        2.0 bin
neigh_modify    every 2 delay 10 page 8000000 one 40000
timestep        0.5
run_style       verlet

group cluster2 id >= 19201

velocity        all create 300.0 23482341 mom yes rot yes dist gaussian

fix              1 all nve
fix_modify      1 energy yes
thermo_style    multi
thermo          1
thermo_modify   flush yes
dump            1 all custom 1000 dump.bmimpf6 tag mol type xu yu zu
dump_modify     1 flush yes

restart         1  rA.rest rB.rest
run             0

displace_atoms cluster2 move -10.0 0.0 0.0 units box
run             0
```

```
displace_atoms cluster2 move -5.0 0.0 0.0 units box

run            0

displace_atoms cluster2 move -2.0 0.0 0.0 units box

run            0

displace_atoms cluster2 move -1.0 0.0 0.0 units box

run            0
```

In the above script, the molecules belonging to the second cluster are grouped under the name “cluster2”. The last commands, e.g. “displace_atoms” moves the atoms in cluster2 by the Cartesian vector whose triplet are given on the same line. The energy of the system containing the two clusters is obtained thereafter. In this way, the energy profile versus the displacement profile is obtained. Figure 5.12 shows a snapshot of the system.

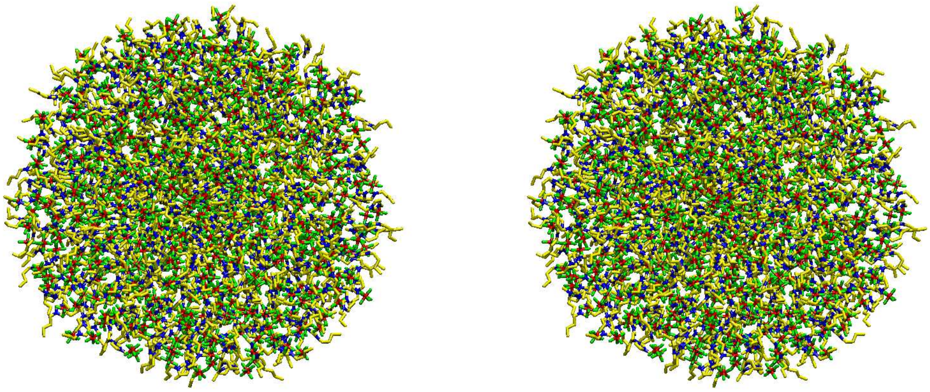

Figure 5.12: Snapshot of two clusters system of the 600 IL pair system. Hydrogen atoms have been removed for the sake of clarity. The colour scheme is same as in Figure 5.3.

The cluster-cluster interaction energy is obtained by subtracting the potential energies of the individual clusters, under isolated conditions (i.e., twice the single cluster energy). This constitutes one interaction energy profile. Results reported here are averaged over eighty such profiles.

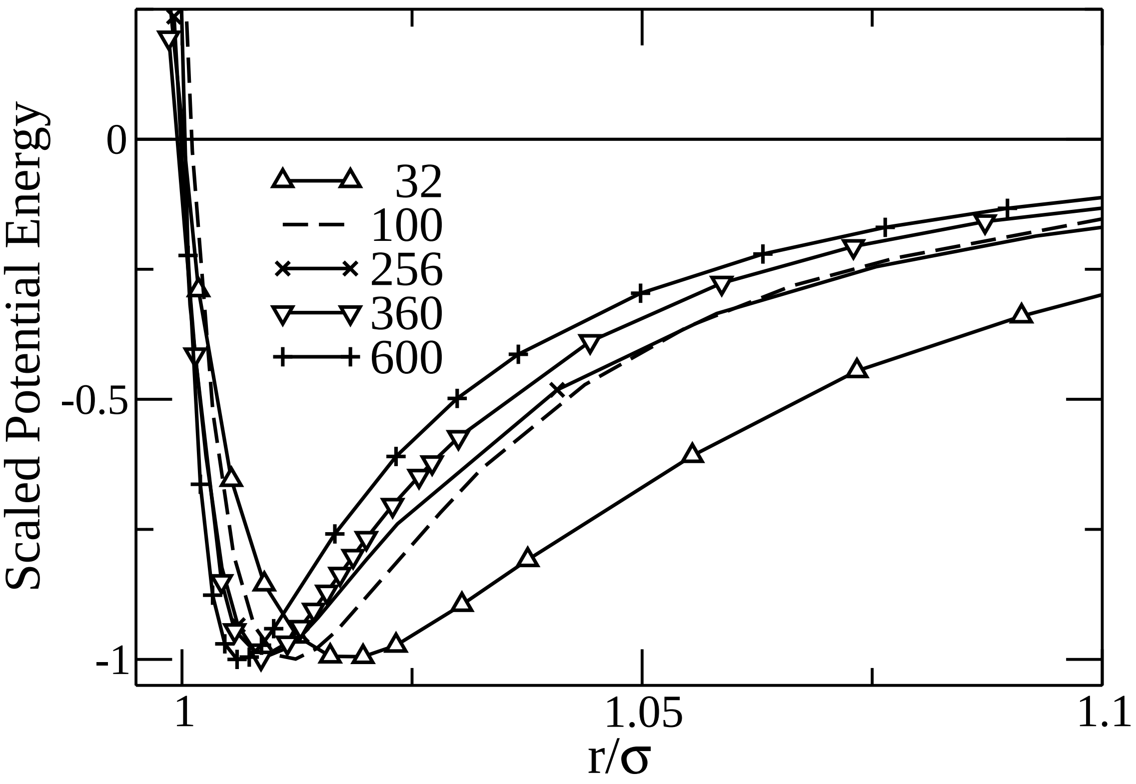

Figure 5.13: Potential of interaction between pairs of clusters of varying sizes. The data is scaled on both the axes – by the value of the minimum energy along the ordinate and the distance at which the potential is zero, on the abscissa.

In Figure 5.13, the interaction energy profile between clusters is shown. The plot is scaled on both the axes – by the minimum value in the energy (ordinate) and by the distance at which the interaction energy is zero (abscissa). Since the cluster surface is rough due to the outward projection of the alkyl tails, the distance at which the minimum is observed and its magnitude varies for each realization of the interaction energy profile. This is to be expected, and thus the representation of the data as a scaled plot is useful. Data from all the cluster sizes are shown. The similarity of the profiles is striking. The profiles can be fitted to a form:

$$U_{cc}(r) = Aexp\left[\frac{-(r-\sigma)}{\rho_1}\right] - Bexp\left[\frac{-(r-\sigma)}{\rho_2}\right] \tag{5.7}$$

Here, ρ_1 and ρ_2 signify the range of repulsive and attractive terms and their values of fit are 0.15Å and 2.62Å respectively for the 600 ion pair cluster. σ denotes the "diameter" of the cluster. One could fit the attractive part of the profile to an inverse power law as well; however, such a fit provides exponents ranging around 30 or so and are harder to interpret. Hence, the exponential attraction term has been chosen. In the scaled representation, the potential well narrows and becomes harder with increase in the cluster size.

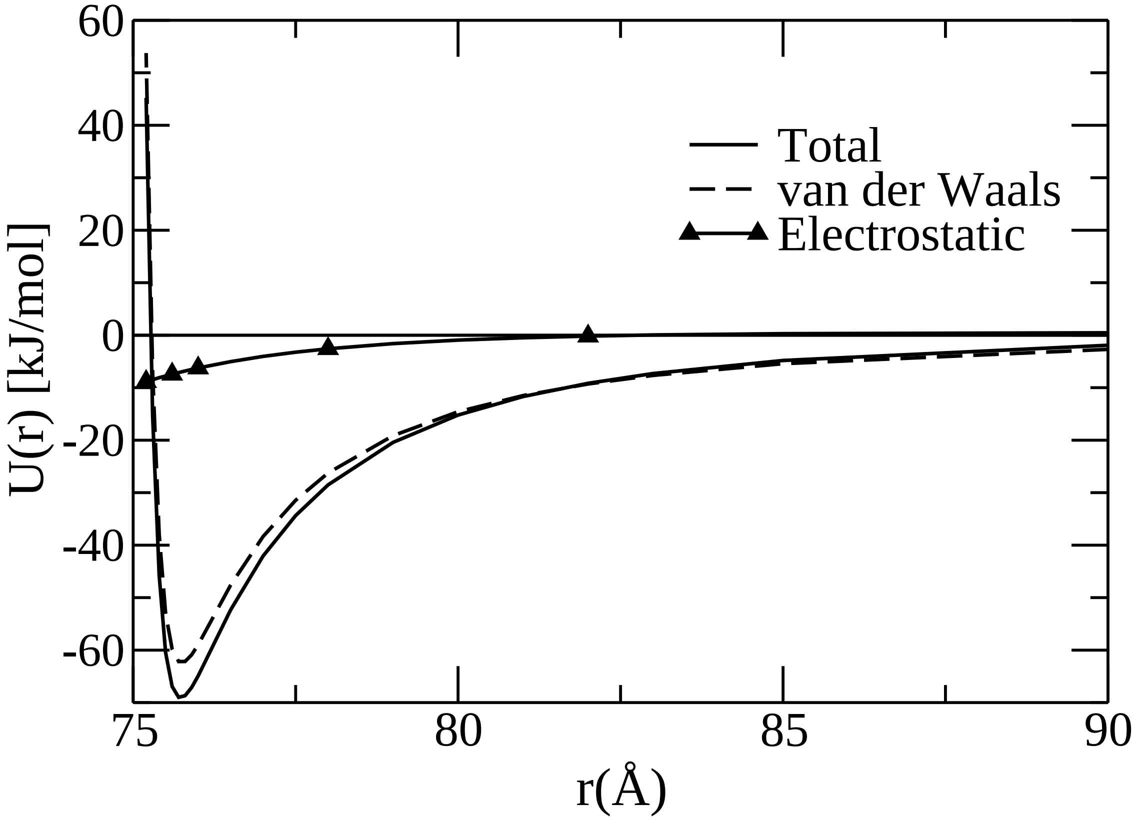

Figure 5.14: Potential of interaction between representative clusters each containing 600 ion pairs as a function of their separation. The contribution to the total potential from electrostatic and van der Waals terms are also shown.

The interaction energy profile possesses a steep repulsion and a strong, but short ranged attraction. The range is short relative to the size of the cluster, but is consistent with that expected for intermolecular forces. This behaviour is reminiscent of micelle-micelle interactions which were well studied many years ago using thermodynamic calculations and light scattering experiments [28, 29]. The attraction arises primarily from the interactions between alkyl groups of the cation. The contribution to the interaction energy from electrostatic and dispersive terms has been examined, and found that the former are much weaker than the latter. As the clusters are charge neutral, the primary electrostatic interaction is dipole-dipole which contributes much less to the total potential energy than the van der Waals terms. This can be seen from a representative energy profile shown in Figure 5.14 for the 600 ion pair system, where these contributions are shown.

The maximum value of the electrostatic energy is around 8 kJ/mol, while the van der Waals contribution is nearly an order of magnitude larger. This result can be rationalized by examining the dipole moment of the cluster. The average magnitudes of dipole moments of the clusters (centered on their respective centres of mass) is listed in Table 5.2.

No. of ion pairs	$\langle\mu\rangle$ (Debye)
32	11.8±0.5
100	19.5±0.6
256	31.2±1.5
360	38.0±1.0
600	48.6±2.3

Table 5.2: Mean dipole moments of nanoclusters of IL. Error bars are standard error on the mean.

At each configuration in the trajectory, the magnitude of the dipole moment was calculated which was then averaged over the entire trajectory. The magnitude of dipole moments are rather large, as expected for such nanometric sized liquid droplets. Assuming an inverse cubic dependence of the dipole-dipole energy with distance, an estimate of 8 kJ/mol is obtained for this interaction at an inter-cluster distance of around 75Å, which explains the rather weak contribution of electrostatics relative to van der Waals. In summary, the van der Waals interaction (primarily between the alkyl groups of the cation) is the chief contributor to the potential energy of the cluster dimer.

In Figure 5.15, the mean value of the well depth as a function of the radius of gyration of the cluster is exhibited. The linear dependence seen here is a direct evidence for the interpenetration model [28–30]. Larger the cluster size, more are the number of site-site dispersive interactions and hence the larger well depth. The data can be fitted to a straight line of the form $\langle U_{min} \rangle$ = -2.8 -1.55R$_g$. Using this function, it should be possible to obtain the mean well depth of arbitrarily large IL clusters.

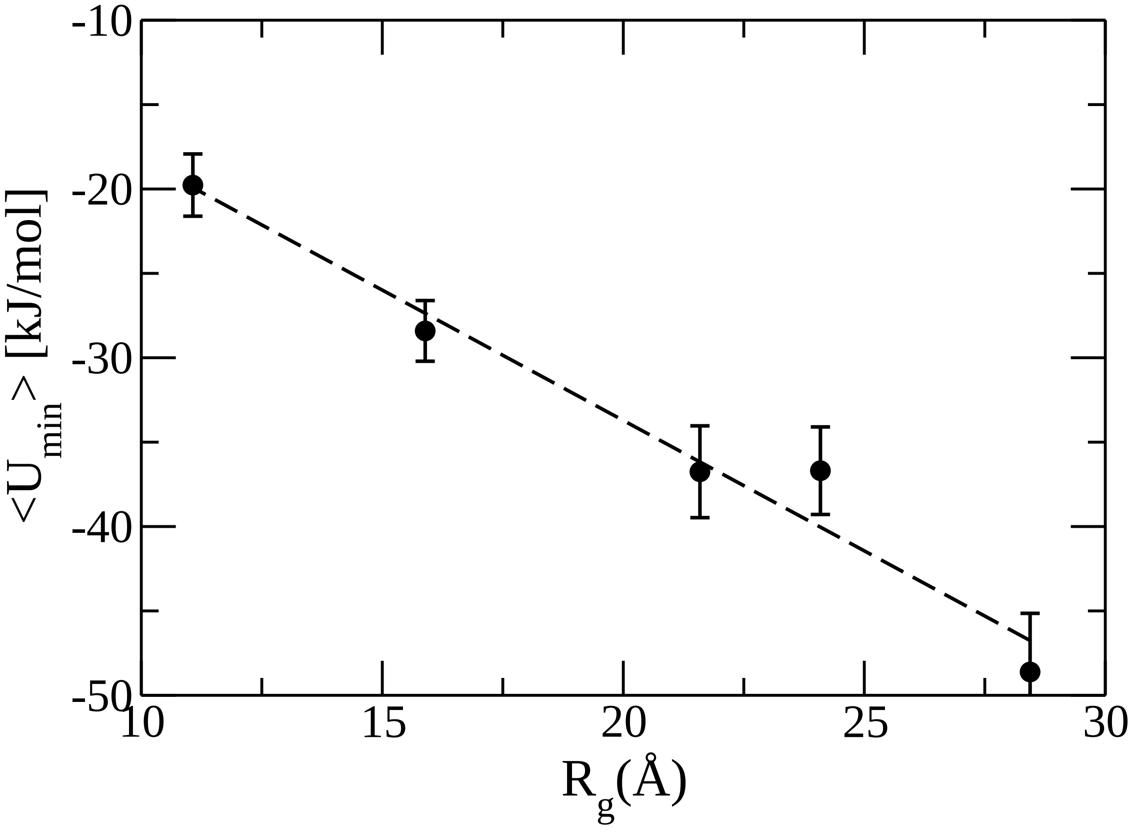

Figure 5.15: The mean value of the minimum in the potential energy of interaction between IL clusters plotted against the radius of gyration of the cluster. The dashed line is a best fit to the data.

5.4 Conclusions

Atomistic molecular dynamics simulations have been carried out on nanometric sized clusters of ionic liquids, in vacuum. The purpose of the study is two-fold: (i) to obtain information on the structure and electrostatic properties of the curved liquid-vapour interface and (ii) to study the effective interaction between IL clusters. Our simulations reveal that the interface is rather rough and is hydrophobic due to the outward projection of the butyl groups of the cation. The number density of the ions and the charge density profile show oscillations near the interfacial region of the cluster. Ordering of the charges at an interface leads to these oscillations. Specifically, the oscillations in the number (and charge) density of the cation and the anion are out-of-phase due to charge ordering. A potential drop of around -0.17V is observed to exist at the interface, in agreement with earlier simulations on the planar liquid-vapour interface [2]. The clusters are spherical in shape and the potential energy per ion pair in the largest cluster studied (that of 600 ion pairs) is higher than the value for the bulk liquid by about 8.0 kJ/mol.

The interaction between clusters of a given size exhibits a deep well with the range of attraction being short when compared to the size of the cluster. The strength of the interaction increases linearly with increasing cluster radius in accordance with the interpenetration model. In the latter, the attractive force between such clusters arises from the alkyl tails of the cation. Interestingly, the interaction is dominated by van der Waals terms in the potential energy, rather than the electrostatic ones. This result can be rationalized by the charge neutrality of the clusters. Despite possessing rather large dipole moments, the dipole-dipole potential contributes only around 10% of the stabilization energy between clusters.

The potential model used in the present study is a non-polarisable one. Yet, the inclusion of polarizability will not affect the qualitative nature of the results. The outward projection of the butyl tails and the interaction strengths (captured through inter-cluster interaction profiles) are not likely to be altered by the inclusion of polarisable interactions. In microemulsions, the reverse micelles (RM) containing the IL pool is coated with a surfactant layer. Thus, the interactions between IL clusters will be mediated by this layer as well as by the solvent (continuous medium). Experiments have demonstrated that the RMs are spherical; hence only minimal deformations of the IL pool through inter-cluster interactions are possible. Although these deformations could stabilize the clusters further, this aspect has not been considered in the current work. The effect of the surfactant layer and the solvent can be studied using Brownian dynamics simulations which will be pursued in future.

The data presented here can be used to build coarse grained models of IL based microemulsions in which the ionic liquid is present in polar pools surrounded by surfactants present in a continuous medium. It should then be possible to study the phase behaviour exhibited in such complex ternary systems.

Bibliography

[1] B.L. Bhargava, S. Balasubramanian, *J. Am. Chem. Soc.*, **128**, 10073, (2006).

[2] R. M. Lynden-Bell, M. G. Del Popolo, *Phys. Chem. Chem. Phys.*, **8**, 949, (2006).

[3] H. Gao, J. Li, B. Han, W. Chen, J. Zhang, R. Zhang, D. Yan, *Phys. Chem. Chem. Phys.*, **6**, 2914, (2004).

[4] Y. Gao, S. Han, B. Han, G. Li, D. Shen, Z. Li, J. Du, W. Hou, G. Zhang, *Langmuir*, **21**, 5681, (2005).

[5] D. Seth, A. Chakraborty, P. Setua, N. Sarkar, *Langmuir*, **22**, 7768, (2006).

[6] A. Adhikari, K. Sahu, S. Dey, S. Ghosh, U. Mandal, K. Bhattacharyya, *J. Phys. Chem. B*, **111**, 12809, (2007).

[7] J. Eastoe, S. Gold, S. E. Rogers, A. Paul, T. Welton, R. K. Heenan, I. Grillo, *J. Am. Chem. Soc.*, **127**, 7302, (2005).

[8] Y. Gao, N. Li, L. Zheng, X. Bai, L.Yu, X. Zhao, J. Zhang, M. Zhao, Z. Li, *J. Phys. Chem. B*, **111**, 2506, (2007).

[9] Y. Gao, A. Voigt, L. Hilfert, K. Sundmacher, *ChemPhysChem*, **9**, 1603, (2008).

[10] J.P. Armstrong, C. Hurst, R.G. Jones, P. Licence, K.R.J. Lovelock, C.J. Satterley, I.J. Villar-Garcia, *Phys. Chem. Chem. Phys.*, **9**, 981, (2007).

[11] V.N. Emel'yanenko, S.P. Verevkin, A. Heintz, *J. Am. Chem. Soc.*, **129**, 3930, (2007).

[12] R. Ludwig, U. Kragl, *Angew. Chem. Int. Ed.*, **46**, 6582, (2007).

[13] M.S.Kelkar, E.J. Maginn, *J. Phys. Chem. B*, **111**, 9424, (2007).

[14] M. G. Del Popolo, J. Kohanoff, R. M. Lynden-Bell, C. Pinilla, *Acc. Chem. Res.*, **40**, 1156, (2007).

[15] R. Ludwig, *Phys. Chem. Chem. Phys.*, **10**, 4333, (2008).

[16] P.A. Hunt, I.R. Gould, B. Kirchner, *Aus. J. Chem.*, **60**, 9, (2007).

[17] B.L. Bhargava, S. Balasubramanian, *J. Chem. Phys.*, **127**, 114510, (2007).

[18] S. J. Plimpton, *J. Comp. Phys.*, **117**, 1, (1995).

[19] B. L. Bhargava, R. Devane, M. L. Klein, S. Balasubramanian, *Soft Matter*, **3**, 1395, (2007).

[20] J. Rudnick, G. Gaspari, *J. Phys. A: Math. Gen.*, **19**, L191, (1986).

[21] A. Baumgartner, W. Renz, *Europhys. Lett.*, **17**, 381, (1992).

[22] E. N. Brodskaya, A. I. Rusanov, *Mol. Phys.*, **62**, 251, (1987).

[23] E. N. Brodskaya, J. C. Eriksson, A. Laaksonen, A. I. Rusanov, *J. Coll. Inter. Sci.*, **180**, 86, (1996).

[24] R. M. Lynden-Bell, M. G. Del Popolo, T. G. A. Youngs, J. Kohanoff, C. G. Hanke, J. B. Harper, C. Pinilla, *Acc. Chem. Res.*, **40**, 1138, (2007).

[25] C. Aliaga, C. S. Santos, S. Baldelli, *Phys. Chem. Chem. Phys.*, **9**, 3683, (2007).

[26] P. Ballone, C. Pinilla, J. Kohanoff, M. G. Del Popolo, *J. Phys. Chem. B*, **111**, 4938, (2007).

[27] R. M. Lynden-Bell, J. Kohanoff, M. G. Del Popolo, *Farad. Discuss.*, **129**, 57, (2005).

[28] B. Lemaire, P. Bothorel, D. Roux, *J. Phys. Chem.*, **87**, 1023, (1983).

[29] S. Brunetti, D. Roux, A. M. Bellocq, G. Fourche, P. Bothorel, *J. Phys. Chem.*, **87**, 1028, (1983).

[30] J. S. Huang, S. A. Safran, M. W. Kim, G. S. Grest, M. Kotlarchyk, N. Quirke, *Phys. Rev. Lett.*, **53**, 592, (1984).

List of Publications

- Nanoclusters of Room-Temperature Ionic Liquids: A Molecular Dynamics Simulation Study.

  S. S. Sarangi, B. L. Bhargava, and S. Balasubramanian

  Physical Chemistry Chemical Physics, **11**, 8745, (2009).

- Correlation between Dynamic Heterogeneity and Local Structure in a Room-Temperature Ionic Liquid: A Molecular Dynamics Study of [bmim][PF_6].

  S. S. Sarangi, W. Zhao, F. Müller-Plathe, and S. Balasubramanian

  ChemPhysChem, **11**, 2001, (2010).

- Molecular Dynamics Simulations of Ionic Liquid-Vapour Interfaces: Effect of Cation Symmetry on Structure at the Interface.

  S.S. Sarangi, S.G. Raju, and S. Balasubramanian

  Physical Chemistry Chemical Physics, **13**, 2714, (2011).

- Low-Frequency Vibrational Modes of Room Temperature Ionic Liquids.

  S.S. Sarangi, S.K. Reddy, and S. Balasubramanian

  Journal of Physical Chemistry B, **115**, 1874, (2011).